

Mass and Magnetic Field of Eruptive Solar Filaments

Jack Carlyle

Thesis submitted for the degree of

Doctor of Philosophy (PhD)

of

University College London

Mullard Space Science Laboratory

Department of Space and Climate Physics

University College London

January 2016

I, Jack Carlyle, confirm that the work presented in this thesis is my own. Where information has been derived from other sources, I confirm that this has been indicated in the thesis.

Abstract

I present a method for column density calculation of filament material seen in absorption in EUV wavelengths which utilises satellite data in a quasi-spectroscopic way. First, back-falling material following a particularly large eruption is examined and found to have column densities comparable with pre-eruption filaments (over 10^{19} cm^{-2}), which is surprising since the filament material had been seen to expand by approximately two orders of magnitude. I then highlight morphology seen in the back-falling material consistent with the Rayleigh-Taylor instability (RTi) and estimate a characteristic magnetic field strength from equations governing the instability to be 0.6 G.

Bubbles indicative of the RTi can also be seen developing into the bulk of the ejecta before breaking up and falling back. The growth rate of these bubbles is measured, and found to be larger than predicted by previous studies. Simulations of RT-unstable plasma are then conducted to investigate the effect of magnetic field strength on the development of the instability, which indicate that the development of the RTi is slower in plasmas with stronger magnetic fields embedded. When the observed growth rates were compared to that of the simulations, they were found to be a factor of five larger possibly due to outflows impacting the material, or that the material is not in fact stationary as the instability sets in.

Finally, the column density calculation is refined by removing the noisy 94 Å channel and then applied to various portions of material involved in two unusual eruptions of an intermediate filament. The total hydrogen mass of the filament is estimated to be $M_H = 2.4 \times 10^{15} \text{ g}$, and over half of this material appears to be lost in the second eruption.

Acknowledgements

Firstly I would like to thank UCL Impact Funding and the Max Planck Society for funding this PhD, without which, none of this work would have been possible.

I would also like to thank my academic supervisors. Lidia van Drield-Gesztelyi has gone far beyond the call-of-duty, not only imparting her immense wisdom of solar physics, helping me make the most of every academic opportunity, but also looking out for my personal wellbeing. I cannot thank her enough for everything she has done for me. David Williams also deserves far more credit than I could give; he has frequently helped me with work at the drop of a hat, worked long hours when deadlines loomed, and has always made time to listen when I'm having a hard time. Davina Innes provided indispensable insight into my work, and made me feel welcome and at home as soon as arriving in a new country. Sami Solanki and Sarah Matthews have both also supported me academically and personally through a very demanding three years. I owe all of these wonderful people so much.

I would also like to say a special thanks to Andrew Hillier, who has worked tirelessly in helping my understanding of plasma instabilities and MHD simulations. Without him, I would not have had the opportunity to work in Kyoto, and I certainly would not have survived my time there.

My parents have my eternal gratitude for everything they have done for me over the last 28 years, especially putting up with me during the final few months of writing this thesis, which I know wasn't fun. Thanks goes to my sister, Martha, too, for lending me her car when I needed it and generally being a great sibling. And thank you, Mia Lovrić, for keeping me much more emotionally stable than I otherwise would have been, and for tolerating all of

my instabilities.

So many other kind hearts have helped me out in so many different ways over the last three years, and thanking all of them would be impossible. However I would like to mention as many as I can, as without the support of the people around me, I would be nothing.

Everyone in the MSSL Solar group has been incessantly wonderful, kind, and helpful, as were so many people working elsewhere in MSSL and at the Max Planck Institute for Solar System Research; not least of all Deb Baker, who made me feel a part of the group before I'd even sat down at my desk. I'd like to thank John Hodges, Steve Fossey and Ian Howarth for being inspirational teachers; Rosalind Medland, Libby Daghorn, Judy Bartley, Julia Wehrle, Suzanne Winter, Ines Dominitzki, Katrina Walker and Asha Jhummu for helping with all sorts of things, and for always offering a friendly chat; Jane Salton and Daisuke Kawata for trying to help me improve the student living conditions; Professor Shibata-san for welcoming me into his group; Duncan Stackhouse for being Duncan Stackhouse; David Perez-Suarez for leaping to help without hesitation whenever he can (especially NAM2015); Shinsuke Takasao for taking me on a date in Kyoto when I felt lonely; Don Schmit for helping me carry a washing machine up three flights of stairs; Theresa CF for accompanying me to the emergency room when I almost poisoned myself in a foreign country; Martin de la Nougerede for saving me when I was stranded with a broken axel; David Belda, Michel Eberhardt, Fransisco Inglasias and Ivan Millic for taking me to lunch every day in Germany; Alice Foster, Kirthika Mohan and Nadine Kalmoni for fun walks in the woods; Przemek Szponarski for playing hide-and-seek with me; Steph Yardley for driving over 3,500 miles in 10 days on a hare-brained adventure; Gherardo Valori for introducing me to his cats; Ricardo Gafeira for helping me get access to my data when I thought all hope was lost; Sally Dacie for bringing me my notebook when I thought all hope was lost (again); Nicole Saltz for talking sense into me when I need it; Anton Rubisov for keeping my enthusiasm for academia up; Shereif Mujahed for always listening when I need to unload; and thanks to anyone and everyone who I have met since starting this PhD. You are what has made it worthwhile.



Contents

	Page
Abstract	3
Acknowledgements	4
List of Figures	10
List of Tables	13
1 Introduction	14
1.1 The Sun	14
1.1.1 Structure	15
1.1.2 Observing the Sun	18
1.1.3 Magnetic Field & MHD	22
1.2 Filaments & Eruptions	31
1.2.1 Filaments	31
1.2.2 Eruptions	36
1.3 The Rayleigh-Taylor Instability	43
2 Instrumentation	47
2.1 The Solar Dynamics Observatory (SDO)	47
2.1.1 The Atmospheric Imaging Assembly (AIA)	49
2.2 Solar TERrestrial RELations Observatory (STEREO)	53
2.2.1 Extreme Ultraviolet Imager (EUVI)	55
3 Density and Dynamics of In-Falling Material Following the 2011 June 7 Eruption	57

3.1	Observations	58
3.2	Density Calculation Method	60
3.3	Column Density Analysis of In-Falling Material	65
3.4	Rayleigh-Taylor Morphology & Magnetic Field Estimation . .	71
3.5	Discussion	73
3.6	Conclusions	76
4	Observations and Simulations of The Rayleigh-Taylor Instability in Erupted Material	77
4.1	Measured Rayleigh-Taylor Growth in Erupted Filament Plasma	78
4.1.1	Observations	78
4.1.2	Rayleigh-Taylor Growth Analysis	79
4.2	Numerical Simulations of Rayleigh-Taylor Unstable Plasma . .	85
4.2.1	Ideal MHD Simulations	85
4.2.2	The Effect of Magnetic Field Strength on the Nonlinear Development of the Rayleigh-Taylor Instability	91
4.3	Comparison of Observations and Simulations	94
4.4	Discussion	96
4.5	Conclusions	98
5	Estimating the Total Mass of An Unusual Eruptive Filament	100
5.1	Observations	107
5.2	Refining the Column Density Calculation	110
5.3	Mass Investigation	113
5.3.1	Method	113
5.3.2	Total Target Masses	114
5.3.3	Estimating the Total Filament and Eruption Mass . . .	118
5.4	Discussion	118
5.5	Conclusions	124
6	Summary, Conclusions & Future Work	126
6.1	Summary & Conclusions	126
6.2	Future Work	128

7 List of Publications	131
7.1 Peer-reviewed Journals	131
7.2 Conference Proceedings	132
Bibliography	133

List of Figures

1.1	The solar atmosphere seen in an eclipse.	18
1.2	Temperature profile of the solar atmosphere.	19
1.3	The Sun in EUV.	20
1.4	Magnetic reconnection between two field lines.	25
1.5	Magnetic reconnection between two fields.	26
1.6	β profile of the solar atmosphere.	27
1.7	The Zeeman effect.	28
1.8	A filament seen in $H\alpha$	31
1.9	Flux rope formation	33
1.10	Cross-sectional area of H I, He I and He II for photoionisation	35
1.11	The standard CME model.	38
1.12	An unusual eruptive IF on the 15 th of March 2015.	42
1.13	The 7 th of June 2011 eruption.	43
1.14	Rayleigh-Taylor mixing region.	44
2.1	The Solar Dynamics Observatory.	48
2.2	AIA images in each bandpass, as well as three HMI images. . .	50
2.3	Temperature response of SDO/AIA filters.	51
2.4	The Atmospheric Imaging Assembly layout.	51
2.5	AIA telescope cross-section.	52
2.6	STEREO.	54
2.7	EUVI telescope cross-section.	56
3.1	Target blobs viewed from SDO/AIA.	59
3.2	Target blobs viewed from STEREO-A/SECCHI.	59
3.3	Abundance-weighted photoionisation cross-sections of H and He.	61

3.4	The column density model fit to five data points.	63
3.5	171 Å image of Target 1 and associated background.	64
3.6	171 Å image of Target 1 and $G = 0.5$ contours.	65
3.7	Calculated N_H and G for Target 1, 07:06 UT.	66
3.8	Calculated N_H for Target 1, 07:15 – 07:40 UT	66
3.9	Calculated G for Target 1, 07:15 – 07:40 UT.	67
3.10	Histograms of N_H for Targets 1a and 1d.	67
3.11	Histograms of G for Targets 1a and 1d.	68
3.12	Calculated N_H for Target 2, 07:11 – 07:56 UT.	68
3.13	Calculated G for Target 2, 07:11 – 07:56 UT.	69
3.14	Calculated N_H for Target 3, 07:40 – 08:34 UT	69
3.15	Calculated G for Target 3, 07:40 – 08:34 UT	69
3.16	Calculated N_H for Target 4, 07:03 – 07:48 UT.	70
3.17	Calculated G for Target 4, 07:03 – 07:44 UT	71
3.18	Errors on N_H for Targets 1a and 4a.	71
3.19	RTi morphology: simulation and target blob.	72
4.1	Erupted material undergoing RTi.	80
4.2	Distance-time plots of observed bubble fronts.	82
4.3	Observed bubble height as a function of time squared.	83
4.4	log bubble height as a function of time.	84
4.5	The mixing region of select simulations at several times.	89
4.6	The mixing region of W2, 3, 4 at $t = 2, 4, 6$	90
4.7	B simulation bubble heights as a function of time squared.	92
4.8	W simulation bubble heights as a function of time squared.	93
4.9	Normalised observation & simulation bubble heights as a function of time squared.	95
5.1	Polarity Inversion Lines in AR12297.	101
5.2	AR12297 in 193 Å, H α and HMI, pre-eruption	102
5.3	Material ejected during the first (failed) eruption	103
5.4	Cartoon of the magnetic set-up of AR12297 and surroundings	105
5.5	AR12297 and an intermediate filament before and after erupting	106

5.6	Filament material shown in 94 and 171 Å.	106
5.7	Target 1; a portion of the IF.	107
5.8	Target 2; a portion of the smaller filament.	108
5.9	Target 3; the smaller filament.	109
5.10	Target 4; material ejected from AR12297.	109
5.11	Target 5; the erupted smaller filament bulk.	110
5.12	Column density values including and omitting 94 Å.	111
5.13	Error on N_H values including and omitting 94 Å.	111
5.14	High geometric depth values including and omitting 94 Å.	112
5.15	Low geometric depth values including and omitting 94 Å.	112
5.16	χ^2_ν values including and omitting 94 Å.	113
5.17	‘Bad’ χ^2_ν values including and omitting 94 Å.	113
5.18	Target 1 and associated background in 171 Å.	114
5.19	Column density of Target 1.	115
5.20	Target 2 and associated background in 171 Å.	115
5.21	Column density of Target 2.	115
5.22	Target 3 and associated background in 171 Å.	116
5.23	Column density of Target 3.	116
5.24	Target 4 and associated background in 171 Å.	117
5.25	Column density of Target 4.	117
5.26	Target and background of the filament eruption at 01:19 UT.	117
5.27	Column density of Target 5.	117
5.28	AR12297 and the IF in H α on the 15 th of March 2015.	119
5.29	Absorption depth for four SDO/AIA bandpasses.	122
5.30	Bad G values for Target 4.	123

List of Tables

2.1	Wavelengths observed by SDO/AIA.	49
4.1	Initial conditions of varied parameters and measured nonlinear growth rate over first set of simulations.	88
4.2	Initial conditions of varied parameters and measured nonlinear growth rate over second set of simulations.	90

Chapter 1

Introduction

1.1 The Sun

The Sun has always been revered as an immense source of power, being worshipped across many cultures from the dawn of humankind. For example, one of the major deities in ancient Egyptian religion was Ra, the Sun God, signifying a direct acknowledgement of the importance of the Sun. A less obvious example of ancient Sun-worship can be found in many prehistoric monuments dotted around the British Isles, such as Stonehenge, where certain structures were designed to align with sunrise or sunset on a solstice or equinox.

Even contemporary western cultures, though lacking any unified religious organisation, treat our mother star with some spiritual significance, whether intentional or not: the excitement we share with one another when the skies are clear on a weekend; the fact that we consider sunny days “good weather” and other days “bad” is telling itself. Perhaps a more objective interpretation of the spiritual importance of the Sun in modern times is a psychological diagnosis known as Seasonal Affective Disorder, a personality disorder whereby mood is negatively impacted by the poorer weather of the winter months, demonstrating that sunlight is indeed likely to have a psychological effect on us as a species. Furthermore, we frequently repeat the mantra that one must never look directly at the Sun with the naked eye which, given the importance we ascribe to it, seems almost like a religious idea - we must deny ourselves ever glimpsing the great power which we so desire to bask in (although the reason for this is due to safety, rather than superstition).

This fixation is not unjustified, either - we now know that almost all energy on our planet originated in the Sun, and in fact all matter on (and in) our planet was formed from the same protostellar gas-and-dust cloud as the Sun. Many religions call God the creator, the source of all life, and in terms of our world, there seems to be no candidate better suited to this position than the Sun.

The energy generation occurs deep within the centre of the Sun via nuclear fusion. The dominant reaction is the proton-proton chain, a process which converts hydrogen to helium with approximately 0.7% of the mass converted to energy. The extremely high pressure in the centre of the Sun can bring the protons (hydrogen nuclei) close enough together such that quantum mechanical tunnelling may allow the particles to overcome the repulsive electrostatic forces, allowing the attractive nuclear force to take effect, causing nuclear fusion. The mass of the Sun is 2×10^{30} kg, with a mass composition of 75% hydrogen, 24% helium and 1% heavier elements. The proton-proton chain occurs in the Sun about 9.2×10^{37} times per second and generates 3.8×10^{26} joules per second. The Sun is known as a main-sequence star, *i.e.*, with sufficient mass to ignite nuclear fusion in its core without having yet exhausted its hydrogen; it has been in this stage of its life for about 4.6 billion years, and will not exhaust the hydrogen in its core for another 5 billion years.

1.1.1 Structure

While there are no tangible boundaries in (or on) the Sun, it is generally considered to have several different layers, defined by the dominant energy transfer mechanism. In the broadest sense, the Sun may be divided up into an interior, a surface layer and an atmosphere, with further subdivisions therein.

The energy generation described previously takes place in the core of the Sun, extending from the centre to roughly 0.25 of the solar radius $R_{\odot} = \sim 6.96 \times 10^8$ m, where some 34% of the entire mass of the Sun is concentrated. The core has a density of ~ 150 g cm⁻³ and a temperature of $\sim 1.5 \times 10^7$ K. Above the core lies the radiative zone, so-called because radiative transfer is the dominant energy transfer process, and has a density between 0.2 – 20 g cm⁻³ and a temperature of $2 - 7 \times 10^6$ K. The radiative

zone, extending out to approximately 0.7 solar radii, rotates with the core as a solid body at a rate of 430 nHz: about one rotation every 27 days.

As temperature falls moving away from the centre of the Sun, collisional ionisation becomes less effective and electrons may occupy shells of atoms for longer periods of time. This, in turn, increases the bound-free opacity of the material, and causes a steeper temperature gradient. At the outer edge of the radiative zone, the temperature gradient becomes steep enough to allow convection to set in, and so the outermost portion of the solar interior is known as the convective zone, as this is the dominant heat-transfer process. This means there is a mass motion of material in the form of circular convection currents as the lower-lying material is heated from the radiative zone beneath and becomes less dense than its surroundings, rising up, whilst the material at the top cools, becoming more dense and sinking. This causes granulation of the surface, where large cells of convective overturning can be seen from above, material rising in the centre, moving horizontally outwards as it cools before sinking back down in inter-granular lanes. These rising ‘parcels’ of material also generate acoustic waves which propagate through the interior, the study of which is known as helioseismology, one of the most powerful tools for probing the interior of the Sun.

The rotation rate of the convection zone is lower than that of the radiative zone and there is a transition region with very large shear between the two, known as the tachocline. The convective zone rotates as a normal fluid with differential rotation, the equatorial regions rotating faster (with a period of as low as 25 days) than polar regions (with a period of up to 35 days). The density and temperature rapidly fall as the top of the convective zone is approached, reaching around 0.016 g cm^{-3} at the surface, with an effective temperature of approximately 5,800 K.

What is generally considered the surface of the Sun is not a surface in the sense of any sudden interface or boundary, but is in fact defined visually; the visible edge is where the population of H^- ions becomes low enough to allow visible light to escape unimpeded, which occurs at a relatively static radius from the centre, $\sim 6.96 \times 10^8 \text{ m}$ (R_{\odot}). The material above this is colloquially

referred to as the solar atmosphere, but as below, so above are there several distinct layers with unique traits. The first layer is called the photosphere ('photo' being derived from the Greek word for 'light') and is extremely thin compared to the radius of the Sun, at only ~ 500 km, though the density falls by several orders of magnitude and the temperature also decreases somewhat.

The next layer is the chromosphere, roughly five times thicker than the photosphere on average, a complex, irregular structure. Around supergranular boundaries is the so-called chromospheric network, composed in part of fine, radial, jet-like structures known as spicules. These spicules are narrow columns, a few hundred kilometres in diameter, ascending upwards with velocities of around 30 km s^{-1} , reaching altitudes of up to 9,000 km. When observed in an $\text{H}\alpha$ filter (see Section 1.1.2), elongated dark and bright features are seen, known as fibrils and mottles, present everywhere near concentrations of magnetic field.

The temperature minimum of the Sun, $\sim 4.5 \times 10^3 \text{ K}$, is found approximately at the bottom of the chromosphere, with temperatures reaching around $7 \times 10^3 \text{ K}$ at the top. The density varies between $\sim 10^{-10} \text{ g cm}^{-3}$ at the bottom and $\sim 10^{-13} \text{ g cm}^{-3}$ at the top. The chromosphere is a highly dynamic environment and the temperature and density profiles can not be easily described for the entire Sun simultaneously. "Chromosphere" literally means 'sphere of colour', due to its appearance during a solar eclipse often being a bright red, as shown in Figure 1.1.

The outermost layer in the solar atmosphere is the corona, extremely diffuse at $10^{-15} \text{ g cm}^{-3}$ yet extremely hot at almost 1 MK. The temperature of the corona increases gradually with height above the solar surface, but the jump between the upper chromosphere and lower corona is so sudden that there is often described an intermediate transition region where the temperature increases two orders of magnitude over only a few hundred kilometres. The temperature profile of the whole atmosphere is shown in Figure 1.2. There is no definitive outer edge to the corona, and the material making up the solar atmosphere is in fact continuously outflowing as a solar wind. This reaches out to beyond the planets and creates a shock where the (dynamic) pressure

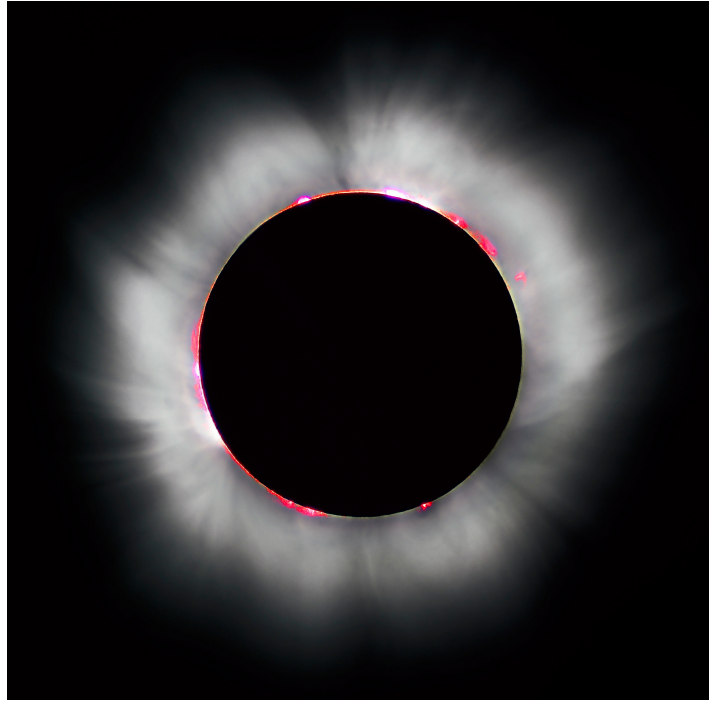


Fig. 1.1: The solar atmosphere can be seen during a solar eclipse: the chromosphere is the low-lying red material, and the corona is the white, wispy lines leading away from the Sun. Image credit: Luc Viatour, www.lucnix.be.

balances that of the interstellar medium, defining the outer boundary to the solar system, or the heliosphere.

1.1.2 Observing the Sun

The study of the Sun involves observation as a primary means of investigation. The photosphere appears as a relatively unvarying sphere, characterised by granules with bright centres and relatively dark inter-granular lanes, as well as the possibility of a few sunspots (explained in Section 1.1.3). The continuum emission peaks in the visible range and this is dominated by Fraunhofer absorption lines. The continuum emission from the Sun at wavelengths shorter than the visible is of lower intensity than the spectral lines in this wavelength range, which emanate from higher regions of the solar atmosphere, allowing for observations of these locations in short wavelengths.

Spectral emission lines are peaks in intensity of light occurring at wavelengths which correspond to energy released by de-exciting atomic transitions; as the electrons fall to a lower state in the atom, energy is released from the

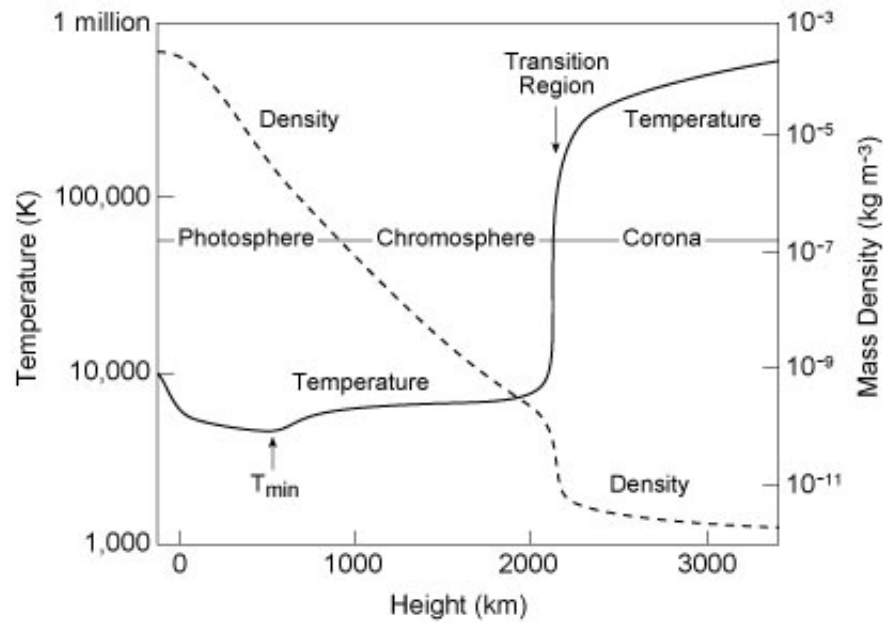


Fig. 1.2: Graph showing canonical temperature and density gradients for the solar atmosphere. Image credit: Eugene Avrett, Smithsonian Astrophysical Observatory.

system as a photon. This means that the wavelength of the dominant spectral lines emitted by a medium will indicate the internal energy, that is, temperature. This is because temperature describes the average kinetic energy of particles (as a maxwellian distribution), and as such characterises the typical energy exchanged in a collision; this energy is quantised by exciting an electron to the closest corresponding energy level of the atom, and so the most common de-excitations will be from this same level, leading to photons of a particular energy, and therefore wavelength, being produced most commonly.

By measuring the intensity of specific wavelengths, *i.e.*, spectral lines of species present in the Sun, we can essentially observe different locations and features in the solar atmosphere. The photosphere appears in visible light (predominantly scattered light from the interior) and the $H\alpha$ fibrils of the chromosphere may also be seen in absorption in this wavelength range, however, the corona is barely visible here. The chromosphere, transition region and corona all have strong emission at shorter wavelengths, such as Ultraviolet (UV, $\sim 400 - 91.2$ nm), Extreme Ultraviolet (EUV, $91.2 - \sim 10$ nm) and X-rays ($\sim 10 - 0.01$ nm). An example of EUV emission can be seen in Figure 1.3, highlighting the transition region and upper chromosphere. A contribution

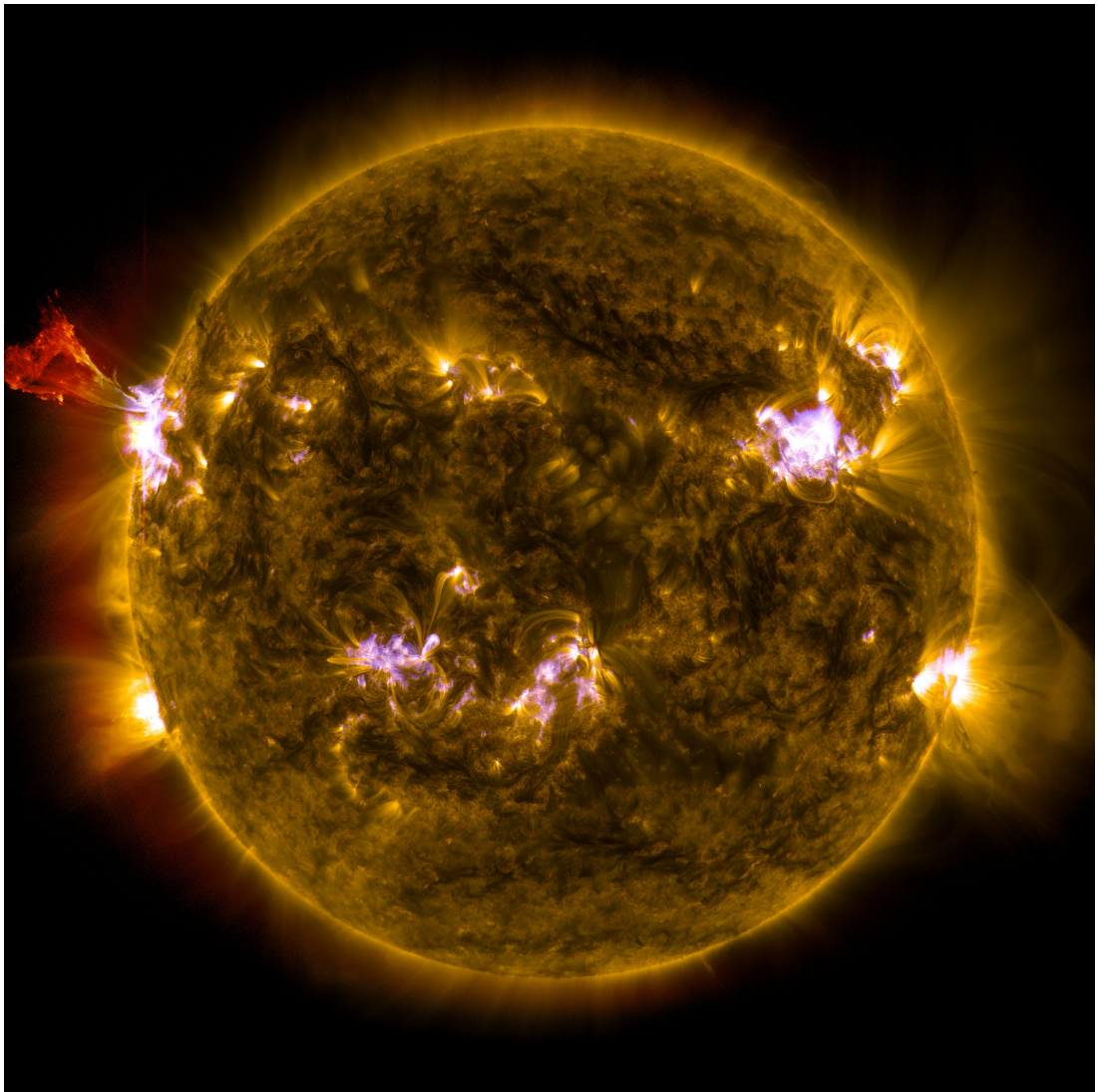


Fig. 1.3: A composite image of three EUV lines (131 (purple), 171 (yellow) and 304 (red) Å). Image credit: NASA/SDO/AIA.

factor can be calculated for particular wavelength filters as a function of temperature and ion abundance, allowing for temperature diagnostics of coronal material by observing different ions (*i.e.*, different spectral lines). This also means that particular filters of instruments will observe material over some range of temperatures, characterised by the response function of the filter. See Table 2.1 for an example of such bandpasses on NASA’s Solar Dynamics Observatory.

When measuring the light received from a particular source, it is always important to consider whether this light will be modified at all on its path be-

tween source and observer. For example, if the LOS passes through a material then photons may be scattered (reflected/redirected by a collision with a particle) or absorbed (destroyed by exciting an electron to a higher energy level or even liberating it entirely), and conversely new photons may be emitted in the same direction, adding to the source. When examining the emission from the corona, the latter is in fact the desired measurement; the total photon emission from the plasma along the LOS. So are scattering and absorption effective in the corona? This can be answered by considering the mean free path (MFP), the average distance travelled by a photon before encountering a particle, of the corona, given as:

$$L_{mfp} = \frac{l}{\sigma_{\nu} l \cdot n}, \quad (1.1)$$

where we have used l as the distance travelled by a photon, σ as the cross-sectional area of the particle (which is more like the probability of the photon interaction than a physical size, although its units are cm^2 ; this is frequency-dependent, as denoted by ν) and n is the number density of particles. Therefore, the denominator of equation 1.1 is the number of particles encountered over distance l . n in the corona is of the order 10^8 cm^{-3} close to the Sun and falls with r^2 , and for the EUV lines which the corona is commonly observed in $\sigma_{\nu} \sim 10^{-19} \text{ cm}^2$, and so L_{mfp} is of the same order as the Sun–Earth distance. The physical interpretation of this is that absorption and scattering are negligible effects in this regime and as such can be disregarded. The corona is said to be optically thin in EUV.

Optical depth is a description of how much light is attenuated by absorption as it passes through a specific medium. It is the integration of the opacity κ of the medium over the physical depth l , *i.e.*,

$$\tau_{\nu}(l_{abs}) = \int_{l_{abs}} \kappa_{\nu} dl, \quad (1.2)$$

where

$$\kappa_{\nu} = \sigma_{\nu} n, \quad (1.3)$$

and any material with $\tau < 1$ is said to be optically thin. An optical depth of unity indicates that the physical depth of the material is equal to L_{mfp} .

Optically thick material is any material with $\tau > 1$, as is the case for cool, dense, low-lying material in the solar atmosphere which appears dark in many spectral lines. The dominant process by which such material in the lower corona removes photons from the LOS is photoionisation, in which a photon incident on an atom is destroyed and the energy is converted into liberating an electron entirely. The former results in spectral absorption lines (the inverse effect of spectral emission lines, whereby the quantised nature of energy levels of an atom results in specific wavelengths of light being emitted or absorbed), whilst the latter gives rise to an absorption continuum; any photon with energy greater than or equal to the ionisation potential of the atom in question may be absorbed.

1.1.3 Magnetic Field & MHD

Whilst the Sun can be described as a sphere of self-gravitating hydrogen and helium (*etc.*), this is not the whole story. The Sun is also composed of strong magnetic fields, some of which may have been inherited from the protostellar cloud from which it formed, but more importantly magnetic fields are also generated at the tachocline (as described by dynamo theory). The polarity of the solar magnetic field roughly aligns with the axis of rotation, though the polarity periodically reverses (see below).

The material which makes up the Sun is a plasma, a quasi-neutral fluid state of matter composed (at least partially) of positively and negatively charged particles. This means the fluid is electrically conductive and as such may generate or be affected by magnetic fields. The study of the behaviour of plasma is known as magnetohydrodynamics (MHD), and a set of equations under particular approximations may be used as a complete description of (idealised) plasma. These equations may be used in different forms, with additional or fewer terms, depending on the specific system being described. These equations in conservative form (*i.e.*, with no sinks or sources) are written in CGS units (centimetre-gram-second) as:

The equation of state:

$$P_{gas} = \frac{R\rho T}{\mu} = nk_B T \quad (1.4)$$

The equation of mass conservation:

$$\frac{\partial \rho}{\partial t} + \nabla \cdot (\rho \mathbf{v}) = 0 \quad (1.5)$$

The equation of momentum conservation:

$$\frac{\partial \rho \mathbf{v}}{\partial t} + \nabla \cdot (\rho \mathbf{v} \mathbf{v} - \frac{\mathbf{B} \mathbf{B}}{8\pi} + P \mathbf{I}) = 0 \quad (1.6)$$

The equation of energy conservation:

$$\frac{\partial e}{\partial t} + \nabla \cdot [(e + P) \mathbf{v} - \frac{\mathbf{B}(\mathbf{v} \cdot \mathbf{B})}{4\pi}] = \eta \mathbf{j}^2 \quad (1.7)$$

Ohm's law:

$$\mathbf{E} + \frac{\mathbf{v} \times \mathbf{B}}{c} = \eta \mathbf{j} \quad (1.8)$$

Faraday's equation:

$$\nabla \times \mathbf{E} = - \frac{\partial \mathbf{B}}{\partial t} \quad (1.9)$$

Poisson's equations (Gauss' law for an electric field):

$$\nabla \cdot \mathbf{E} = 0 \quad (1.10)$$

Ampere's law:

$$\nabla \times \mathbf{B} = \frac{4\pi \mathbf{j}}{c} + \frac{1}{c} \frac{\partial \mathbf{E}}{\partial t} \quad (1.11)$$

Gauss' law for a magnetic field:

$$\nabla \cdot \mathbf{B} = 0 \quad (1.12)$$

The induction equation:

$$\frac{\partial \mathbf{B}}{\partial t} - \nabla \times (\mathbf{v} \times \mathbf{B}) - \eta \nabla^2 \mathbf{B} = 0 \quad (1.13)$$

Here I use total pressure $P = P_{gas} + P_{mag}$, $P_{mag} = \mathbf{B}^2/8\pi$, gas constant R , density ρ , temperature T , mean molecular mass μ , number density n , Boltzmann constant k_B , time t , bulk velocity of the fluid \mathbf{v} , magnetic field \mathbf{B} , energy density $e^1 = \epsilon + \rho(\mathbf{v} \cdot \mathbf{v}/2 + (\mathbf{B} \cdot \mathbf{B})/2)$, internal energy ϵ , electric field \mathbf{E} , speed of light c ($= 3 \times 10^8 \text{ ms}^{-1}$), current density \mathbf{j} and magnetic diffusivity η . For an infinitely conducting fluid, $\eta = 1/4\pi\sigma = 0$ (where σ is conductivity), and this is the provision for what is known as ideal MHD.

¹usually written as E , but changed here so as not to be confused with electric field \mathbf{E}

An ideal plasma is unable to move across magnetic field lines according to Alfvén's frozen-flux theorem, which states that in a fluid with infinite conductivity, any fluid motion perpendicular to the field-lines would generate infinite eddy currents. This means that magnetic field cannot move independently of plasma, which gives rise to different effects at different locations in the Sun.

This can be defined more rigorously; in order to determine the validity of the frozen-in-flux condition, we may consider the magnetic flux Ψ passing through a contour C co-moving with the plasma and bounded by a surface S :

$$\Psi = \int_S \mathbf{B} \cdot d\mathbf{S}. \quad (1.14)$$

Two processes may affect the rate of change of Ψ over time: firstly, the time variation of \mathbf{B} ,

$$\frac{\partial \Psi}{\partial t} = \int_S \frac{\partial \mathbf{B}}{\partial t} \cdot d\mathbf{S}, \quad (1.15)$$

and using Faraday's law, which states that $-(\partial \mathbf{B} / \partial t) = \nabla \times \mathbf{E}$:

$$\frac{\partial \Psi}{\partial t} = - \int_S (\nabla \times \mathbf{E}) \cdot d\mathbf{S}. \quad (1.16)$$

Secondly, the movement of C (relative to B): if we call a length element of C by dl , the area swept out by dl in dt is $\mathbf{v} \times dl$ and the flux passing through this area is $\mathbf{B} \cdot \mathbf{v} \times dl$. So we have

$$\frac{\partial \Psi}{\partial t} = \int_S \mathbf{B} \cdot \mathbf{v} \times dl = \int_S \mathbf{B} \times \mathbf{v} \cdot dl, \quad (1.17)$$

and using Stoke's theorem,

$$\frac{\partial \Psi}{\partial t} = \int_S \nabla \times (\mathbf{B} \times \mathbf{v}) \cdot d\mathbf{S}. \quad (1.18)$$

Combining these two, we obtain

$$\frac{\partial \Psi}{\partial t} = - \int_S \nabla \times (\mathbf{E} + \mathbf{v} \times \mathbf{B}) \cdot d\mathbf{S}, \quad (1.19)$$

which, for Ohm's law (equation 1.8) in an infinitely conducting plasma (*i.e.*, ideal MHD, where $\eta = 0$), then

$$\frac{\partial \Psi}{\partial t} = 0 \quad (1.20)$$

the flux through a contour moving with the plasma cannot change over time.

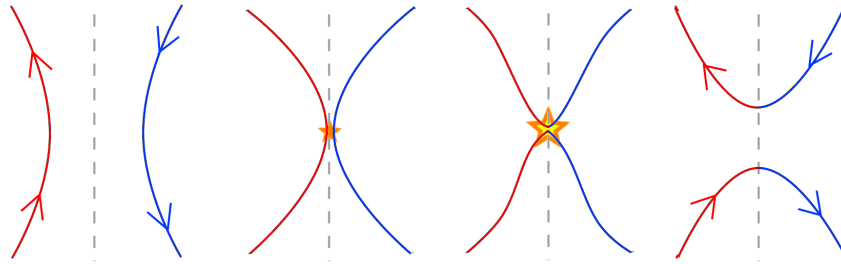


Fig. 1.4: A basic 2D schematic showing magnetic reconnection between two field lines and energy release. Line colour corresponds to initial connectivity, arrows show the direction of magnetic field, and the star indicates the location of energy release. Original cartoon.

This condition suggests that a portion of plasma will only ever be able to lie along a single field line, however, this is not strictly the case. Magnetic reconnection is a process in which the magnetic topology is rearranged into a lower energy state, releasing the energy as kinetic, thermal and particle acceleration. The individual effect on a field line is that upon meeting an antiparallel field line under certain conditions (*i.e.*, a current sheet is needed, where ideal MHD breaks down), the two lines will appear to split and reattach to one another, releasing energy at the point of reconnection, as shown in Figure 1.4. The overall effect of this (as it is unlikely that a single field line would reconnect on its own, and if it did might not release sufficient energy to be noticed; besides, a ‘field line’ is a concept or a description of physical laws, as opposed to a quantifiable object) is that plasma is seen to inflow towards a point on a line, and outflow from the same point perpendicular to the inflows, as shown in Figure 1.5.

Reconnection allows plasma to occupy different elements of flux while it remains on the Sun, or even leave the Sun entirely. Reconnection is thought to play an important role in many observed phenomena, which are covered in more detail later in this Chapter. The trigger for magnetic reconnection could be anything which forces magnetic fields with antiparallel vector components towards one another. This could for example be caused by plasma movement with large momentum, or even magnetic pressure from surrounding fields. Indeed, the trigger for reconnection depends largely on the environment, which

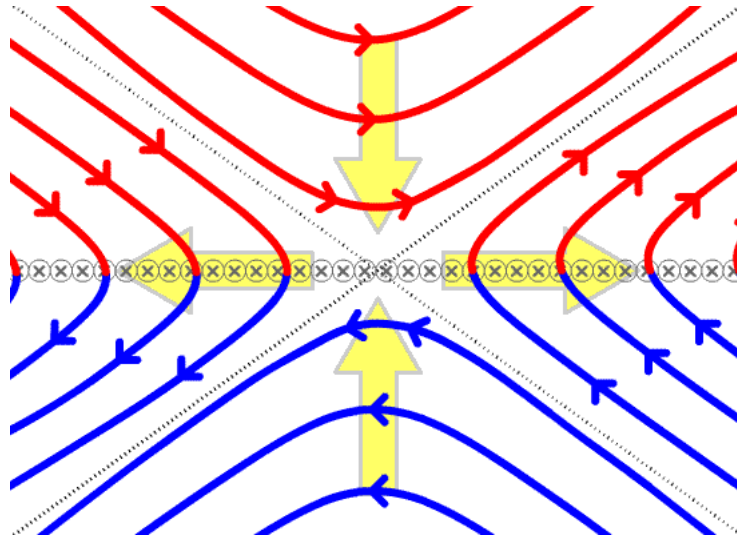


Fig. 1.5: A basic 2D schematic showing magnetic reconnection between two fields, flows (yellow arrows), and the location of the current sheet (\otimes). Image in the public domain.

may be described by the ratio between the gas pressure of the plasma and the magnetic pressure of the field.

The ratio of gas pressure to magnetic pressure is known as plasma β :

$$\beta = \frac{P_{gas}}{B^2/8\pi} . \quad (1.21)$$

Within the interior and in the photosphere, this value tends to be greater than unity (increasing with depth), and so the motion is dominated by the fluid. This leads to the spherically self-gravitating appearance and observed rotation. However, β falls rapidly in the chromosphere to values lower than unity, resulting in the magnetic forces dominating the motion. This is what gives the corona its appearance, seen in Figures 1.1 and 1.3.

The differential rotation in the interior, high- β regions of the Sun lead to the magnetic fields becoming ‘wound-up’ and stretched in the equatorial direction. These fields then rise to the surface with the convecting plasma and can end up crossing the surface. Above this, β is less than unity, and magnetic tension forces the fields to become as straight as possible whilst both ends remain rooted in and below the surface, resulting in complex loop-like formations, as well as some ‘open’ field-lines, with one end rooted in the sun and the other out in the solar wind.

This gives the corona a fascinating appearance, with magnetic loops and

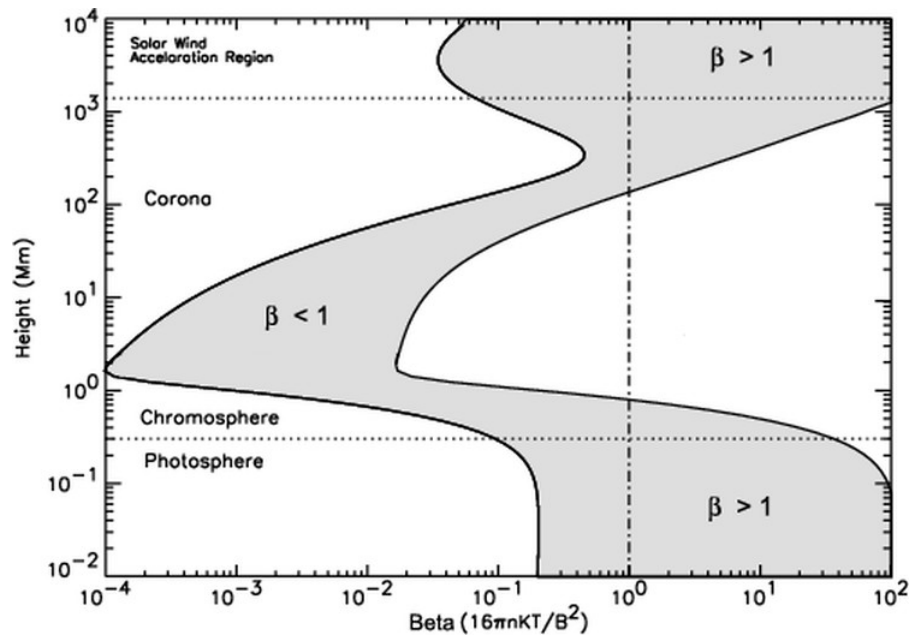


Fig. 1.6: Graph showing canonical β values for the solar atmosphere. Image adapted from Gary (2001).

many other dynamic features seen in EUV lines. Dense patches of bright loops of strong magnetic field are known as active regions, and appear particularly bright in EUV and X-rays. These often coincide with sunspots on the photosphere, dark patches (in the visible range) appearing at points of the highest concentration of radial magnetic field. This is due to convection being magnetically suppressed by the sudden drop in β and hence a fall in the temperature of the photospheric material. Where magnetic field lines are only rooted in the Sun at one end, the plasma is able to flow outwards with the pressure gradient arising from the high temperature; this is known as the solar wind. The result of this outflow is that the areas containing the footpoints of these open field lines become less dense than the surrounding closed-loops and hence appear darker in EUV, known as coronal holes.

Line-of-sight (LOS) magnetic fields can be detected in the photosphere by observing the Zeeman effect, whereby the interaction of external magnetic field strength (and orientation) and the internal magnetic moment of an emitting atom results in the splitting of the spectral line into several components, simultaneously polarising each component. The interaction of the magnetic field and magnetic moment alter the energy of the photons emitted (increase

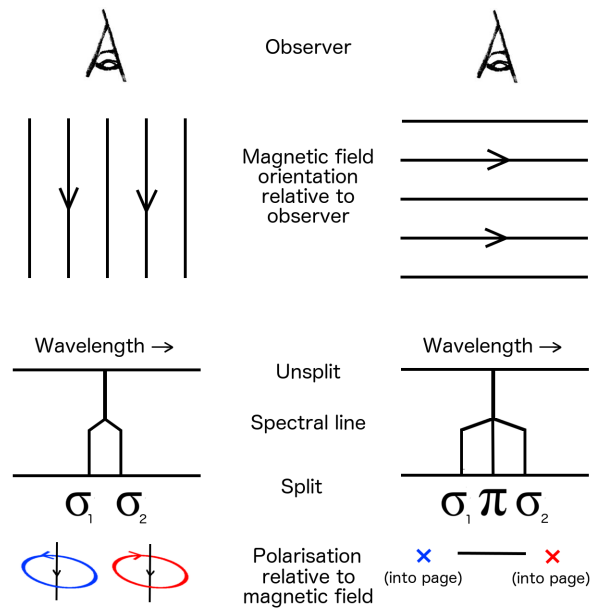


Fig. 1.7: A diagram illustrating the shift in wavelength and polarisation of split spectral lines in the presence of a magnetic field by the Zeeman effect. Note that for magnetic field towards the observer results in opposite circular polarisation to the case presented on the left. Original cartoon adapted from Phillips (1995).

or decrease depending on the orientation of the atom) proportionally to the strength of the magnetic field. For fields parallel to the LOS, the Zeeman effect gives rise to two components labelled as σ , one displaced to higher wavelength than the unsplit line, and the other to lower. These components will also be circularly polarised in opposite senses. Should the magnetic field, however, be perpendicular to the LOS, three components arise: the two σ -components with wavelength shift as the previous case, and also with a π -component, unshifted relative to the unsplit spectral line. In this case, the two σ -components are linearly polarised perpendicular to the magnetic field, whilst the π -component is polarised parallel to the magnetic field. This description is illustrated in Figure 1.7.

A magnetogram is an image of the Sun indicating LOS magnetic field (relative) strength, which are typically made by subtracting a circularly polarised image of the photosphere from the same image with opposite circular polarisation. This is the difference in intensity of both σ -components in the

presence of a field parallel to the LOS and will indicate the directionality of the magnetic field.

The wavelength displacement of spectral lines is given as

$$\Delta\lambda = \frac{\pi e \lambda^2 g B}{M_e c}, \quad (1.22)$$

where here π is the traditional mathematical constant, e is electron charge, M_e is electron mass, λ is the wavelength of the unsplit spectral line, g is what is known as the Landé factor (determined by the spin, angular and orbital angular momentum of the atom) and B is magnetic field strength. This immediately demonstrates that the Zeeman effect will only be observable for sufficiently strong magnetic fields (and high Landé factor), however, this also shows the dependence on λ^2 , suggesting that this effect will be more easily observed at longer wavelengths. This is part of the reason that the effect can only be observed at the photospheric level, where not only are magnetic fields very strong, but also emission is typically in the visible wavelengths. Coronal emission lines are almost exclusively in the EUV range and as such the $\Delta\lambda$ becomes very small. The measurement of coronal magnetic field by this method is further complicated by the extremely high temperature of the corona; the full-width-half-maximum (FWHM, the width of a spectral line at half of the peak intensity) of a spectral line increases with temperature due to thermal doppler broadening (particles in a fluid material are moving both towards and away from the observer at any given moment, and the temperature of a gas is a measure of kinetic energy of the particles, so higher temperature simply leads to greater line-of-sight velocities which may ‘stretch’ or ‘squash’ the wavelength of the emitted photon). So the high temperature of the corona prevents direct measurement of the associated LOS magnetic field by the Zeeman effect for both of these reasons.

Coherent scattering of photons by resonant spectral lines results in the polarisation of light. In the presence of a horizontal magnetic field, this polarisation is modified, and this is observed as the Hanle effect. This has been used to successfully probe turbulent magnetic fields near the base of the chromosphere, though is not as widely applicable as the Zeeman effect due to

conflation with other effects (*e.g.*, the Zeeman effect becomes mixed in at sufficiently high magnetic field strengths, as is often the case, inhibiting measurement of the Hanle effect), and the need for considerable scattered light (Stenflo 1982).

The global magnetic field of the Sun is not constant, but in fact has a quasi-periodic variation. Dubbed the activity cycle, it was first recognised as a pattern in the number of sunspots and has since been shown to correspond to an 11 year (on average) cyclic change in the magnetic field. The cycle is characterised by a sharp rise and gradual fall in the number of sunspots on the Sun, as well as other phenomena strongly associated with magnetic activity. At the beginning of the cycle, sunspots tend to lie at latitudes above 30° , and as the cycle progresses and the number slowly falls, the sunspots are observed at progressively lower latitudes.

At roughly the point of maximum activity, the polar fields of the Sun are seen to reverse, though not necessarily simultaneously (for example, the southern polar field reversed in mid-1957 while the north polar field did not reverse until in late-1958). The true cycle is therefore approximately 22-years in length, as each 11-year cycle is complemented by another with reversed magnetic field direction. The cycle is generally accepted to arise from the frozen-in flux being ‘wound up’ by the differential rotation between different depths of the interior, especially at the strongly sheared tachocline, where dynamo processes amplify magnetic field.

The increased magnetic activity at the peak of each cycle gives rise to many dynamic features and effects in the low β atmosphere. A greater number of active regions is seen coinciding with sunspot number, coronal holes appear at lower latitudes as the cycle progresses, and complex magnetic, mass-carrying structures form, which can launch material from the chromosphere out into the corona and beyond. However, whilst such magnetic activity is more commonly seen near cycle maxima, the variable and transient magnetically-driven phenomena have also been known to occur during minima. For a detailed review on the solar cycle, see Hathaway (2010).

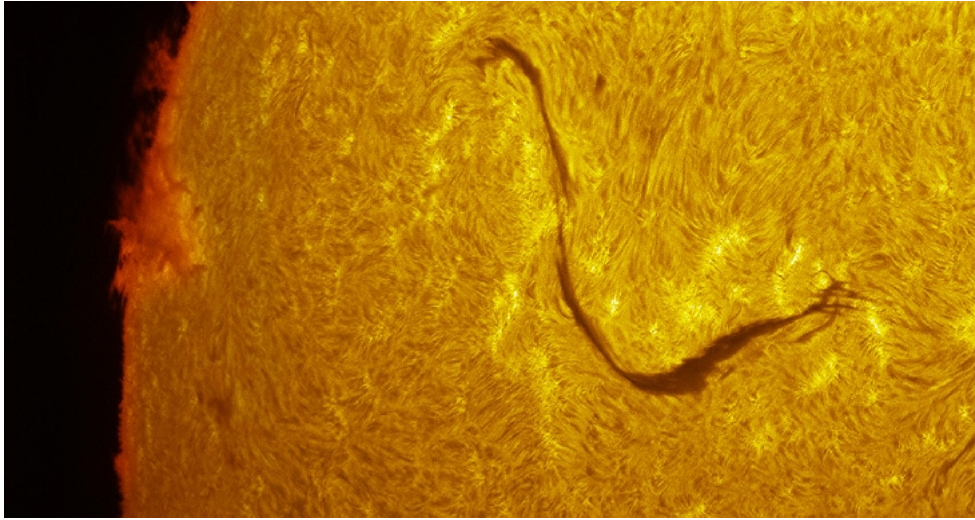


Fig. 1.8: A particularly large filament viewed in $H\alpha$. Image credit: Jack Newton.

1.2 Filaments & Eruptions

1.2.1 Filaments

As magnetic fields rise into the solar atmosphere and reconfigure, material from the chromosphere may be forced up into the lower corona. The relatively cool, dense material can become suspended against gravity at heights of up to tens of megameters by magnetic tension in dips of the field lines, appearing in absorption against the hotter, brighter background. Elongated structures of such material are observed frequently on the solar disc, thousands of kilometres in length, referred to as filaments. When these structures are seen extending out from the solar limb, they appear bright against the diffuse background corona and are referred to as prominences. Filaments and prominences are fundamentally the same structures, the naming convention being an artefact of the history of solar observations. I will use the terms interchangeably, but since this work concentrates on absorbing material, I will primarily refer to them as filaments. For a summary of current observations, theories and models of filaments, see Labrosse et al. (2010), Mackay et al. (2010) & Parenti (2014).

Filaments are found above neutral lines separating opposite polarity magnetic fields in the photosphere, known as polarity inversion lines (PILs), which are most commonly found around the borders of polar coronal holes, between or around active regions, and embedded inside active regions. Filaments which

form over these are referred to as quiescent filaments (QF), intermediate filaments (IF) and active region filaments (ARF), respectively. The former two, especially QF, tend to be larger (up to lengths which are comparable to the solar radius, heights above 2×10^4 km) and longer lived (up to several months), while the latter are smaller (of the order 10^4 km in length and less than this in height), more dynamic structures, typically lasting only a few days. Filaments can be seen in the deep-red visible spectral line $H\alpha$ and in many EUV lines (see Table 2.1 for more information on some observed wavelengths). Filaments appear to be formed of many fine (~ 200 km thick) threads apparently lying along magnetic field lines roughly aligned with the PIL, or the spine of the filament (Mackay et al. 2010; Parenti 2014).

There are several theories on filament formation, many of which involve the formation of so-called flux-ropes. These are long bundles of twisted, intertwined magnetic field lines, rooted either side of a PIL with a strong shear, causing the main length of the flux rope to lie along the PIL. This is thought to be built up by magnetic loops rooted either side of the PIL reconnecting with and around one another as the footpoints are shifted towards and along the PIL in opposite directions (van Ballegooijen and Martens 1989), illustrated in Figure 1.9. The reconnection occurs low down in the atmosphere, and so chromospheric material could be ‘scooped-up’, or levitated, in the newly reconnected field lines; this is one theory on the origin of the mass in the flux ropes. The other newly reconnected line is a small loop, which is subducted below the surface by magnetic tension ‘pulling’ it straight. This could explain what is known as flux cancellation, seen in magnetograms as two concentrations of opposite polarity moving together before disappearing. Other theories postulate that the flux rope emerges from beneath the photosphere already formed, and the mass may or may not be pulled up with it. Another possibility is put forth by DeVore and Antiochos (2000), who argue that a flux rope is not formed at all, and show that magnetic loops with sufficient shear in their footpoints can become dipped, giving a potential well for material to collect in.

As well as the different theories for filament structure, so too is there still

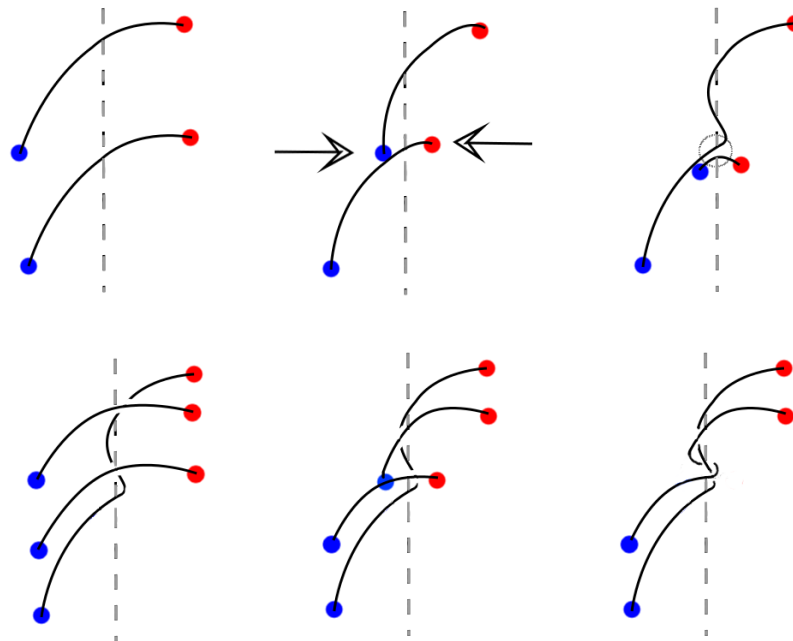


Fig. 1.9: A diagram illustrating how magnetic loops lying above a PIL (represented by the dashed line) may reconnect to form a flux rope along the PIL. The newly reconnected region is shown with a dashed circle in the top third panel. The bottom row shows how as this occurs multiple times, the field lines become longer and more intertwined, forming a flux rope. Original cartoon.

some question over how the mass comes to be supported by these structures in the first place. As previously mentioned, some have theorised that the material is levitated by magnetic forces, either as flux emerges from the interior, or reconnects low down in the atmosphere. It has also been shown that reconnection in the low atmosphere can produce jets of material, and so it is possible that reconnection with low-lying fields at the foot of a filament could inject mass into the magnetic structure (Chae 2003). This would also account for observed counter-streaming flows. However, this is expected to be more likely to occur in ARFs, leaving other mechanisms required to explain the formation of QFs and IFs (Mackay et al. 2010). Studies have indicated that a thermal nonequilibrium process can act as a mechanism for putting chromospheric material into the corona, in which localised heating above the flux tube footpoints causes the chromospheric plasma to evaporate, condensing in the coronal part of the magnetic structure (Luna et al. 2012). Furthermore, Isobe et al. (2005) performed three dimensional simulations of emerging flux which show the observed filamentary structure might arise spontaneously from the Rayleigh-Taylor instability (detailed in Section 1.3).

Prominence mass is not a trivial quantity to determine, as historically techniques have required observations in optically thick lines and radiative transfer modelling of these lines, and typically, only order-of magnitude estimates are made (see Labrosse et al. (2010) for a more detailed history). However, in recent years, techniques have been developed for more accurately determining prominence mass; Gilbert et al. (2005) used temporal-interpolative and spatial-interpolative approaches to determine the column density of erupting and quiescent prominences, respectively, using observations obtained from the EUV Imaging Telescope on board the SOHO spacecraft, by measuring how much coronal radiation in the Fe XII spectral band is absorbed by prominence material. They then went on to calculate the mass of an erupting prominence from 12 July 1999 as being approximately $\sim 6 \times 10^{14}$ g. This method is further developed by Gilbert et al. (2011), where the technique was expanded to conduct the analysis in three different wavelength regimes, covering three different species' photoionisation continua. They concluded that the total prominence

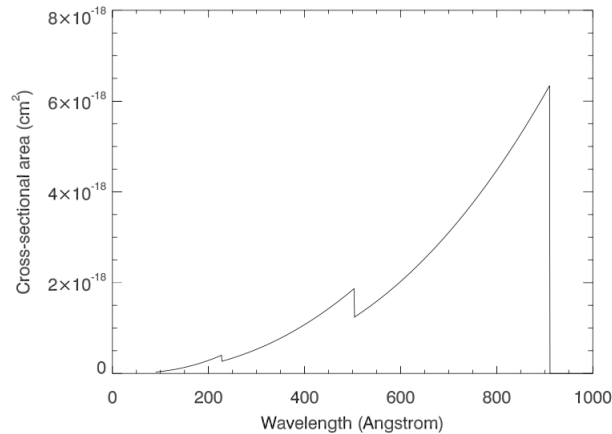


Fig. 1.10: A graph showing the cross-sectional area of H I, He I and He II for photoionisation as a function of wavelength. The sudden drops are due to longer wavelength photons not having sufficient energy to ionise a species at all.

mass estimate is lower for the higher wavelengths analysed, attributed to the higher opacity causing a saturation of continuum absorption in these lines and thus a potentially large underestimation of the mass. This suggests that such column density diagnostics are best conducted at shorter wavelengths, where particles appear to have smaller cross-sections and therefore a greater number of particles would be required to remove all photons from the LOS. This is highlighted by Figure 1.10, which plots the cross-sectional area for photoionisation for H I, He I and He II as a function of wavelength.

Heinzel et al. (2008) undertook a thorough study of a quiescent prominence, using observations in $H\alpha$, EUV and X-rays from many instruments across several missions, examining absorption and emissivity blocking. They go on to discuss the determination of hydrogen column density and ionisation degree in the prominence, finding column densities in agreement with Gilbert et al. (2005) for an ionisation degree of 0.5. They showed this value for ionisation degree is appropriate within a small variance for a range of temperatures comparable with prominences.

Landi and Reale (2013) developed a method to determine prominence electron temperature and column emission measure from EUV and UV absorption. This work describes the temperature and absorption coefficients for the most abundant elements in the Sun (H & He) for distinct wavelength

ranges. This can be used to calculate the electron column density as well as the relative abundance of helium.

Most recently, Schwartz et al. (2015) have used a similar technique of measuring EUV absorption to calculate column density and total mass of quiescent prominences, however, this work also used X-ray emission in order to calculate the intensity of the background, rather than extrapolating a background using nearby, unobscured quiet Sun in the EUV images; the drawback to this is that dedicated campaigns are usually needed to obtain X-ray observations, whereas full-disk EUV images are taken extremely frequently by multiple instruments and missions. Schwartz et al. (2015) found the total mass of the six prominences studied to be between 2.9×10^{14} and 1.7×10^{15} g, based on column densities of the order $10^{18} - 10^{19} \text{ cm}^{-2}$, agreeing with results of other authors.

1.2.2 Eruptions

As the magnetic fields supporting these massive structures shift and reconfigure, accumulating free magnetic energy, they can become unstable, triggering a runaway process of upward motion and expansion above sites of reconnection. This is thought to result in a release of magnetic energy, leaving the system in a more relaxed state. These eruptions are known as coronal mass ejections (CMEs). Since CMEs are associated with strong concentrations of magnetic field, filaments are often located near, or even embedded in, the CME precursor. Often a significant fraction of the mass contained within these structures is carried with the magnetic field and ejected out into interplanetary space.

It can therefore be deduced that the most common filaments to erupt are ARFs, though IFs may also be seen to erupt, either fully or partially. However, a ‘full’ eruption does not necessarily mean that all of the filament material is ejected into the heliosphere. Indeed, material can be seen streaming down magnetic field lines during eruptions, and material which is ejected further from the initial configuration can often be seen falling back to the surface at later times. Failed eruptions may occur, whereby low lying magnetic fields suddenly reconfigure, ejecting material, but overlying fields may constrain further motion into the heliosphere.

As filament material is ejected away from the solar surface, it moves into

locations progressively lower magnetic pressure, and as such expands with the magnetic fields carrying it. This leads to a decrease in density which lowers the optical depth, and so the material becomes more ‘transparent’ when viewed in absorption. It is also possible for such material to be heated during an eruption, either by reconnection, enhanced radiation from the AR, or even conduction from hotter material on newly reconnected field lines. Higher temperatures indicate that more hydrogen and helium particles will have lost electrons, which means fewer photons will be absorbed by photoionisation, further increasing the transparency of this material at relevant wavelengths (see Section 1.1.2).

Following a filament eruption, the magnetic environment in the low corona may appear almost unchanged with respect to the pre-eruption configuration, or totally different, depending on the magnitude of the eruption. Filaments themselves may also appear relatively similar before and after erupting, however, the very definition of a filament eruption requires some change in the mass; even failed eruptions will typically cause some mass to be lost from the filament, though in this case it would not be ejected into interplanetary space. ARFs often disappear completely following an eruption, as the strong associated magnetic fields tend to lead to more violent events. IFs, on the other hand, are more likely to remain at least partially, as the magnetic fields which are not above the associated AR may be relatively unaffected by any eruption.

CMEs have been historically observed in the upper corona, as Thomson-scattered white light from the photosphere is more clearly visible against the darkness of space than against the brightness of the solar disc, provided the relatively bright Sun is occulted from view. When seen in coronagraph images, they are typically described by a three-part structure: a bright frontal arc of swept-up coronal material, followed by a dark evacuated cavity and a bright core of embedded filament material; however, not all CMEs necessarily contain all three elements. Whilst many CMEs contain little filament mass, either due to the material flowing back down along field lines connected to the solar surface, or simply no filament being present, a filament eruption may sometimes be referred to as a CME. In the case of a failed filament eruption,

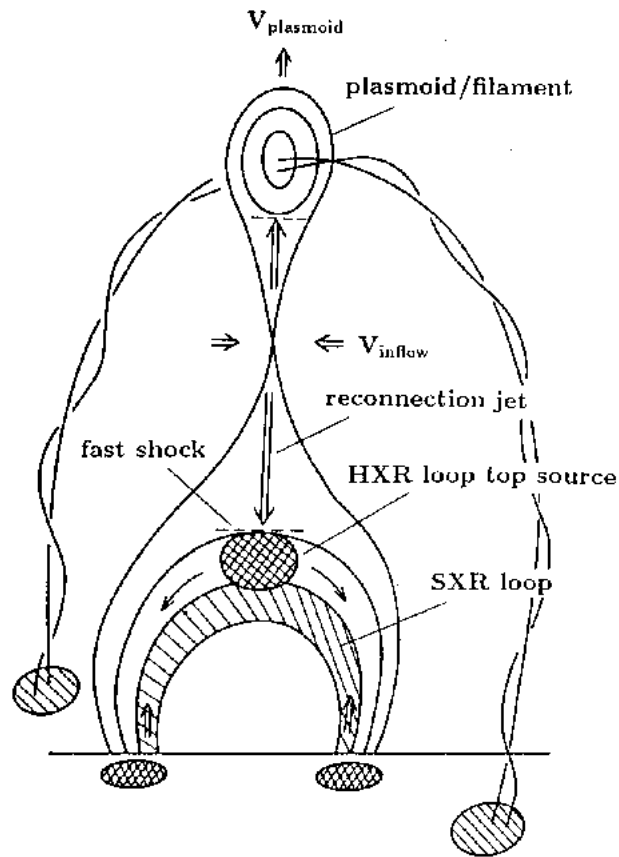


Fig. 1.11: The standard CME model, showing rising and expanding magnetic field lines with embedded filament material above reconnection sites. Image from Shibata et al. (1995).

a CME may or may not occur.

The progenitor for normal CMEs is a strongly sheared or twisted magnetic field configuration which has stored a large amount of nonpotential energy. These metastable structures may be disturbed, rise and expand, and release this energy by reconnecting and reconfiguring with the surrounding field. This rise is shown in the schematic presented in Figure 1.11 (Shibata et al. 1995). The reconnection beneath the rising plasmoid in this figure is thought to be the driver of flares: sudden, short-lived but very intense brightenings across many wavelengths (though most notably $H\alpha$ and X-rays). Although frequently seen together, both flares and CMEs are thought to be symptoms of a magnetic instability, rather than one triggering the other (Chen 2011).

This standard model has been expanded upon and modified by several

bodies of work. The breakout model describes how an eruption may be triggered in a sheared arcade containing a filament channel by the magnetic structure reconnecting with the overlying and surrounding field (Antiochos and DeVore 1999; Lynch et al. 2004). This removes the constraint above the filament channel and allows it to rise and erupt. Another proposed source of the instability is reconnection of the lower parts of the sheared arcade itself into a flux rope structure, removing magnetic field rooted in the surface from the structure, a process known as tether-cutting (Moore et al. 2001; Goff et al. 2007). A third mechanism for triggering eruptions comes from the twist of the flux rope which, if it reaches a critical point, will deform into a helical structure, known as the kink instability. The apex of the flux rope has an exponential rise in height for the linear phase of the instability, causing an eruption (van Ballegooijen and Martens 1989; Williams et al. 2005). Additionally, the torus instability is emerging as a universal trigger mechanism, which describes how a \sim circular ring of twisted magnetic field is unstable against expansion if the overlying field is sufficiently weak. The kink instability provides an avenue for this condition in flux ropes, by not only forming smooth curves in the flux rope (*i.e.*, arcs of circles) but also by rapidly increasing the height of the flux rope, where overlying magnetic fields will be weaker due to the radial expansion (Kliem and Török 2006).

In the breakout model, the energy is stored in the shear of the arcade, while in the kink and torus instabilities it is primarily in the twist of the flux rope, with tether-cutting reconnection lying somewhere between the two. However, it could be argued that the energy stored in the twist of a flux rope initially arose from shear in the footpoints of a magnetic arcade. If an eruption is triggered by a sheared arcade, *i.e.*, with no flux rope, one will form during the eruption.

The average mass of a CME is approximately 3×10^{15} g with the kinetic and potential energy of a typical CME amounting to 10^{22-25} J. Order of magnitude estimates for the available energy in the low solar atmosphere suggest that the origin of this energy must be magnetic. The front of a CME can move with a velocity of anywhere from 100 to upwards of 3,000 km s⁻¹,

though the average lies close to 300 km s^{-1} . As they expand radially away from the Sun into interplanetary space, the angular width remains relatively constant, meaning the volume occupied by the mass and magnetic field swells out. CMEs are most commonly observed moving outwards in the ecliptic, due to low latitudes being the prime location of active regions, and the large-scale structure of the solar magnetic field ‘bending’ towards the equator, guiding the CME. For a thorough review of CMEs, see Chen (2011).

If a CME is ejected towards us, then after anywhere between two and five days travel time, these bundles of plasma and magnetic fields can interact with the Earth’s magnetosphere. The Dungey cycle describes how the front of the CME reconnects with geomagnetic fields, sweeping the field lines back over the Earth, which build up in density, triggering further reconnection on the night-side of the planet, releasing the solar plasma into the atmosphere in polar regions. The resulting magnetic storms have the potential to interfere on a large scale with many different aspects of modern technology; GPS and radio communications are disrupted by ionospheric currents, magnetic vibrations may induce currents at ground level, and there is a radiation risk for polar regions (particularly applicable to trans-polar flights). The geomagnetic storm which occurred in March 1989 caused the collapse of Hydro-Québec’s electricity transmission system, leaving 6 million people without electricity for 9 hours and costing the Canadian economy \$2 billion – a highly geoeffective storm. Such a magnetic storm now, causing only a single day’s loss of GPS and electricity, could cost the UK economy over £10 billion². For such reasons, ‘space weather’ has become a focus of appreciable interest in recent years, and a better fundamental understanding of the processes involved could lead to the ability to better predict events and protect our technology-dependent world from this harsh, unforgiving environment.

On the 14th and 15th of March 2015, a particularly interesting pair of eruptions occurred from NOAA Active Region 12297 and an associated IF to the west, with one leg originally rooted in the AR and the other in diffuse magnetic field, shown in the top left pane of Figure 1.12. AR12297 underwent

²From a presentation by AirBus at MSSL 10th June 2015

first a failed eruption at 11:45 UT on the 14th, followed by another (successful) eruption at 00:40 UT on the 15th. The first eruption casts material to higher points in the solar atmosphere, but this is constrained by the overlying arcade. A small condensation is seen to form above the IF, supported as a static structure in the dips of field lines, with one leg rooted in the strong positive concentration of the AR, and the other in the diffuse negative polarity field surrounding the south and west of the AR. This is highlighted in the top right and bottom left panes of Figure 1.12. The second eruption causes this filament to be ejected into the heliosphere, and bright loops are seen to form where the small concentration had been supported, seen in the bottom right pane of Figure 1.12. The second eruption is accompanied by a CME, which was predicted to have a 40-60% chance of causing a geomagnetic storm, however, as the wake of the CME passed into the Earth's magnetosphere, the most geoeffective magnetic storm of the current solar cycle was induced. The mass involved with these eruptions is studied in Chapter 5.

Another unusual filament eruption occurred on the 7th of June 2011 at roughly 06:00 UT. The precursor filament was embedded in an active region, with two other similarly sized active regions close by to the east. The filament itself did not appear unusual in shape or size, at roughly 4×10^4 km in length, and is shown in the top left of Figure 1.13. However, an unusually high amount of flux cancellation was found to take place within the active region for four days leading up to the eruption (van Driel-Gesztelyi et al. 2014). The material expanded in area on the plane-of-sky to around two orders of magnitude greater than the initial footpoint separation squared (a large-scale view of the eruption is shown in Chapter 3).

After the initial expansion, as a large bulk of the material appeared to reach zero radial velocity (*i.e.*, just before falling back to the surface), bubbles of diffuse coronal material were seen expanding into the erupted cloud of material, radially outwards from the Sun, and thin spikes and fingers of the more dense erupted material was seen extending in the opposite direction, interpreted as occurrence of the Rayleigh-Taylor instability (Innes et al. 2012). This material is analysed in Chapter 4. As this cloud expanded, much of the

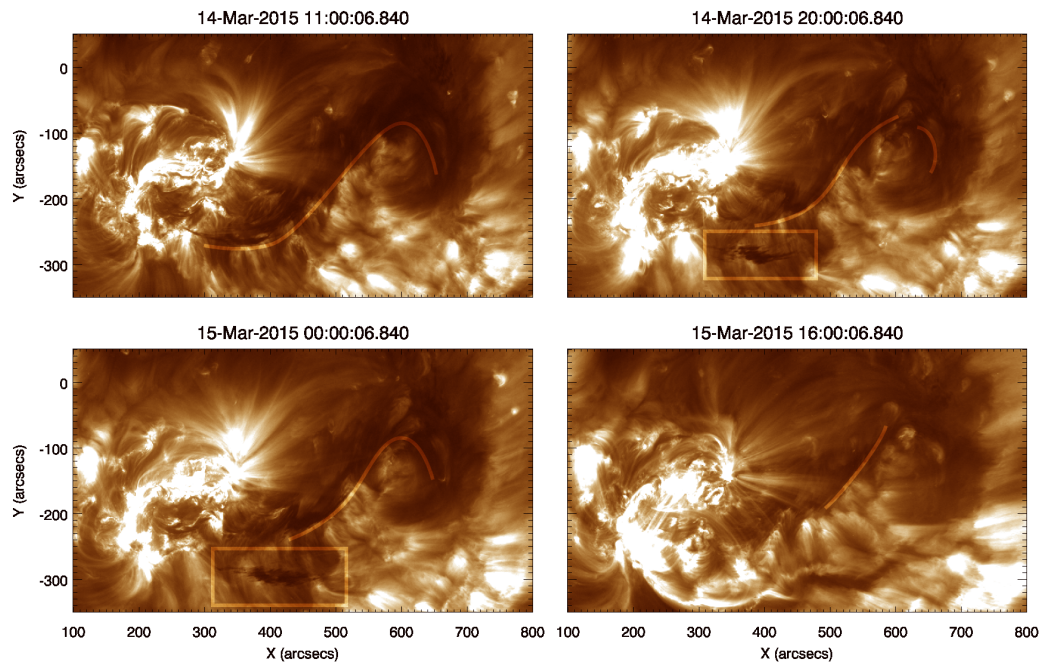


Fig. 1.12: AR12297 with the associated IF protruding to the west shown in the 193 \AA channel of SDO/AIA. The images have been corrected for solar rotation and as such only the first image axes are accurate co-ordinates. The first image (top left) is before both eruptions with a line drawn just to the south of the IF to highlight its position, the next two (top right, bottom left) are between the two eruptions with the IF and smaller filament highlighted, and the final image (bottom right) is some time after the second eruption with the remaining IF highlighted.

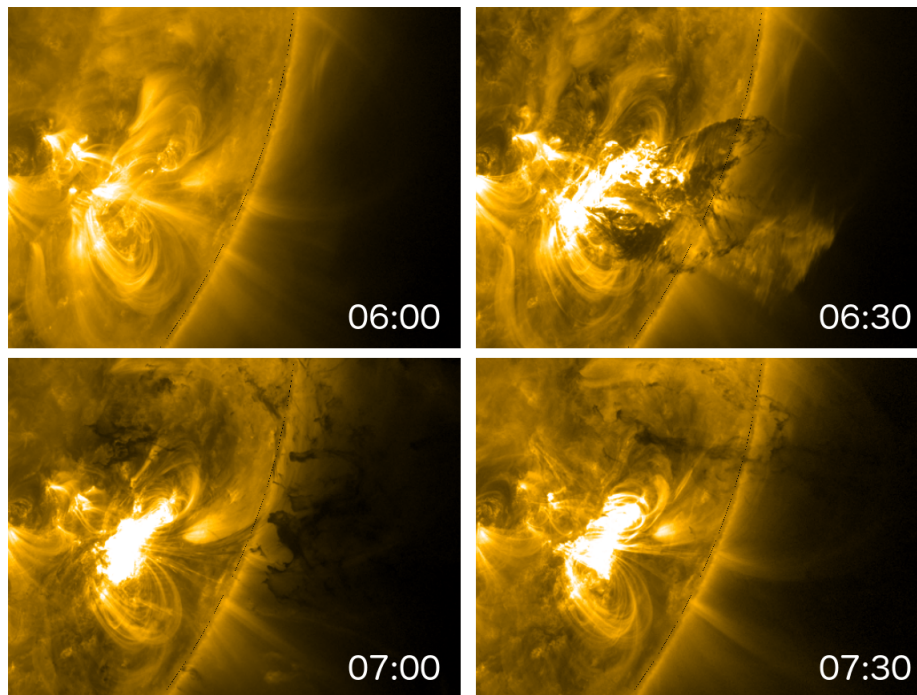


Fig. 1.13: The CME on the 7th of June 2011, seen in the EUV 171 Å channel by SDO/AIA (see Section 2.1). Times are UT. Original image using SDO/AIA data.

material started falling back toward the solar surface, fragmenting into discrete condensations of matter. These blobs of falling plasma are analysed in Chapter 3 and by Carlyle et al. (2014). Reconnection of magnetic field lines between the eruption site and the neighbouring active regions was observed shortly after the initial eruption, which marks the first direct evidence of a CME magnetically reconnecting with surrounding magnetic fields, studied by van Driel-Gesztelyi et al. (2014).

1.3 The Rayleigh-Taylor Instability

The material ejected by the the 7th of June 2011 CME has been shown to be Rayleigh-Taylor unstable (Innes et al. 2012; Carlyle et al. 2014) (also detailed in Chapters 3 & 4); the Rayleigh-Taylor instability (henceforth referred to as RTi) occurs when a fluid is supported against gravity (or otherwise accelerated) by another fluid of lower density, whereupon a fingering instability of the interface occurs; that is, spikes of the higher density fluid penetrate downwards whilst bubbles of the lower density fluid grow and rise upwards (Sharp 1984).

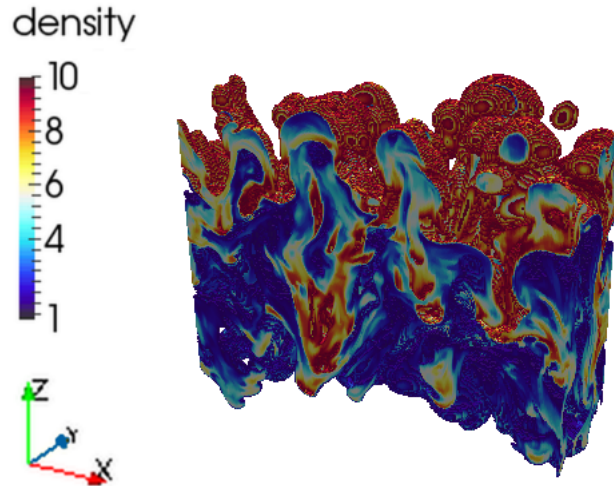


Fig. 1.14: The mixing region between fluids of density 1 and 10, where the pure fluids above and below the mixing region are not shown. Original image of simulation run with the Athena astrophysical MHD code (see Chapter 4).

Figure 1.14 demonstrates the appearance of the RTi, showing the mixing layer of a simulation of the instability.

The RTi is thought to play an important role in many aspects of solar physics. For example, it has been shown to form the filamentary structure in emerging flux (Isobe et al. 2005), observed in upflows in prominences (Hillier et al. 2012), as a mechanism for supra-arcade downflows (Guo et al. 2014) and influenced the break-up of plasma following the the 7th of June 2011 CME.

If the fluids involved are inviscid and perfectly conducting and a magnetic field is present (in both fluids), the growth rate of the rising bubbles in the linear phase γ is given by Chandrasekhar (1961):

$$\gamma^2 = gkA - \frac{\cos^2\theta k^2 B_x^2}{2\pi(\rho_u + \rho_l)}, \quad (1.23)$$

where: g is the gravitational acceleration; k is the wavenumber of the instability; A is the so-called Atwood number, defined as $(\rho_u - \rho_l)/(\rho_u + \rho_l)$, with ρ being density and the subscript denoting the density of the upper and lower fluids respectively, B is the magnetic field strength, and θ is the angle between k and B ; in this case \mathbf{B} is along x . The linear phase of the RTi describes the initial onset, where only first order perturbations are important in describing the system. If equation 1.23 is below zero then γ is imaginary and the sys-

tem is stable, and any perturbations will produce waves in the interface. If γ is real, the system is unstable and any perturbations will give rise to the bubbles and spikes described. Therefore the most unstable wavelength of the instability, *i.e.*, the dominant length scale in separation between successive bubbles/fingers, will be at the peak of the distribution of $\gamma(k)$, that is where $\partial\gamma/\partial k = 0$:

$$2\gamma \frac{\partial\gamma}{\partial k} = gA - \frac{2\cos^2\theta k B_x^2}{2\pi(\rho_u + \rho_l)}, \quad (1.24)$$

and so,

$$gA = \frac{2\cos^2\theta k_u B_x^2}{2\pi(\rho_u + \rho_l)}, \quad (1.25)$$

where k_u is the dominant wavenumber (along the magnetic field). Rewriting,

$$\frac{2\pi}{k_u} = \lambda_u = \frac{2\cos^2\theta B_x^2}{g(\rho_u - \rho_l)}, \quad (1.26)$$

where λ_u is the dominant growth scale of the undular mode (*i.e.* along the direction of the magnetic field) of the instability. Therefore we can express magnetic field strength (along x) in terms of this:

$$B_x = \sqrt{\frac{g\lambda(\rho_u - \rho_l)}{2\cos^2\theta}}, \quad (1.27)$$

where λ would be an observed separation.

The nonlinear phase of the instability is reached approximately when the height of the rising bubbles has reached scales of the order of the wavelength of instability. In this regime, their height relative to the original interface is found to be proportional to time squared, and commonly stated for the hydrodynamic case as

$$h = \alpha A g t^2, \quad (1.28)$$

where h is the height from the initial interface which the mixing region has penetrated the denser fluid (Youngs 1989). The coefficient α is insensitive to A and g and has been determined from simulations as being approximately 0.057 but found in laboratory experiments to be approximately 0.025 (Dimonte et al. 2004). Glimm et al. (2001) conclude that numerical dissipation effects, such as mass diffusion and viscosity, due to algorithmic differences and differences in simulation duration, are the main reasons for the observed spread in nonlinear growth rate across studies.

Jun et al. (1995) studied the linear and nonlinear regimes of the RTi using 2D MHD simulations, investigating the effect of a magnetic field tangential to the initial interface as well as fields normal to this. They found enhanced growth in the latter case, the material collimating along field lines as the instability sets in. However, there is an upper limit to the magnetic field strength, beyond which the growth is greatly suppressed.

The nonlinear phase has been studied in 3D MHD simulations; for example, Stone and Gardiner (2007a) showed how the shape of resulting bubbles is affected by magnetic field configuration, and Stone and Gardiner (2007b) demonstrated that the instability was slowed by the addition of a strong magnetic field during the initial onset of the instability. At later times, the nonlinear growth rate was actually enhanced relative to the hydrodynamic case due to the suppression of mixing between the fluids, which occurs through secondary Kelvin-Helmholtz roll-ups at the edges of the bubbles and fingers. A thorough overview of the RTi is given by Sharp (1984). Unfortunately, there have been no further 3D numerical studies examining the effects of magnetic fields on the nonlinear development of the RTi.

Chapter 2

Instrumentation

The observational data used in this thesis are EUV images captured by spaceborne instruments. The filament material studied is clearly visible in absorption at these wavelengths, and the column density is calculated from the change in intensity over the wavelengths observed (see Chapter 1). The Solar Dynamics Observatory was the main source of data used in the observational analysis in this thesis (specifically the Atmospheric Imaging Assembly (AIA) instrument on-board), and so this is described here in detail. Some images gathered by the Solar TERrestrial RELations Observatory (STEREO) were also used to make qualitative judgement of erupted filament material, and so this spacecraft and the EUV telescope is also described.

2.1 The Solar Dynamics Observatory (SDO)

SDO is a satellite launched by NASA in February 2010 which aims to understand the physics of solar variations that influence life on Earth. The satellite sits in an inclined geosynchronous orbit with near-continuous view of the Sun with three experiments on board SDO: an array of telescopes imaging the surface and atmosphere of the Sun, known as AIA (see Section 2.1.1); a collection of instruments to measure fluctuations in the ultraviolet output of the Sun, known as the Extreme Ultraviolet Variability Experiment (EVE); and the Helioseismic and Magnetic Imager (HMI), which maps magnetic and velocity fields at the surface, producing dopplergrams and LOS and vector magnetograms. No data is stored on board the satellite, but is continuously transmitted to two dedicated ground stations in New Mexico, USA, through

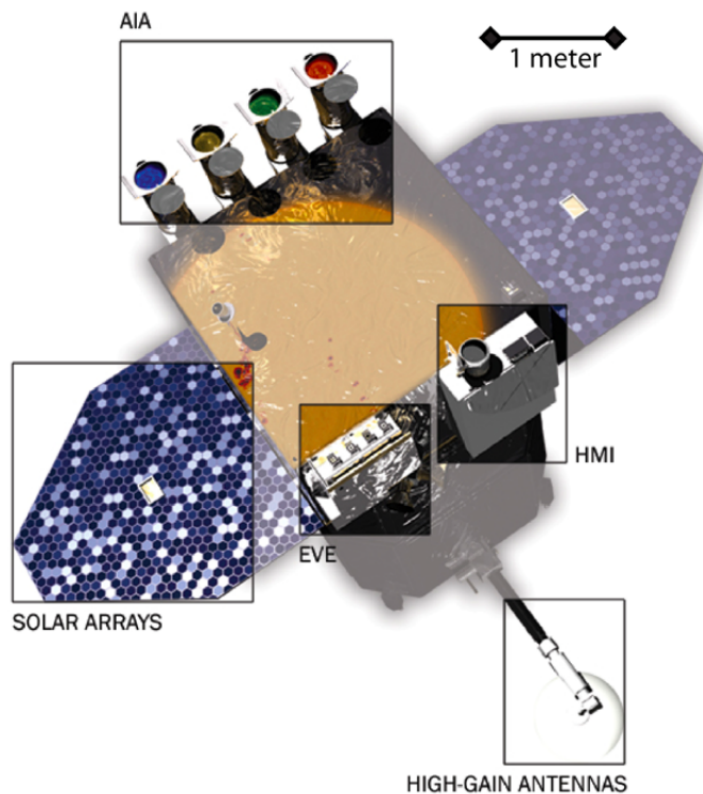


Fig. 2.1: The Solar Dynamics Observatory with instruments, solar arrays and high-gain antennas highlighted (from Pesnell et al. (2011)).

a set of high-gain antennas.

A main strength of the SDO mission is the high temporal and spatial cadence of all three experiments, which, coupled with the continuous full-disc view of the Sun, provides unprecedented insight into the fine structure and dynamics of the fascinating solar atmosphere. This generates large amounts of data very rapidly, and approximately 1.5 terabytes of data are downloaded every day.

The satellite itself, weighing 3,000 kg at launch (300 kg in instrumentation, the 1,300 kg spacecraft and 1,400 kg of fuel), is a fully redundant spacecraft with three-axis stabilisation and is shown in Figure 2.1. The prime science mission is planned for five years, however, there is sufficient propellant on board to operate for up to ten years. The instruments on board are powered by 6.6 m² of solar panels, providing 1,500 W of power and expected to work with 16% efficiency after the initial 5 years.

Wavelength (Å)	Primary ion	Char. log(T) (K)	Location
94	Fe XVIII	6.8	Flaring corona
131	Fe VIII / XXI	5.6 / 7.0	Transition region, flaring corona
171	Fe IX	5.8	Quiet corona, upper transition region
193	Fe XII / XXIV	6.2 / 7.3	Corona, hot flare plasma
211	Fe XIV	6.3	Active region corona
304	He II	4.7	Upper chromosphere
335	Fe XVI	6.4	Active region corona
1600	C IV (& cont.)	5.0	Transition region, upper photosphere
1700	Continuum	3.7	Photosphere (temperature minimum)
4500	Continuum	3.7	Photosphere

Table 2.1: Wavelengths observed by SDO/AIA.

The information in this section is from Pesnell et al. (2011).

2.1.1 The Atmospheric Imaging Assembly (AIA)

AIA began capturing data on the 27th of March 2010 and has since been providing full-disc images with unprecedented resolution and cadence, revealing the breathtaking structure of the solar atmosphere in a way which has not before been seen. It consists of four cassegrain telescopes which provide Sun-centred images up to $0.5 R_{\odot}$ from the limb in ten bandpasses (almost) simultaneously. The images are of a spatial resolution of $1.5''$ and (baseline) cadence of 12 seconds (which may be shortened for chosen transient phenomena), in order to capture the highly dynamic structures in the corona.

The data are captured by the narrow-band imaging of seven EUV band passes, as well as continua in UV and visible light; the full list of wavelengths observed are described in detail in Table 2.1. An image in each of these is shown in Figure 2.2, as well as three HMI images. The transmission profiles of the filters have a full-width-half-maximum (FWHM) of roughly two angstroms, however this is not a problem for the methods used in this thesis, as the wavelength-dependent variables have small change over such scales (see Section 3.2).

The temperature response for the seven main EUV filters is shown in Figure 2.3. It can be seen here that they are all relatively wide and uneven,

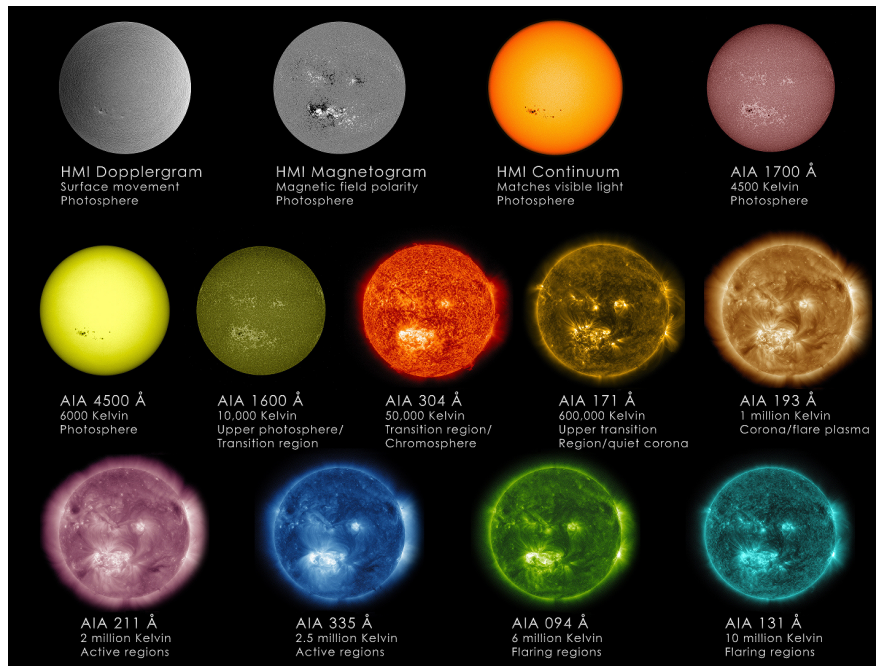


Fig. 2.2: AIA images in each bandpass, as well as three HMI images. Image credit: NASA/SDO/AIA.

indicating that material at a range of temperatures is captured by each of these filters, and care must be taken when using the characteristic temperatures presented in Table 2.1. Fortunately, this does not affect the work in this thesis, as the intensity is measured in the context of absorbing material which is far below these coronal temperatures.

The filters on the AIA are metal layers supported at the aperture of each telescope by a nickel square-pattern mesh, and in a filter wheel located in front of the focal plane. Aluminium is used for wavelengths $\geq 171 \text{ \AA}$, and zirconium for the shorter two wavelengths. One telescope contains a selector mechanism rather than the filter wheel, which are used to select channels of interest; this telescope observes the UV and visible continua. The layout of the telescopes is shown in Figure 2.4.

Each telescope has a 20 cm primary mirror and an active secondary mirror, providing a low coefficient of thermal expansion and polished to achieve a spatial frequency range from $10^{-3} - 5 \times 10^{-2} \text{ nm}^{-1}$. A cross section of one telescope is shown in Figure 2.5.

At the focal plane of each telescope is a 4096×4096 pixel CCD sensor.

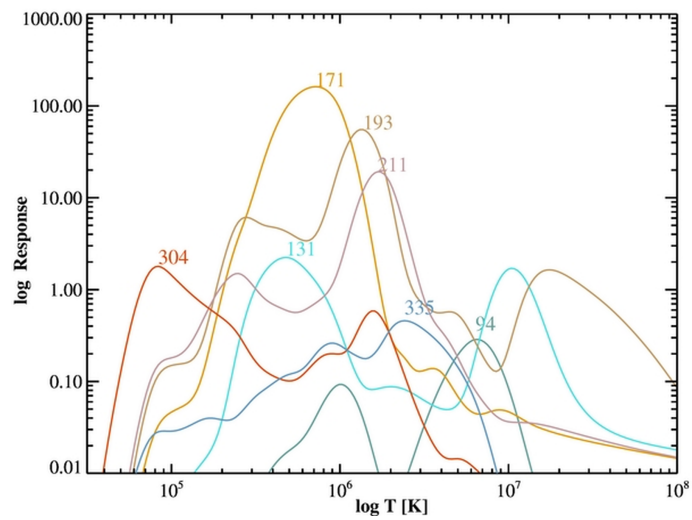


Fig. 2.3: Temperature response of the seven standard EUV filters (from Downs et al. (2012)).

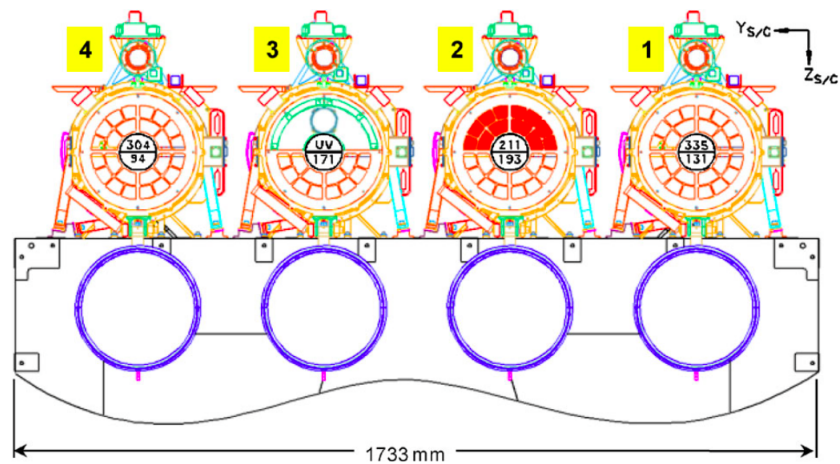


Fig. 2.4: The layout of the wavelength channels in each of the four AIA telescopes. The top half of telescope number 3 has a window with a coating centred at 1600 \AA (from Lemen et al. (2012)).

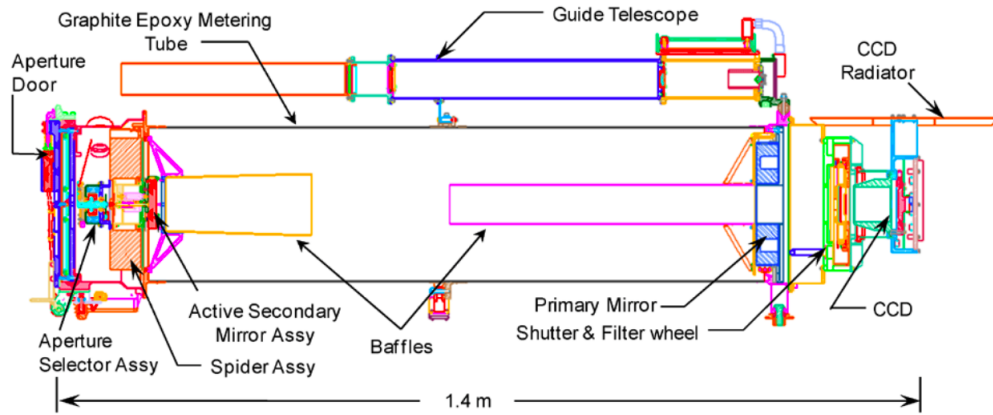


Fig. 2.5: Cross section of AIA telescope 2; each telescope has its own guide telescope to stabilise the image on the CCD (from Lemen et al. (2012)).

The detectors have a full well of more than 150 000 electrons, with typically $18 \text{ e}^- \text{ photon}^{-1}$ (for 193 \AA). Each quadrant of each CCD has an amplifier which the electrons in each pixel are transferred to; the induced voltage is measured and converted to Data Number (DN) by an analogue-to-digital converter (ADC). The four quadrants are read out simultaneously, at a rate of 2 Mpixels s^{-1} with less than 25 electrons of read noise, and almost lossless data compression. Each pixel is $12 \text{ }\mu\text{m}$ and corresponds to a view of $0.6''$ (where $1''$ corresponds to approximately 725 km at the Sun-Earth distance).

The raw data, referred to as Level 0, are stored as 16-bit integer 4096×4096 arrays and immediately compressed. Level 1 data processing involves several procedures to correct for various instrumental effects. ‘Over-scan’ rows of pixels are removed, a dark image is subtracted (to account for digital offset of the camera, CCD read noise and dark current), flat-field correction, dead pixel removal, and finally the images are flipped so as to put solar north at the top.

Light passing through the entrance filters is diffracted by the mesh supporting it, which, coupled with contributions from the mirrors and CCD, causes a point spread function (PSF). This is not corrected for in the Level 1 data processing, and so images should be deconvolved according to this PSF before observations made by the instrument are used in intensity analysis, such as in the work conducted in this thesis. This is described in detail by Grigis

et al. (2012).

The data may then be processed further into Level 1.5, which allows the images to be more easily presented as a movie. This is achieved by rotating the images so solar north is at 0° , a plate-scale adjustment which ensures that each pixel scales to exactly $0.6''$, then co-aligning the images. However, this was not necessary for the work undertaken in this thesis, as co-alignment is performed on each target individually.

Level 1 and 1.5 data products are sent to the Smithsonian Astrophysical Observatory, which acts as a data-distribution center, and can be accessed through the Virtual Solar Observatory (VSO), an online database of the major sources of solar data.

Much of the information in this section is from Lemen et al. (2012).

2.2 Solar TERrestrial RELations Observatory (STEREO)

The STEREO mission was launched by NASA on the 26th of October 2006 and consists of two (nearly) identical satellites, one placed in a heliocentric orbit slightly closer to the Sun than that of the Earth, and the other slightly further away. The result of this is that each satellite moves around the Sun relative to the Earth in opposite directions, giving a full 360° view of the Sun for the first time in human history¹. The mission also observes the Sun-Earth line from two different points of view, providing insight into the propagation of CMEs through the heliosphere. The spacecraft ahead of Earth in its orbit is referred to as STEREO-A, while the spacecraft behind is referred to as STEREO-B.

The main science aims of the STEREO mission are to understand the causes and mechanisms of CME initiation and characterise their propagation through the heliosphere, to uncover the mechanisms and sites of energetic particle acceleration in the low corona, and to determine the structure of the ambient solar wind. To achieve these aims, each satellite utilises a collection of instruments: the Sun Earth Connection Coronal and Heliospheric Investigation (SECCHI) consists of an extreme ultraviolet imager, two white-light coronagraphs and a heliospheric imager; STEREO/WAVES (S/WAVES)

¹this was achieved February 6th 2011

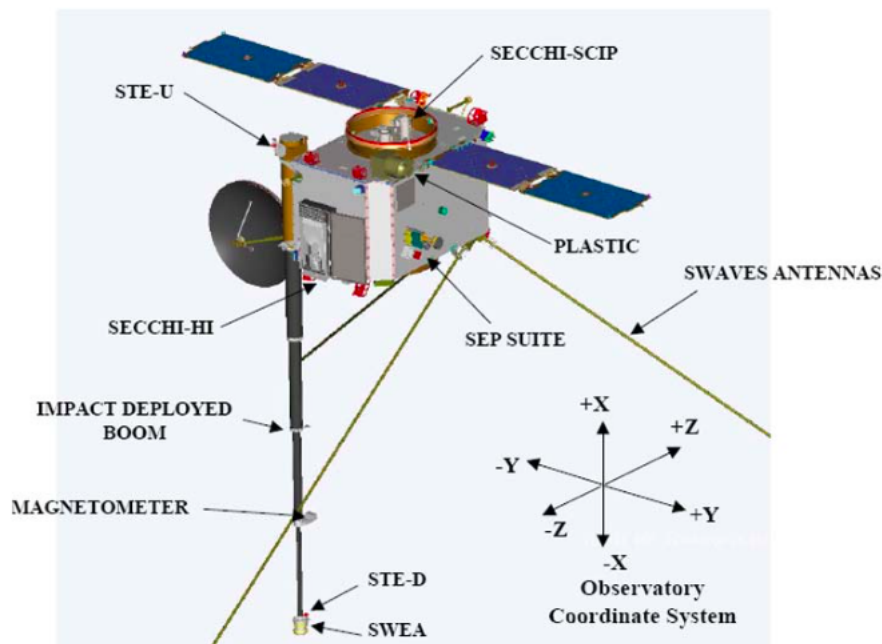


Fig. 2.6: STEREO with instrumentation highlighted (from Driesman et al. (2008)).

traces radio disturbances along the Sun-Earth line; In-situ Measurements of Particles and CME Transients (IMPACT) is an instrument which measures plasma characteristics of solar energetic particles and the local vector magnetic field; PLAsma and SupraThermal Ion Composition (PLASTIC) provides plasma characteristics of protons, alpha particles and heavy ions. Only the Extreme Ultraviolet Imager (EUVI) in SECCHI is used in this thesis.

Both STEREO spacecraft have selective redundancy and 3-axis stabilisation. Each had a launch mass of 620 kg (including propellant) and are powered by two large solar arrays. The collected data is stored on the 1GB solid state recorder and downloaded to the STEREO ground station network during a daily realtime pass. On top of this, there will also be a continuous telemetry stream of approximately 633 bits per second to provide continuous monitoring of the heliospheric conditions, known as the space weather beacon. The spacecraft is shown in Figure 2.6 with instrument labels.

2.2.1 Extreme Ultraviolet Imager (EUVI)

The EUVI are normal-incidence Ritchey-Chrétien telescopes (one on each STEREO spacecraft) with metal filters, multilayer coated mirrors, and

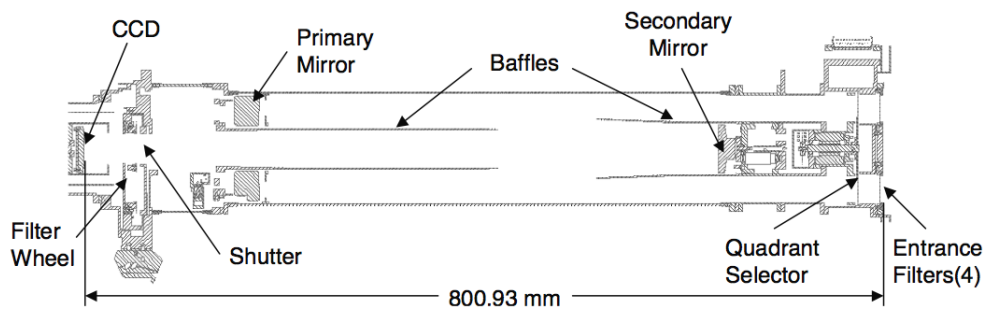


Fig. 2.7: Cross-sectional view of one of the EUVI telescope on STEREO (from Wuelser et al. (2004)).

2048 × 2048 pixel detectors, which observe the low corona and chromosphere. A cross section of one of the EUVI is shown in Figure 2.7. Four EUV lines are measured using narrow-bandpasses at 171, 195, 284 and 304 Å, and the data gathered have a spatial resolution of 1.6'' and a variable temporal resolution (nominally one image will be taken every 2 or 3 minutes) in a circular, full-Sun field of view up to 1.7 R_⊙.

Chapter 3

Density and Dynamics of In-Falling Material Following the 2011 June 7 Eruption

I would like to thank David Williams, Lidia van Driel Gesztelyi, Davina Innes and Andrew Hillier for guiding me through the first project of my PhD. The contents of this Chapter have been published in *The Astrophysical Journal* and *Proceedings of the International Astronomical Union* (see Chapter 7).

The 7th of June 2011 eruption (described in Section 1.2.2) is a fascinating event and a unique set of observations. Such a large amount of material has never been seen to fall back to the solar surface following an eruption by SDO/AIA, and I was interested to learn why this material appeared so dark in the EUV band passes. I decided to investigate whether the cause of this is a particularly high mass (or, rather, density) of material, and the first project in this PhD centres around determining the column density of several of the discrete condensations of erupted filament material as they fall back through the solar atmosphere (“in-falling blobs”). In order to do this, I further developed the method of column density calculation first used on AIA data by Williams et al. (2013), also described by Special Case I in Landi and Reale (2013), which estimates total hydrogen column density by measuring how much radiation from the background corona/chromosphere is occulted by these blobs.

As the blobs fall through the atmosphere, a self-similar bifurcation is

seen repeatedly, which visually conforms with the RTi. This morphology is occurring between a lower density fluid (the corona) and a fluid of higher density (the blobs), a system which is (the requirement for a system to be) RT-unstable. This means that equations governing this instability can be applied to the observed length scales and measured mass/density. This allows for an order-of-magnitude estimate of the strength of any embedded magnetic field, which may strengthen or refute the speculation that this is an occurrence of the RTi.

3.1 Observations

The analysis of the erupted material was performed using images collected by SDO/AIA (see Section 2.1) between 06:40 and 08:40 UT on the 7th of June 2011 in the 94, 131, 171, 193 and 211 Å passbands. The eruption occurred from NOAA active region 11226, which was in the south-west quadrant of the visible disc at the time, and most of the in-falling material passed over this quadrant upon returning to the Sun. Figure 3.1 shows some of these blobs as they first crossed back onto the south-west limb as seen by SDO/AIA.

STEREO-A/SECCHI (see Section 2.2) images were also used for a qualitative examination of the geometry of the blobs analysed. At the time the observations were taken, the Sun-STEREO-A line was approximately orthogonal (94.8°) to the Sun-Earth line, allowing for optimal assessment of its extent along this line, *i.e.*, its ‘depth’ into the plane-of-sky viewed from Earth. Figure 3.2 shows a snapshot of the eruption as seen by STEREO-A/SECCHI, which shows similar structures to those seen in AIA (by visual inspection). This suggests that the blobs are approximately as deep as they are wide, and as such are assumed to be this deep for the purpose of estimating a volume density from column density.

The targets selected for study are four distinct blobs which appear to remain as reasonably coherent structures along their long, unobscured descent. The absorption depth of these is measured at roughly equal intervals as they pass across the solar disc. The requirement for a relatively quiet background guided the choice of examination times, chosen as points when the material

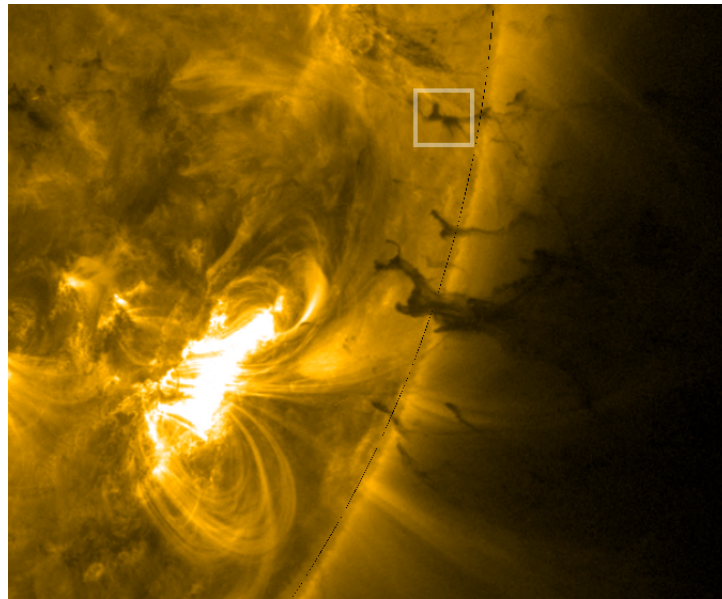


Fig. 3.1: Target blobs crossing back onto the south-west solar limb seen in the SDO/AIA 171 Å passband at 07:10 UT. Target 1 (shown in detail in Figure 3.5 *et al.*) is highlighted. The dark material is falling towards the left of the image having expanded massively from a filament eruption approximately 30 minutes before. Snapshots of this eruption are shown in Figure 1.13.

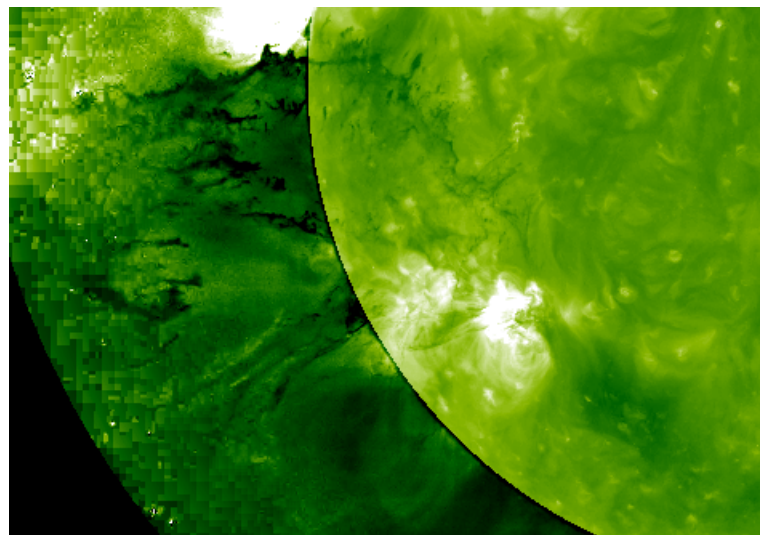


Fig. 3.2: Target blobs crossing back onto the south-west solar limb seen in the STEREO-A/SECCHI 195 Å passband at 07:05 UT.

passes in front of relatively quiet regions. This ensures the best accuracy column density estimate, as it means that the co-spatial background image used is as uniform as possible in the time between target and background frame collection. One target is examined at higher cadence (*i.e.*, more points along its descent) than the other three, as the morphology reminiscent of the RTi is clearly seen in this blob.

3.2 Density Calculation Method

The intensity of radiation received by an observer from material occulting the source of the radiation will depend on the optical depth of the material and the intensity of the source; that is, the absorbing material removes a certain amount of photons from the LOS depending on how many particles lie along this LOS, and the opacity of the material itself (where this work assumes that photoionisation is the dominant process that removes photons from the LOS; see Section 1.1.2). Formally put, the observed obscured intensity I_{obs} is a function of the unobscured background intensity I_b and the optical depth τ :

$$I_{obs} = I_b e^{-\tau}. \quad (3.1)$$

The optical depth is a function of column density N and cross-section for absorption σ ,

$$\tau = N \sigma, \quad (3.2)$$

and so if I_{obs} and I_b are measured (where values for σ have been published from calculations and laboratory experiments), in principle the column density of the material may be calculated. It is important to remember that these equations are wavelength dependent; this is due to photons with shorter wavelengths having higher energy, allowing them to penetrate the ensemble of particles more easily. This is expressed through a smaller photoionisation cross-section σ at shorter wavelength, which gives a lower optical depth τ and a greater obscured intensity I_{obs} . Above a certain wavelength, however, photons will not have sufficient energy to ionise a particular species at all, and so the cross-section for photoionisation suddenly drops to zero, $\sigma = 0$ – this can be seen for He II at 227 Å in Figure 3.3.

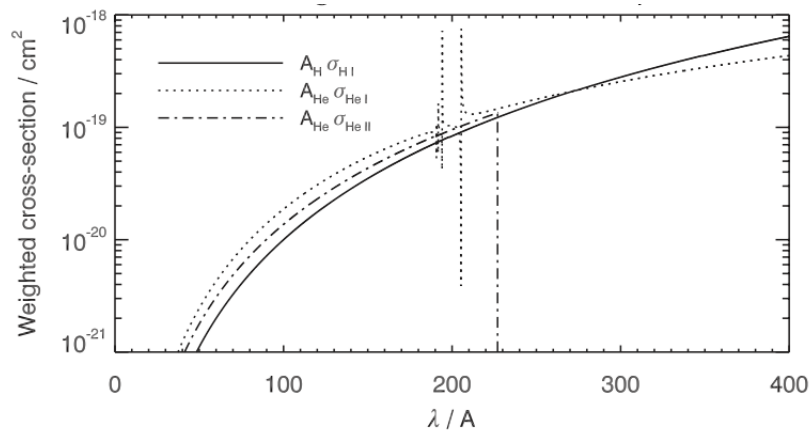


Fig. 3.3: Abundance-weighted photoionisation cross-sections of H and He. From this it can be seen that for these three main populations, the value differs by less than a factor two for the wavelengths observed by SDO/AIA below the He II ionisation edge. Image from Williams et al. (2013).

Photoionisation cross-section σ is not only wavelength dependent, but also species dependent, and the material observed is composed of various particles which are absorbing incident radiation, predominantly H I, He I and He II. Fortunately, for wavelengths below 227 \AA (the photoionisation limit of He II), $\sigma_{He \text{ I}}$ and $\sigma_{He \text{ II}}$ are similar. Furthermore, cross-sections of these three species are very similar when weighted by elemental abundance, as highlighted by Figure 3.3, which shows that $A_H \sigma_{H \text{ I}} \simeq A_{He} \sigma_{He \text{ I}} \simeq A_{He} \sigma_{He \text{ II}}$, were $A_H = 1$ and $A_{He} = 0.0851$ (Grevesse et al. 2007). Therefore,

$$\begin{aligned}
 \tau_{He} &= N_{He \text{ I}} \sigma_{He \text{ I}} + N_{He \text{ II}} \sigma_{He \text{ II}} \\
 &\approx (N_{He \text{ I}} + N_{He \text{ II}}) \sigma_{He \text{ II}} \\
 &\lesssim A_{He} N_H \sigma_{He \text{ II}}.
 \end{aligned} \tag{3.3}$$

For $\lambda < 227 \text{ \AA}$, $\tau_{H \text{ I}} \lesssim \tau_{He}$ and so $\tau_{tot} \lesssim 2\tau_{He}$. The total column density of hydrogen can then be estimated as

$$N_H \gtrsim \frac{\tau_{tot}}{2A_{He}\sigma_{He \text{ II}}}. \tag{3.4}$$

There are some further considerations yet to be made about the intensity of the received radiation, namely that it is not certain that it has all passed through the target material; coronal material between the target and the observer may be in emission, and columns or pixels containing target material are

not necessarily completely occupied by target material. These are accounted for by including in our equations foreground emission I_f and pixel-filling factor f :

$$I_{obs} = I_b [f e^{-\tau} + (1 - f)] + I_f. \quad (3.5)$$

Rearranging,

$$1 - \frac{I_{obs}}{I_b + I_f} = f \frac{I_b}{I_b + I_f} (1 - e^{-\tau}), \quad (3.6)$$

and finally making substitutions for simplicity and including wavelength dependence,

$$d(\lambda) = G (1 - e^{-\tau(N,\lambda)}), \quad (3.7)$$

i.e., the absorption depth $d(\lambda) = 1 - I_{obs} / (I_b + I_f)$, and the geometric depth $G = f I_b / (I_b + I_f)$.

It should be noted that strictly speaking, $I_b + I_f$ is not precisely equal to the intensity of unobscured radiation, *i.e.*, the radiation which would be received in the absence of the target material. The target material which is being measured is occupying space which would otherwise be filled with coronal material which would be in emission; this is referred to as emissivity blocking. The small volume of the target blobs and the low density of coronal material indicate that this emission would be negligible relative to both I_b and I_f , and as such this has not been taken into account. This is not thought to impact the results and is discussed further in Section 3.5.

To obtain a measurement of d at a particular wavelength, the intensity of an image of the target material is used for I_{obs} and a co-spatial image just before or after the target appears in the field-of-view (FOV) is used for $I_b + I_f$, henceforth referred to as the background image. An example of one target blob and its associated background image are shown in Figure 3.5. This is done for the five bandpasses on SDO/AIA below the 227 Å limit (see Table 2.1) and a least-squares minimisation algorithm is used to constrain the two free parameters (G & N_H) in Equation 3.7. A plot showing measures of $d(\lambda)$ at all five wavelengths with the fitted required model is shown in Figure 3.4. This can be thought of as a graphical representation of the fitting of the model: $d(\lambda)$ is measured for five different λ ; these datapoints are then plotted and a

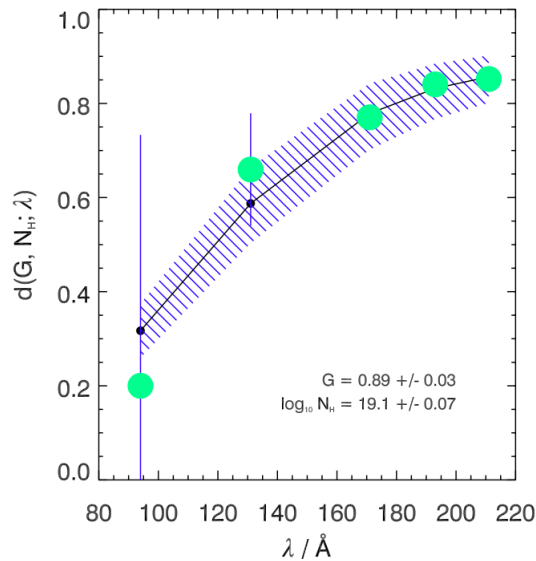


Fig. 3.4: An example of the column density model which has been fit to five data points from SDO/AIA images in a single pixel (from Williams et al. (2013)).

curve of best fit of the form given in Equation 3.7 is drawn over them. Errors are calculated from the square root of the photon count, in turn calculated from the data number (DN) in the SDO/AIA pixels and propagated through the model.

The fitting also returns a measure of the goodness-of-fit for each pixel, χ^2 , which describes the discrepancy between the observed values and the model in terms of the errors on the observations. This becomes the reduced goodness-of-fit, χ_ν^2 , by dividing through by the degrees of freedom; in our case this is 3 (as there are 5 measurements and 2 free parameters; $5 - 2 = 3$). $\chi_\nu^2 = 1$ indicates that the model matches the measurements within the error variance, whilst $\chi_\nu^2 \gg 1$ indicates a poor fit. $\chi_\nu^2 < 1$ suggests the model is ‘over-fitting’ the data, either by an overestimated error variance, or noise is being improperly fitted.

The geometric depth G is a combination of pixel-filling factor and the fraction of emission emanating from behind the target, and can be described as the fraction of received light which has interacted with the target material. Therefore, in the presence of absorbing material with relatively uniform distribution at a sufficient height in the corona, G should approach unity. However,

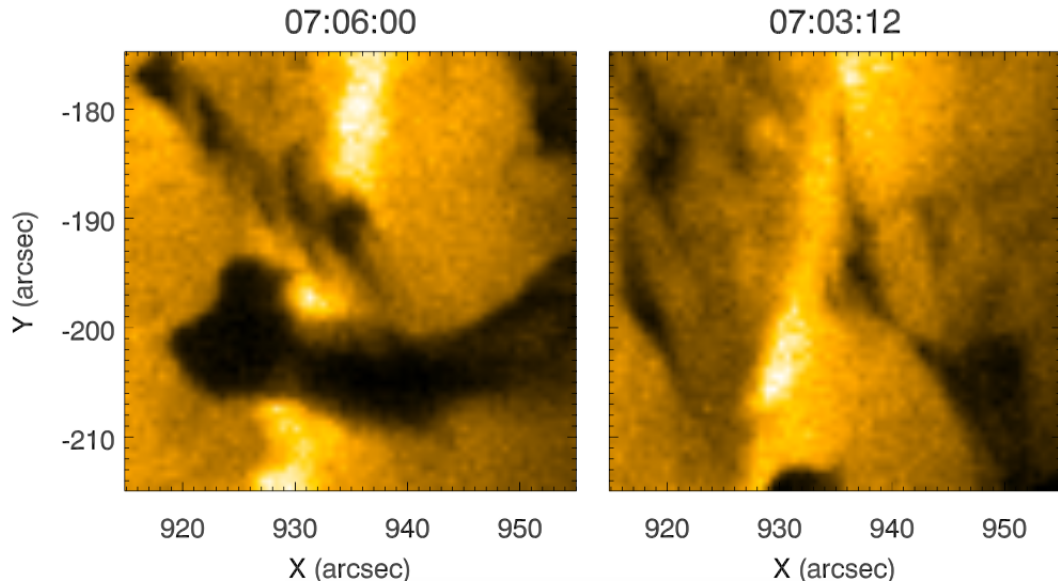


Fig. 3.5: 171 Å images of a target blob (at 07:06 UT, left) and its associated background image (at 07:03 UT, right).

the implication of $G = 1$ is that all of the received radiation originated from background material, with none from the foreground – quite an improbable situation. Furthermore, parameter space in G is finite, bounded between 0 and 1 (as this is the only range over which G is meaningful). The fitted value of G is therefore constrained accordingly, and where the fitted value $G = 1$ suggests that an optimal fit has not been achieved, but that the algorithm has run into a boundary. These pixels are therefore discarded.

Where this value is greater than 0.5, it can be said that the pixel is dominated by absorbing target material, and therefore this cutoff of the geometric depth was used to select target pixels; only locations with $G > 0.5$ are presented in the results. Figure 3.6 shows the target in Figure 3.5 with contours of $G = 0.5$ overlaid, demonstrating how well this aligns with the visual edge of the target. Pixels with a poor goodness-of-fit were also discarded; this was taken as any pixel where χ^2_{ν} deviated from unity by an order of magnitude (or greater).

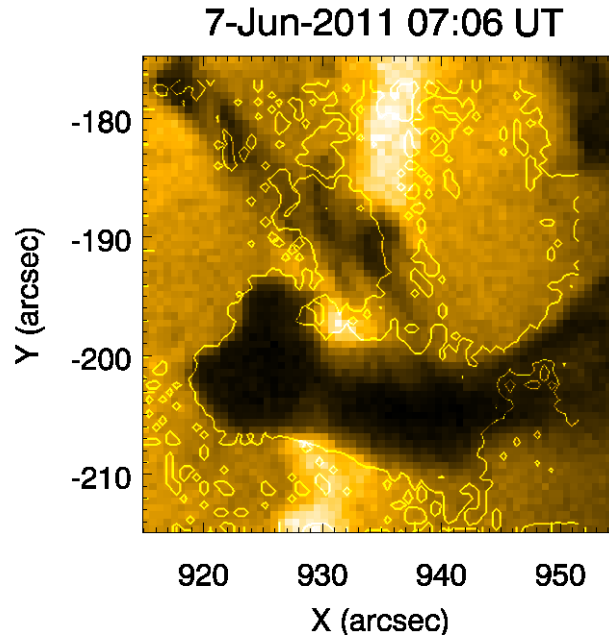


Fig. 3.6: A 171 Å image of the target shown in Figure 3.5 with contours of $G = 0.5$ overlaid.

3.3 Column Density Analysis of In-Falling Material

Figure 3.7 shows the calculated column density and geometric depth values for the target shown in Figure 3.5 at the first point along its descent (Target 1). By comparing Figures 3.7 and 3.5, some of the target towards the lower right of the frame (at roughly $(948'', -203'')$) appears to be omitted from the analysis, and it can be seen from Figure 3.6 that here G falls below 0.5. This is due to the presence of material in absorption at this location in the background image leading to a reduced intensity ratio between the target and background at these points. Although not ideal, this is the most suitable co-spatial background image available.

Calculated column density values of Target 1 as it progresses along its descent are shown in Figure 3.8, and corresponding maps of G are shown in Figure 3.9. The mean column density of hydrogen in this blob is found to have a lower limit of $5.46 \times 10^{19} \text{ cm}^{-2}$ (averaged over the Target) for the first point measured along the descent (07:06 UT). This is seen to gradually rise along the Target's descent, though the number of selected "blob" pixels falls. At 07:15 UT $\bar{N}_H = 5.17 \times 10^{19} \text{ cm}^{-2}$, at 07:27 UT $\bar{N}_H = 5.49 \times 10^{19} \text{ cm}^{-2}$, at

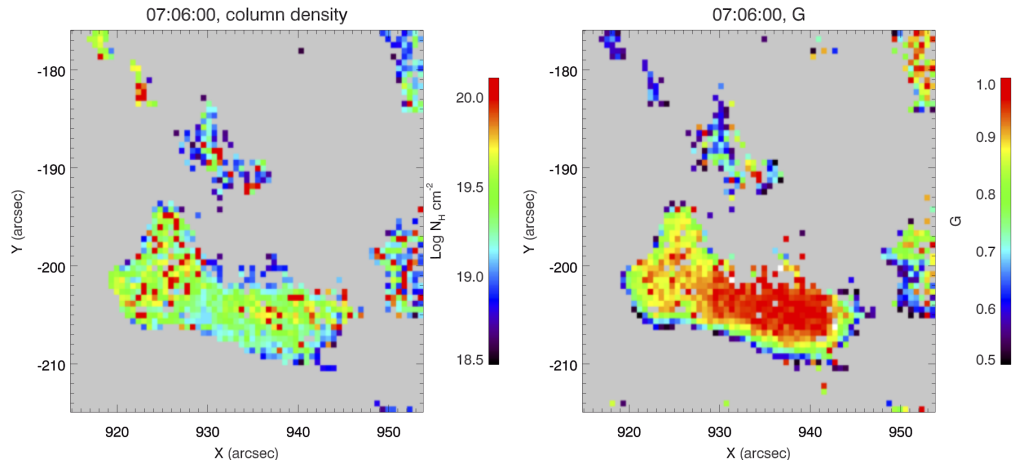


Fig. 3.7: Column density (left) and G (right) maps for Target 1 at 07:06 UT, shown in Figure 3.5. Direction of travel is from right to left, along a line $\sim 40^\circ$ clockwise from the negative x -axis.

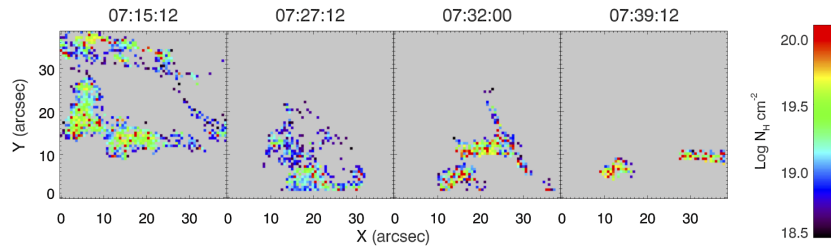


Fig. 3.8: Evolution of the density of Target 1, 07:15 – 07:40 UT, in a frame roughly co-moving with the target. Direction of travel in each frame is roughly towards the upper-left corner of the images.

07:32 UT $\bar{N}_H = 1.12 \times 10^{20} \text{ cm}^{-2}$, and at 07:39 UT $\bar{N}_H = 1.61 \times 10^{20} \text{ cm}^{-2}$. However, the spread of values returned also increases slightly, as shown by Figure 3.10, where a histogram of $\log_{10} N_H$ is shown for Targets 1a and 1d.

G is seen to fall slightly along the descent of Target 1, though only from ~ 0.95 to ~ 0.8 , as demonstrated by Figure 3.11, which shows histograms of geometric depth G for Targets 1a and 1d. This indicates that either the pixel-filling factor is decreasing, implying the appearance of fine structure within the blob (either by formation, or perhaps revealed by a decrease in depth along the line-of-sight), or that as the target material falls to lower heights in the solar atmosphere, a greater proportion of the received radiation is emanating from foreground coronal material.

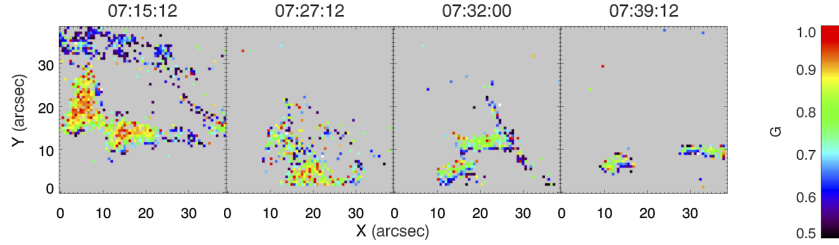


Fig. 3.9: Evolution of the geometric depth of Target 1, 07:15 – 07:40 UT, in a frame roughly co-moving with the target. Direction of travel in each frame is roughly towards the upper-left corner of the images.

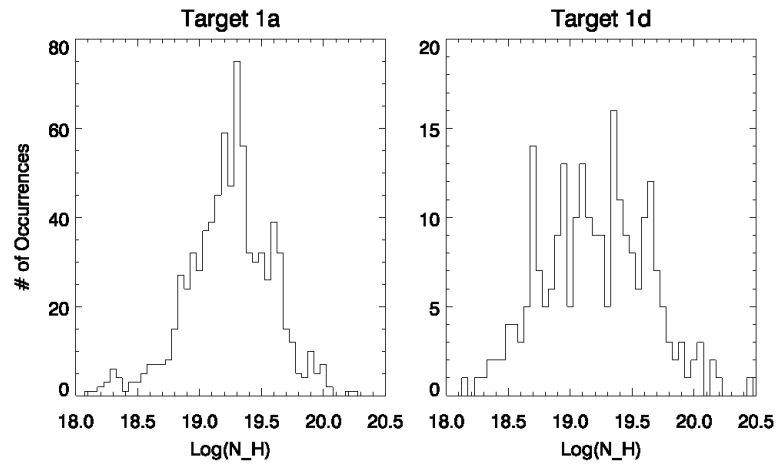


Fig. 3.10: Histograms of N_H for Targets 1a at 07:15 UT (left), and 1d, at 07:40 UT (right). This demonstrates the change in column density as the material falls through the solar atmosphere; also note the different y-axes arising from fewer pixels being selected for 1d than 1a.

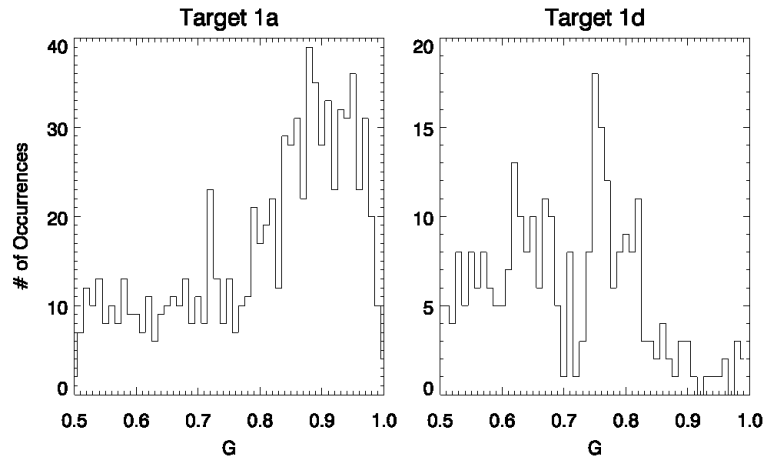


Fig. 3.11: Histograms of G for Targets 1a at 07:15 UT (left), and 1d, at 07:40 UT (right). This demonstrates the change in geometric depth as the material falls through the solar atmosphere; also note the different y-axes arising from fewer pixels being selected for 1d than 1a.

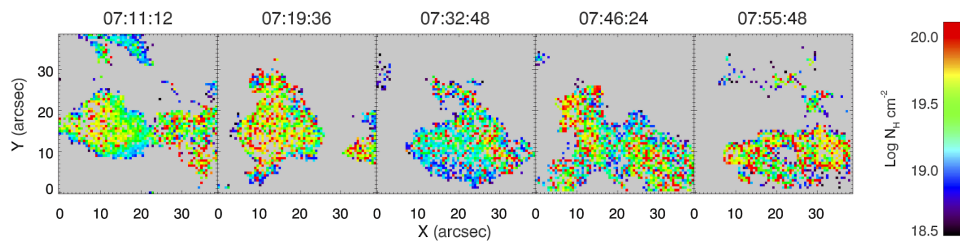


Fig. 3.12: Evolution of the density of Target 2, 07:11 – 07:56 UT. Direction of travel is roughly towards the left side of the images.

Figure 3.12 shows the calculated column density values for Target 2 at five points along its descent (07:11 – 07:56 UT), and Figure 3.13 shows corresponding geometric depth, G . Mean column density is found to be $7.45 \times 10^{19} \text{ cm}^{-2}$ for the first time step (07:11 UT), rising in the same manner as Target 1 to $1.44 \times 10^{20} \text{ cm}^{-2}$ at 07:55 UT.

Figure 3.14 shows the calculated column density values for a third target blob across its descent over the solar disc (07:40 - 08:34 UT), and Figure 3.15 shows corresponding geometric depth, G . Mean column density is found to be $4.25 \times 10^{19} \text{ cm}^{-2}$ for the first time step (07:40 UT), and remains relatively constant over the descent, found to be $6.13 \times 10^{19} \text{ cm}^{-2}$ at 08:33 UT, just before impacting with the solar surface.

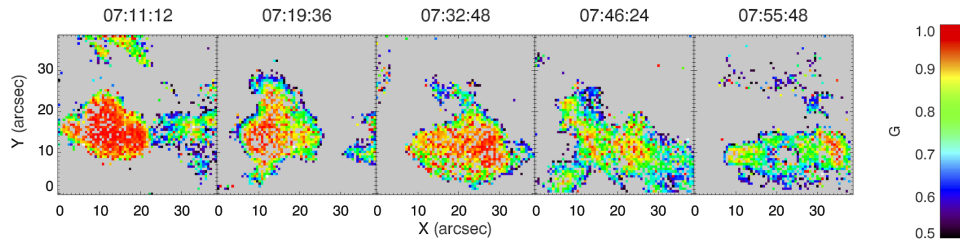


Fig. 3.13: Evolution of the geometric depth G of Target 2, 07:11 – 07:56 UT.

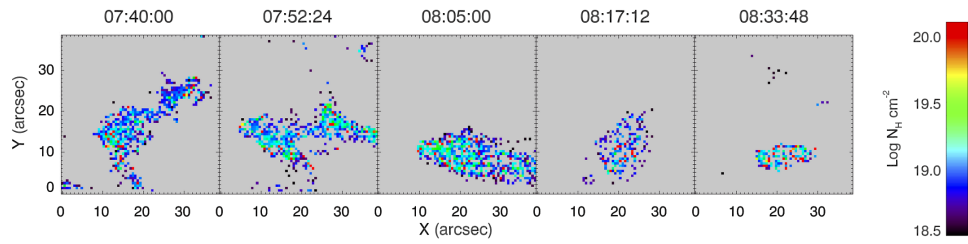


Fig. 3.14: Evolution of the density of Target 3, 07:40 – 08:34 UT. Direction of travel is roughly towards the left side of the images.

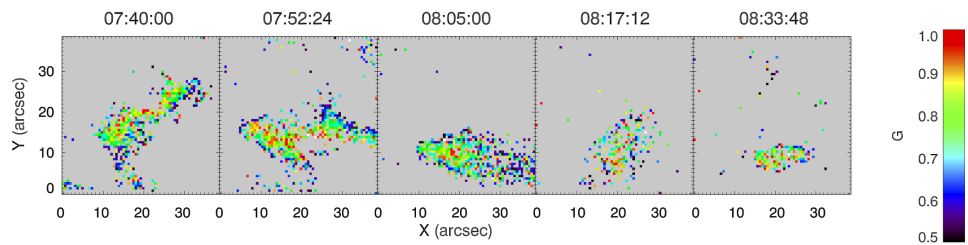


Fig. 3.15: Evolution of the geometric depth G of Target 3, 07:40 – 08:34 UT.

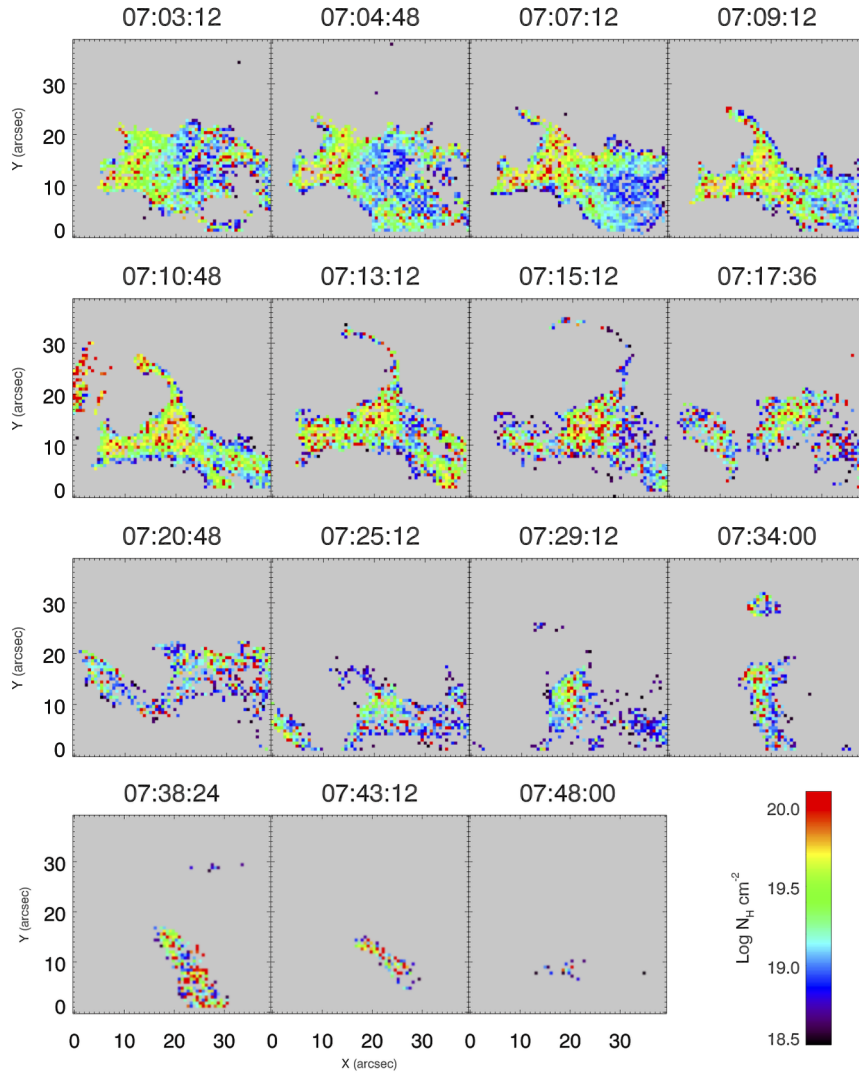


Fig. 3.16: Evolution of the density of Target 4, 07:03 – 07:48 UT. Direction of travel is roughly towards the upper-left corner of the images.

Figure 3.16 shows the calculated column density values for a fourth target blob at fifteen points along its descent. The column density of this blob was examined at higher cadence than the other three as it displayed the clearest instance of the suspected RTi. Mean column density is found to be $4.80 \times 10^{19} \text{ cm}^{-2}$ for the first time step (07:03 UT), which rises slightly (though not linearly) to $1.24 \times 10^{20} \text{ cm}^{-2}$ at 07:44 UT, just before ‘splashing down’. Figure 3.17 shows geometric depth G for this target at four points along its descent.

Figure 3.18 shows the calculated errors for Targets 1a and 4a. This demon-

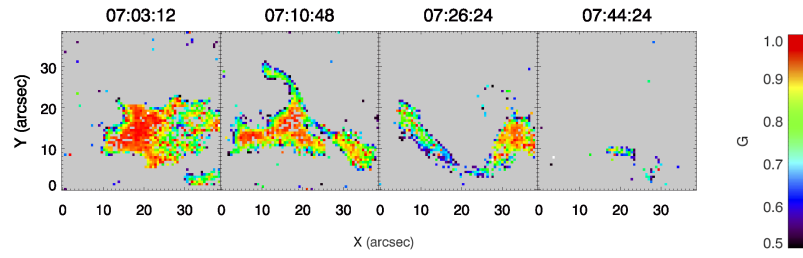


Fig. 3.17: Evolution of the geometric depth G of Target 4, 07:03 – 07:44 UT.

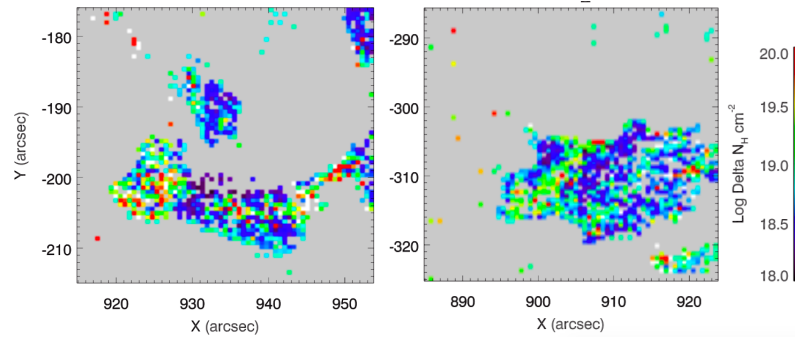


Fig. 3.18: Calculated errors on column density of Target 1a at 07:06 UT (left) and 4a at 07:03 UT (right).

states that the errors are almost of the same order as the results, and are higher in locations where column density seems slightly higher, however, no correlation with geometric depth G is immediately obvious, as larger errors are seen in Target 1a where G is lower, and yet larger errors appear coincident with higher G in Target 4a (by visual inspection and comparison with Figures 3.7, 3.16 and 3.17).

3.4 Rayleigh-Taylor Morphology & Magnetic Field Estimation

As laid out in Section 1.3, the appearance and behaviour of the RTi may be described mathematically; since this Chapter examines a dense fluid being accelerated by a less dense fluid, the conditions for the occurrence of the RTi are right, and the observed forking structures which the blobs are seen to repeatedly form suggest that this material is indeed undergoing an instance of the RTi. Figure 3.19 highlights this by comparing a basic 2D simulation of the RTi with the appearance of a blob as it is seen to split or fork. The

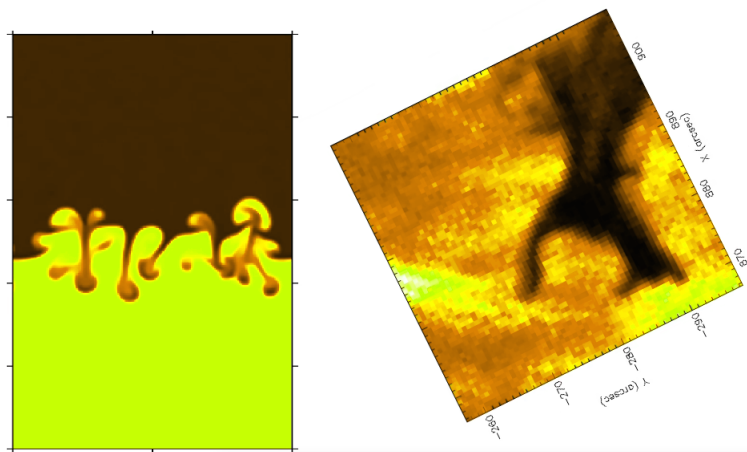


Fig. 3.19: A comparison between a 2D simulation of the RTi and Target 4 as it is seen to fork (rotated so gravity is acting downwards, as in the simulation). The simulation has $A = 9/11$, and was conducted using the (PIP) code, in development by Naoki Nakamura at Kyoto University.

mass distribution and evolution thereof in the column density maps are also consistent with RT-unstable conditions, with a ‘piling up’ of material towards the front of the targets (particularly before the splitting occurs) indicative of the acceleration of the fluid by gravity.

It should be possible to use the equations describing the instability to investigate the strength of any magnetic field embedded in the material. Recalling Equation 1.27,

$$B_x = \sqrt{\frac{g\lambda(\rho_h - \rho_l)}{2 \cos^2 \theta}}, \quad (3.8)$$

the magnetic field strength may be found provided the gravitational acceleration, characteristic wavelength and density difference are known. All values of θ , the angle between the wavevector and magnetic field, may be considered, and the largest corresponds to $\cos^2 \theta = 1$. This will give the lowest value for B_x (where x is taken as the direction in the plane of sky, perpendicular to the direction of motion of the target), and since a lower limit of the column density is calculated, a lower limit on the magnetic field strength is also suitable.

From the STEREO-A image shown in Figure 3.2, the blobs appear to be roughly spherical structures lying at the front of radially-elongated structures. Therefore, to obtain an estimate for volume density, a depth equivalent to the width of each blob was used with the mass of hydrogen $m_H = 1.67 \times 10^{-24}$ g

to give $\rho_{blob} \simeq 6 \times 10^{-14} \text{ g cm}^{-3}$. The density of the corona was taken to be $\rho_{corona} = 1 \times 10^{-15} \text{ g cm}^{-3}$, and the observed spatial separations were all seen to be of the order $\lambda = 15'' = 1.09 \times 10^9 \text{ cm}$. The surface gravity of the Sun is $g_{surf} = 2.74 \times 10^4 \text{ cm s}^{-2}$, however, the targets were studied at a height of approximately $0.5 R_{\odot}$ above the surface, and as such a value of $g = 1.22 \times 10^4 \text{ cm s}^{-2}$ is used. Therefore, from Equation 3.8 one obtains a lower limit on the magnetic field parallel to the blob fronts in the plane of sky of 0.6 G. This is a reasonable value for the quiet corona which the material is seen to fall through, and also for a flux rope which is seen to have expanded so much. Therefore the postulation of the occurrence of the RTi is strengthened.

3.5 Discussion

The calculated values for (the lower limit of) column density of hydrogen in the condensations of in-falling ejecta following the filament eruption on the 7th of June 2011 are all found to have a mean between approximately $4 - 11 \times 10^{19} \text{ cm}^{-2}$, over a factor of two greater than published column density values of pre-eruption filaments: for example Gilbert et al. (2005) found the column density of a pre-eruption filament to be $1.6 \times 10^{19} \text{ cm}^{-2}$. This makes the results seem rather surprising, considering that the blobs studied in this work are formed from a cloud of ejecta which was seen to expand in area (projected onto the plane-of-sky) by roughly two orders of magnitude (by visual inspection of the AIA images), and also considering the small sizes of the blobs which hints that the targets may have an unusually high volume density. However, when considering that filament eruptions are ‘fuelled’ by magnetic energy and opposed by gravity, the material which falls back to the Sun would be expected to have an unusually high gravitational potential energy and therefore a high density.

All of the blobs examined have well-defined leading edges in the direction of travel, though most of them have long, diffuse tails, often connecting all the way back to the original erupted cloud. The front edge was considered to be the most important feature in identifying blob itself, which is why background selection focused on bringing out this feature. The reason for the importance of

the front edge is that this is the interface at which the RTi is most interesting. This is why the calculated column density values for the tail of some targets are omitted, such as explained previously for Figure 3.7.

As noted in Section 3.3, a slight decrease in geometric depth is observed for Target 1, from ~ 0.95 to ~ 0.8 , where equations 3.6 and 3.7 give $G = fI_b/(I_b + I_f)$. Therefore, either the pixel-filling factor f is falling, meaning that fine-structure (*i.e.*, on scales below the resolution of SDO/AIA) is becoming more prominent in the material, or that a greater portion of the received radiation is being emitted from the ‘foreground’ coronal material as the target falls to lower heights in the solar atmosphere. I believe the latter is more likely, as the amount of emission in the foreground will always increase as the height of the target material in the corona decreases for a uniform atmosphere. Furthermore, fine structure forming as the material falls could suggest interaction with strong magnetic fields, but no sudden change in trajectory or velocity is seen to support this – both by visual inspection, and supported by studies of similar material following the same eruption by Gilbert et al. (2013).

However, all observed blobs appear to decrease in size as they fall through the solar atmosphere, and so it is possible that fine structure could be forming in the same way that the edges of the blobs are found to ‘disappear’. This reduction in observed size could be due to more of the material becoming fully ionised by the radiation from the surrounding corona (or by some other heating process), or due to the blob itself breaking apart and becoming more diffuse from frictional interaction with the surrounding corona.

Mean column density is actually seen to increase for all blobs, though only by a factor of up to roughly 2; this may be due to portions of material with lower column density becoming ‘transparent’ more easily, due to radiation penetrating the material easier and therefore allowing for faster ionisation, and is not interpreted as the blobs themselves becoming more compact. It can be seen from Figure 3.10 that the overall number of target pixels falls and there is less of an obvious peak in the distribution. However, the median mass of this target, $1.82 \times 10^{19} \text{ cm}^{-2}$, is roughly constant along the descent. For Target 2, the median column density rises slightly from $2.40 \times 10^{19} \text{ cm}^{-2}$

to $2.91 \times 10^{19} \text{ cm}^{-2}$; for Target 3 this falls from $8.31 \times 10^{18} \text{ cm}^{-2}$ to $6.92 \times 10^{18} \text{ cm}^{-2}$; and for Target 4 this rises from $1.77 \times 10^{19} \text{ cm}^{-2}$ to $3.21 \times 10^{19} \text{ cm}^{-2}$.

As mentioned in Section 3.3, the effects of emissivity blocking are ignored, but another assumption made is that the target material itself is not in emission. Emission is a function of temperature and, therefore, also wavelength; this means that were the material in emission, different drops in intensity would be seen in different bandpasses, resulting in a poor fit of the data to the model. The values of χ^2 for all pixels analysed were within a reasonable tolerance – no more than an order of magnitude deviation from unity (*i.e.*, a perfect fit) – so the data seem to fit the model sufficiently well such that neither emissivity blocking nor target emission need to be taken into account.

Not only are the morphology and dynamics of the blobs self-similar, but they are indicative of the RTi. The calculated densities and length scales over which the RTi-like morphology is seen to occur give an order-of-magnitude estimate of the characteristic magnetic field strength embedded in the plasma which is comparable with previously published coronal values, 0.6 G: Cho et al. (2007) find values of 0.4 – 1.3 G at heights of 1.6 – 2.1 R_{\odot} .

There are some uncertainties with the magnetic field strength calculation, in that the RTi is a complex, 3-dimensional process, while this work predominantly relies on a 2-dimensional projection. Whilst the STEREO-A measurements allow us to make informed estimates of the true geometry of the observed material, these data are not high resolution or cadence enough to accurately measure the volume of these small, dynamic blobs. As stated in Section 3.4, the calculations use $\cos \theta = 1$, *i.e.*, the angle between the wave-vector and the direction of the magnetic field $\theta = 0^\circ$. This will therefore give a lower limit for B , which is also the case since as the density estimate used to calculate this is a lower limit (see Equation 3.8). This is in fact the magnitude of the component of the magnetic field aligned with the observed wave-vector, whose plane-of-sky component is observed.

The calculations used to derive Equation 3.8 (in Section 1.3) describe the linear phase of the RTi. However, it is possible, if the RTi is indeed occurring

in the studied material, that the instability is well into the nonlinear phase by the time the forking dynamics are seen. The point at which the instability moves from the linear to nonlinear phase is difficult to define for an observed system, especially a system which is not as easily described as two regimes of uniform magnetic fluid. However, the eigenfunction of the vertical velocity is $V_z(z) = Ae^{-k|z|}$ (Chandrasekhar 1961), which implies that a perturbation can travel $1/k$ before reaching nonlinear saturation. This is of the order of λ_u , and the separation measured in the observations satisfies this.

3.6 Conclusions

The 7th of June 2011 eruption cast an unusually large amount of filament material into the solar atmosphere, with a large portion of the ejecta falling back to the Sun in discrete condensations. The total hydrogen column density of these back-falling blobs has been found to have a mean lower limit of approximately $4 \times 10^{19} \text{ cm}^{-2}$ - a value higher than column densities previously found in *pre-eruption* filaments.

The front of the falling material which formed the blobs studied was found to exhibit morphological evidence for the occurrence of the RTi. The shapes formed by the plasma as it falls through the solar atmosphere are extremely similar in appearance to simulations of the RTi, and the dynamics of the distribution of density within the blobs supports this further.

Using observations of this material collected by STEREO-A, which at the time observed the Sun from $\sim 95^\circ$ ahead of the Earth in its heliocentric orbit at the time, the blobs were seen to have depths of the same order as their height and width. Therefore, assuming roughly spherical geometry, and using calculated column density values and measured fork separations, a characteristic magnetic field strength was found from RTi equations to have a lower limit of the order ~ 0.6 G. This is comparable with previously published values for coronal magnetic field, and so the observed behaviour of the material is compatible with the RTi.

Chapter 4

Observations and Simulations of The Rayleigh-Taylor Instability in Erupted Material

I would like to thank Andrew Hillier, Davina Innes and LiJia Guo for their help with the simulations conducted in this project, and insight into the interpretation of the results.

The material studied in Chapter 3 is only a small part of the ejected material from the 7th of June 2011 eruption; the observed occurrence of the Rayleigh-Taylor instability (RTi) in that work prompted me to examine more of the erupted filament material in the context of the RTi.

Just before the point at which smaller condensations are observed to ‘break away’ from the bulk of the CME, the material which ultimately returns to the Sun reaches zero (radial) velocity, and large (diameter of the order 10^4 km) bubbles can be seen developing into the ejected material (radially away from the solar surface). As these bubbles grow, secondary ‘fingers’ can be seen forming within the bubbles, and the material has been confirmed as RT-unstable by Innes et al. (2012). The growth rates of these bubbles are measured and compared, taking different inclinations to the solar surface normal. This may provide insight into speculated outflows from beneath the ejecta.

The development of such bubbles has only been extensively studied for the hydrodynamic regime, but the material in the solar corona is highly ionised

with embedded magnetic fields. Therefore, I decided to undertake numerical Magnetohydrodynamic (MHD) experiments by conducting simulations of RT-unstable plasma with varying magnetic field strength. The simulations are initially set up as a three dimensional volume with the origin in the centre; material of density $\rho_l = 1$ is placed at all $z < 0$ and $\rho_h = 10$ at all $z \geq 0$, with a gravitational acceleration in the negative z direction. The interface is then given a random z -velocity perturbation (peaking at 1% of the sound speed) and the system is allowed to evolve according to the equations of ideal MHD (see Sections 1.1.3 and 4.2.1). This should create instances of the RTi which can be investigated and potentially compared with observations. I use the freely available Athena code to run these simulations. Whilst previous work has examined the effect of a magnetic field on the RTi such as Stone and Gardiner (2007b), no studies have examined the growth rate in relation to these magnetic field strengths (or rather this range of magnetic energy relative to gravitational potential, as parameters in a simulation are dimensionless and only have relevance in relation to one another).

4.1 Measured Rayleigh-Taylor Growth in Erupted Filament Plasma

4.1.1 Observations

The observational part of this project analyses images gathered on the 7th of June 2011 between 06:48 – 07:11 UT by SDO/AIA (see Section 2.1). The pass-band chosen is the 193 Å channel, as the target material appears with stronger contrast relative to the other EUV filters. The material studied appears off the south-west limb almost immediately after the initial eruption occurs, as with the material studied in Section 1, however, the target(s) in this project are distinct from those studied earlier. This target material is chosen for the clear bubble-development seen at the point at which the initial bulk of low-lying erupted material appears to reach zero velocity, and is only studied while off-limb, whereas previously smaller condensations of similar material already falling towards the solar surface were studied in front of the disc.

4.1.2 Rayleigh-Taylor Growth Analysis

Rather than examining the length-scales associated with the linear phase of the instability as done previously in Section 3.4, here I am interested in continuing the work of Innes et al. (2012) by examining the nonlinear growth of the bubbles over time. I want to measure the relationship between the ‘height’ (that is, the distance from the initial interface between the two plasmas) of the front of observed bubbles and time, predicted to have a square dependency by the growth of self-similar bubbles (see Section 1.3).

In order to measure the development of the bubble front position relative to the initial interface, vectors in space must first be defined which are normal to the centre of the front of the bubble at all points in time which the measurement is required for. Another way of putting this is that the vectors should be straight lines which are always bisecting the same bubble. These vectors are shown in Figure 4.1, which highlights four slices of varying inclination for the solar surface normal passing through three distinct bubbles (slices 1 and 2 pass through the same bubble at different points). The different inclinations are used in order to assess whether there was any particular directionality in the plane-of-sky to possible ‘windy outflows’ which may be enhancing the RTi, that is fast-moving, transparent material being accelerated away from the Sun, impacting the dark material which forms the target of this study.

The points in space over a slice are then taken as a vector of values, and an array is built up by taking this vector of values for each time-step, generating a time-slice plot. This makes it much easier to examine any acceleration of material moving along such a slice. Further to this, running difference movies are made from the 193 Å channel: this is achieved by subtracting the previous image from the current, leaving a positive value if the intensity has increased with time (at the given location) and vice versa. The merit in doing this is that the most positive points correspond to locations which absorbing material has moved away from, the most negative to locations which absorbing material has moved into, and any pixels for which the intensity does not change (or changes very little) have values close to zero. This means a visual representation of such data will most clearly show the most dynamic material.

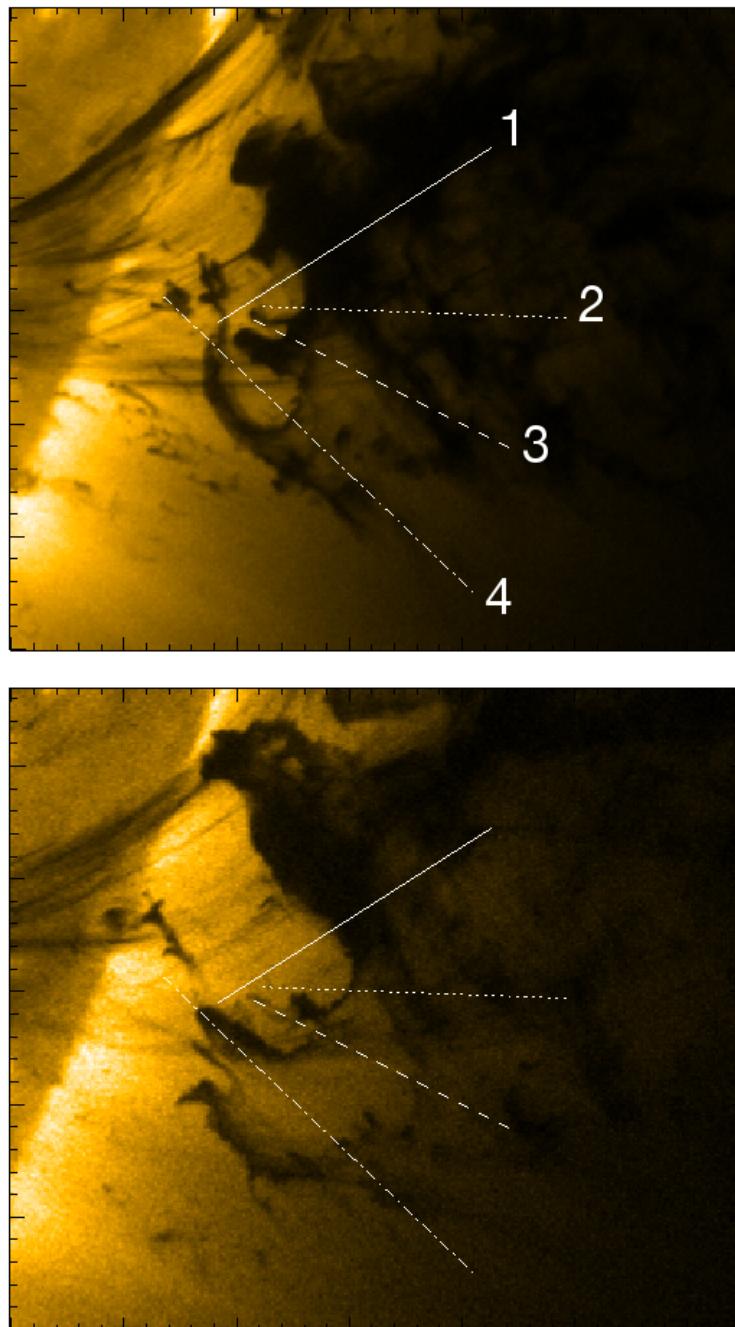


Fig. 4.1: A snapshot of the material at 06:54 (top) and 07:01 UT (bottom) on the 7th of June 2011 in 171 Å, SDO/AIA. The material in the upper left of the frame goes on to become Target 1 in Chapter 3. The white lines are slices along which the displacement of the material was measured.

The four plots shown in Figure 4.2 are generated by building time-slice plots from the running difference movie: the distance along each slice is given on the y axis (where I have taken the movement of the bubbles along the slices in Figure 4.1, *i.e.*, left-to-right, as being positive distance) and time is given on the x-axis. Therefore, by tracing the brightest white curves in Figure 4.2 (which correspond to the sudden increase in intensity at the leading edge of the blob, created by the absorbing material having just moved out of this location), and the measured position with time of bubble fronts are plotted over the time-slice plots in red.

The curves give the distance over which bubbles develop as a function of time (in kilometres and seconds, respectively) and using these, plots can be made of equation 1.28, $h = \alpha A g t^2$, shown in Figure 4.3. The predicted dependence of height on time squared indicates that these plots should be straight lines, where the gradient is given by α , plus any additional acceleration terms, such as the force exerted on the higher-density material by the presence of any outflow. In Figure 4.3 the plots have been scaled by Atwood number, taken as $A = 99/101$, and gravitational acceleration, with inclination of the slice to the normal of the solar surface taken into account by using $g_i = g_s \cos(\theta)$, where θ is inclination to the normal and gravitational acceleration at the solar surface $g_s = 0.274 \text{ km s}^{-2}$.

The first two slices pass through the same bubble (from the top of Figure 4.1; the solid and dotted lines), though with different inclination, and from Figure 4.3 appear to share a very similar evolution. The third slice (dashed line) has a slower initial phase, though this has a sudden increase which can be seen when watching a movie of the event; a small bubble is seen to slowly grow to a diameter of approximately $2 \times 10^3 \text{ km}$, when it suddenly undergoes rapid acceleration, blowing out into a bubble of diameter approximately one order of magnitude larger in only 10 minutes before colliding with other material. The fourth slice (dot-dash line) has the fastest growth, and where this is seen to fall towards the later times is in fact either a collision with material in front of the bubble, or slower moving material suddenly becoming visible above/below the bubble.

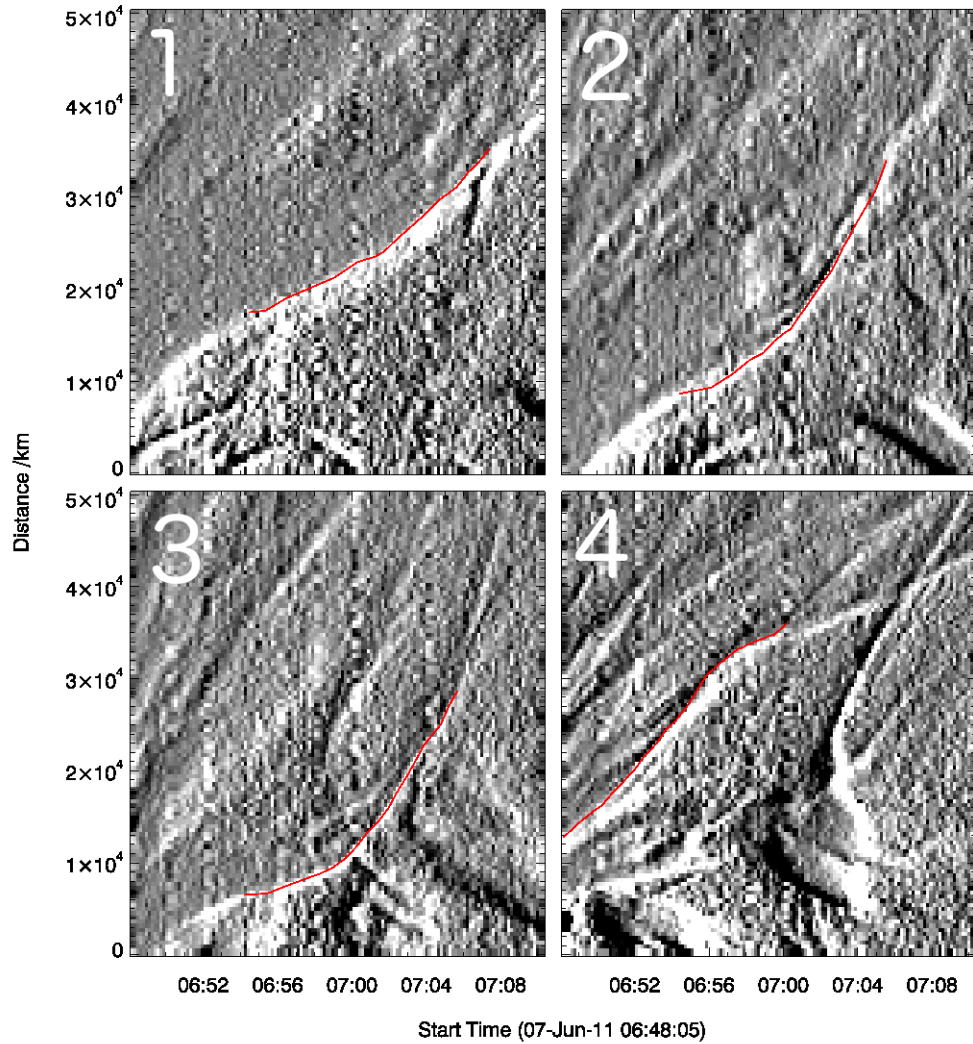


Fig. 4.2: Plots which highlight the change in position of bubble front as a function of time. Each time slice plot presented here corresponds to a slice in Figure 4.1, and is shown as a running difference: bright white curves indicate locations which absorbing material has just moved away from, which will correspond to the front of the bubble. The overlotted red lines are human-input lines following the strong white curves. Note the numeric labels in the top left of each plot correspond to those in Figure 4.1 from top to bottom.

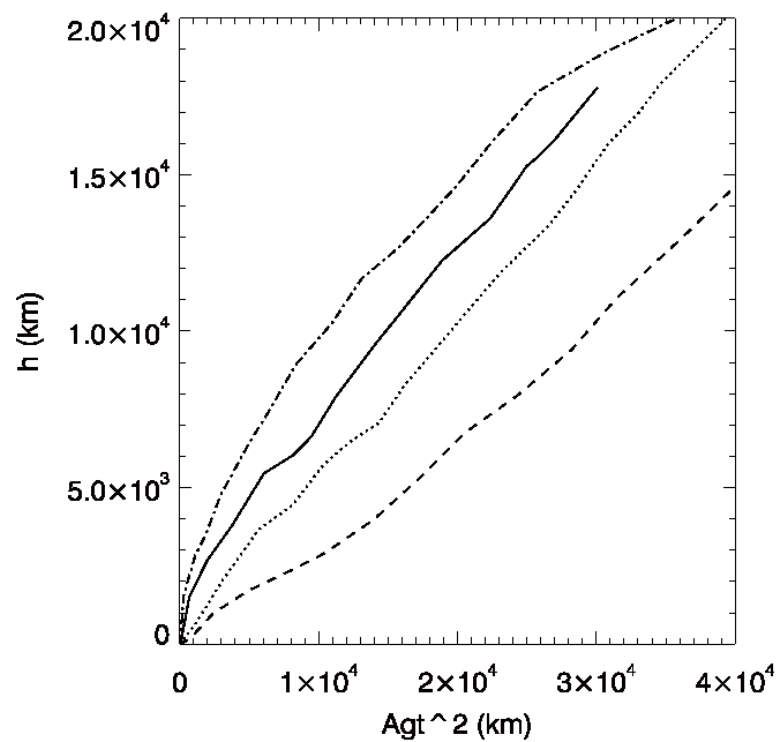


Fig. 4.3: A plot showing the dependence of bubble height on time squared, where Atwood number and gravitational acceleration are taken as constants. The slopes of these lines should be described by equation 1.28 and as such the gradient should be α , plus any additional acceleration. Linestyles correspond to those used in Figure 4.1, that is solid is bubble 1, dotted is bubble 2, dashed is bubble 3, and dash-dot is bubble 4.

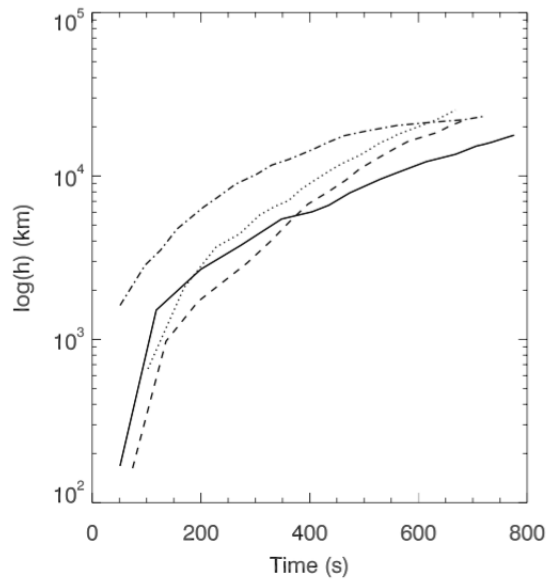


Fig. 4.4: A plot showing the bubble height in logarithmic space against time. This shows only a small amount of exponential growth in the early stages, characteristic of the linear phase of the RTi. Linestyles correspond to those used in Figure 4.1, that is solid is bubble 1, dotted is bubble 2, dashed is bubble 3, and dash-dot is bubble 4.

The onset of the RTi is described to have a linear phase with exponential growth (Chandrasekhar 1961) which is barely seen in the observations, shown best by examining the logarithmic height with respect to time, presented in Figure 4.4. This shows short-lived exponential growth which appears to be quickly damped. This indicates that the observed RTi is fundamentally dominated by the nonlinear regime.

All the slopes are relatively similar and constant in gradient, implying a constant velocity from the postulated ‘windy outflows’ from the solar surface, impacting the material. It is safe to assume that given the temporal and spatial co-location of these measurements that the value for α in equation 1.28 is approximately constant over the slices, recalling

$$h = \alpha A g t^2 \quad (4.1)$$

This was found to be of the order 0.5, however, this has been shown in countless observational studies and theoretical models (*e.g.*, Sharp (1984); Jun et al. (1995); Dimonte et al. (2004); Stone and Gardiner (2007b), *etc.*) to be approximately one order of magnitude smaller. This additional acceleration is

probably due to transparent outflows from below.

4.2 Numerical Simulations of Rayleigh-Taylor Unstable Plasma

4.2.1 Ideal MHD Simulations

This work used the Athena code for astrophysical MHD (see Stone et al. (2008) for a complete description of this code), which solves the equations of ideal MHD with a constant gravitational acceleration, $\mathbf{g} = (0, 0, -g)$:

$$\frac{\partial \rho}{\partial t} + \nabla \cdot (\rho \mathbf{v}) = 0 \quad (4.2)$$

$$\frac{\partial \rho \mathbf{v}}{\partial t} + \nabla \cdot (\rho \mathbf{v} \mathbf{v} - \mathbf{B} \mathbf{B}) + \nabla P = \rho \mathbf{g} \quad (4.3)$$

$$\frac{\partial \mathbf{B}}{\partial t} + \nabla \times (\mathbf{v} \times \mathbf{B}) = 0 \quad (4.4)$$

$$\frac{\partial E}{\partial t} + \nabla \cdot [(E + P) \mathbf{v} - \mathbf{B}(\mathbf{B} \cdot \mathbf{v})] = \rho \mathbf{v} \cdot \mathbf{g}. \quad (4.5)$$

where total pressure $P \equiv P_g + (\mathbf{B} \cdot \mathbf{B})/2$, gas pressure $P_g = (\gamma - 1)\epsilon$, total energy density $E \equiv \epsilon + \rho(\mathbf{v} \cdot \mathbf{v}/2 + (\mathbf{B} \cdot \mathbf{B})/2)$, internal energy ϵ , and the adiabatic index $\gamma = 5/3$ is used. This is not the value which would necessarily be expected from chromospheric or coronal material, however, the simulations are conducted at the incompressible limit by using a large enough sound speed such that all fluid motions are highly subsonic, and so varying the adiabatic index has little effect on the results (Stone and Gardiner 2007b). Note that these equations have been normalised to dimensionless units such that sound speed $c_s = 1$ for $B = 1$ and $\rho = \rho_l = 1$, and the characteristic length scale of the system $\Lambda = 1$. In this model, $g = 0.1$ and so $\sqrt{g\Lambda}/c_s \ll 1$, which indicates that the induced flows are almost incompressible.

The equations are solved using a second-order Godunov scheme, as the sharp discontinuity at the interface between the two fluids is not well dealt with by higher-order solvers. Perhaps the most important element of this scheme is the Riemann solver, which calculates time-averaged fluxes of all conserved quantities at cell interfaces. Here an approximate Riemann solver called Harten-Lax-van Leer-Discontinuities (HLLD) is used as it is found to be as accurate as the well studied Roe approximate Riemann solver and less

computationally demanding (Miyoshi and Kusano 2005). This is combined with the constrained transport (CT) technique which evolves the induction equation in a way which ensures zero divergence of the poloidal (constrained) field components to within machine round-off error (Evans and Hawley 1988). Discretization is based on cell-centered volume averages for mass, momentum, and energy, and face-centered area averages for the magnetic field. Athena has been shown to be successful at conducting MHD simulations of the RTi in three dimensions (Stone and Gardiner 2007a) into the nonlinear regime (Stone and Gardiner 2007b) , and as such it was deemed suitable for conducting the investigation presented in this Chapter.

The x and y boundaries of the domain are periodic whilst the z boundaries are reflective, and the origin is in the centre of the domain. The regular cartesian grid used has dimensions of $256 \times 64 \times 1024$. Resolution in the z-dimension (corresponding to height) was doubled relative to x and y so as to achieve a high precision and accuracy of measurement of height and therefore growth rate.

The system is initially in hydrostatic equilibrium, and the gas pressure is chosen such that the sound speed (c_s) in the light fluid at the interface is unity, and so

$$P(z) = \frac{3}{5} - g\rho z + \frac{B^2}{2}. \quad (4.6)$$

A characteristic length scale of the system Λ maybe be described as being roughly an order of magnitude larger than the scales predicted by equation 1.26, $\lambda_{ux} = \frac{2\cos^2\theta B_x^2}{g(\rho_u - \rho_l)}$. The width of the domain in the direction of magnetic field used for the first set of simulations is set to be $L_x = 0.4\Lambda$. This width is chosen to allow $L_x \geq \lambda_u$ for the magnetic field strengths used across all simulations, and resolves the dominant wavelengths λ_u with at 44 grid points for the weakest field (and therefore with greater resolution for the stronger fields).

RTi modes perpendicular to the magnetic field behave as the hydrodynamic case, and so the smallest scales are favoured. Numerical diffusion in the simulations was of the order 0.01Λ for the resolution used, so $L_y = 0.1\Lambda$ is used as the depth of the domain, allowing sufficient space for interchange

structures to develop. A height of $L_z = 0.8\lambda$ is used to ensure sufficient room for the instability to develop (*i.e.*, up to scales where the bubble height is equal to the width, recalling that bubbles wider than L_x are unlikely to develop in early stages of the nonlinear limit), without the growth of the bubbles being affected by the reflective upper boundary.

The outwards motion of CMEs is thought to be primarily due to magnetic forces, and the fall-back of the material is due to gravity. Therefore it is useful to define some parameter relating the two in order to choose the magnetic field strength of the simulations such that they may be compared with the observed case. This parameter was chosen as

$$J = \frac{c_A^2}{gL} \quad (4.7)$$

where c_A is the Alfvén velocity. J is therefore a dimensionless parameter which describes the balance between magnetic and gravitational forces. A system with $J \gg 1$ is likely to be dominated by the magnetic forces, and one with $J \ll 1$ is likely to be dominated by the gravitational forces.

The lowest J (the weakest magnetic field strength) corresponds to the Athena RTi test case (and as such has been rigorously analysed and tested for accuracy), however, higher J simulations have not previously been conducted; the highest J (strongest field) used here is at the limit of $L_x \simeq \lambda_u$. A larger L_x was not used as the simulations were already computationally demanding; a lower resolution was also avoided as the current setup should lead to approximately 50 pixels per λ_u , and lower resolution is not desirable as it is important that the simulation allows all scales dictated by the physics to develop, and not be inhibited for computational reasons. The magnetic field is initially applied uniformly along the x axis, that is ($B_x = \text{const.}$, $B_y = 0$, $B_z = 0$). Seven simulations were run in this set, and are described in Table 4.1.

The mixing layer (that is all fluid with $1.5 \leq \rho \leq 9.5$, where the initial setup has $\rho_l = 1$ for $z < 0$ and $\rho_h = 10$ for $z \geq 0$) of B1, B3, B5 and B7 are shown at three points along the run in Figure 4.5. The chosen start time of 0.1 rather than 0 is to show the interface; at $t = 0$, the lower half of

Label	J	L_x/λ_u	α
B1	0.0625	5.7	0.0470
B2	0.09	4.0	0.0380
B3	0.1225	2.9	0.0375
B4	0.16	2.2	0.0394
B5	0.2025	1.8	0.0395
B6	0.25	1.4	0.0366
B7	0.3025	1.2	0.0371
B8	0.36	1.0	0.0354

Table 4.1: Initial conditions of varied parameters and measured nonlinear growth rate over first set of simulations.

the domain is filled with $\rho_l = 1$ material and the upper half with $\rho_u = 10$, so no mixing layer is visible. As the simulations progress, bubbles of scales predicted by equation 1.26 can be seen developing along x , the direction along which B is directed. The scales of these so-called undular modes are seen to increase as J (and hence magnetic field strength) increases, whilst the scales across the magnetic field, the interchange mode, remain apparently constant for all simulations: one interchange bubble is seen.

Since the only two parameters which vary between B1 – B7 are J and L_x/λ_u (the ratio of domain width to dominant linear wavelength of the RTi), I wanted to ensure the observed change in growth rate was due to the former rather than the latter. In order to do this, a second set of simulations was run, where magnetic field was kept constant but the width of the domain was made progressively smaller. If a dependence of α on L_x/λ_u were to be seen in simulations of constant magnetic field similar to this dependence in the previous set of simulations, then the magnetic field could not be said to be causing the postulated effect on growth rate. Four simulations were run with $J = 0.0625$ and other parameters detailed in Table 4.2. Figure 4.6 shows the final state of the mixing region for W2, 3 and 4. Note that W1 has the same initial conditions as B1, highlighted by comparison with Figure 4.5.

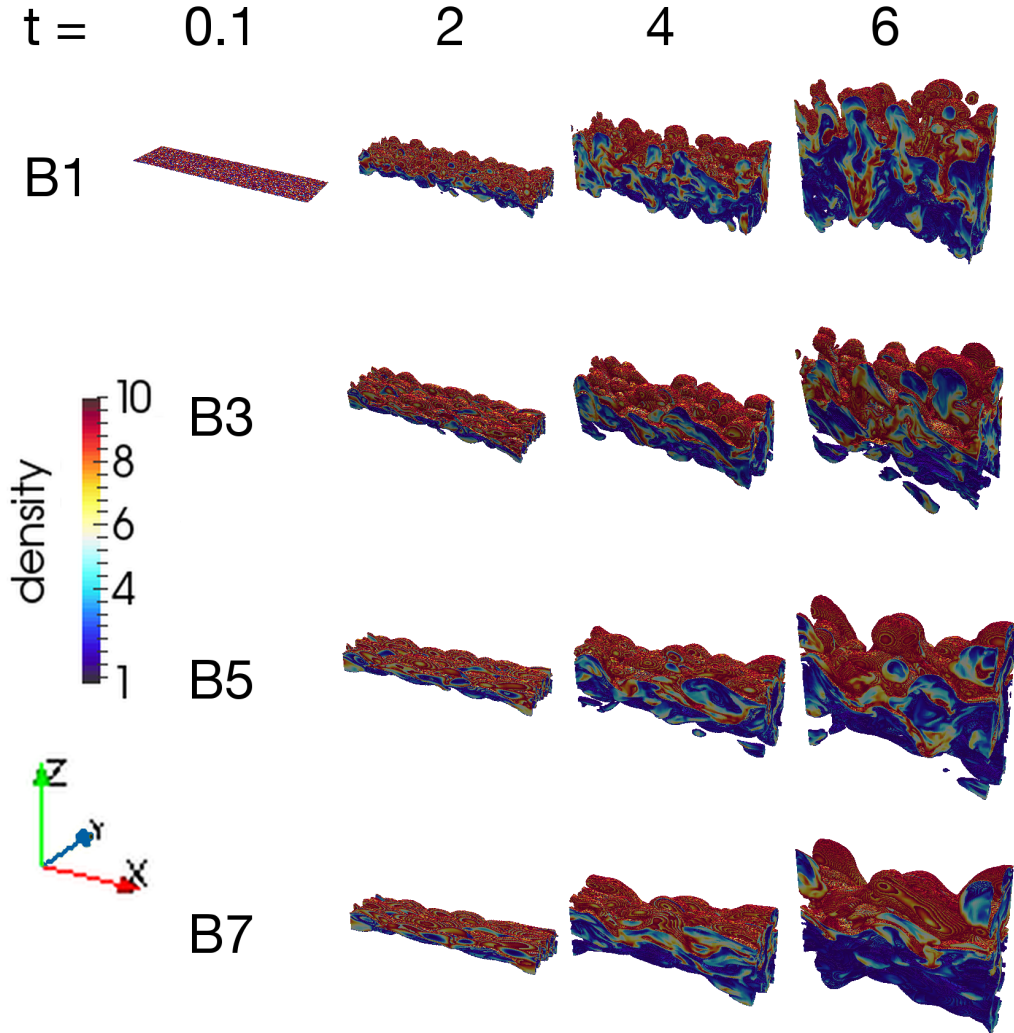


Fig. 4.5: Images showing the mixing region $1.5 \leq \rho \leq 9.5$ of simulation B1, B3, B5 and B7 (c.f. Table 4.1) at $t = 0.1, t = 2, t = 4$ and $t = 6$ (Note: the interface visible at $t = 0.1$ appears very similar for all runs and as such is only included once). The volumes are bound by surfaces of $\rho = 1.5$ and $\rho = 9.5$. The faces of the domain, *i.e.* the edge of the volume show a slice of all material with density between 1.5 and 9.5. The magnetic field is initially applied along the x axis (the horizontal axis along the page in these images). From this figure, the morphological development of the RTi can be seen, with both bubble height and finger depth increasing rightwards in the Figure.

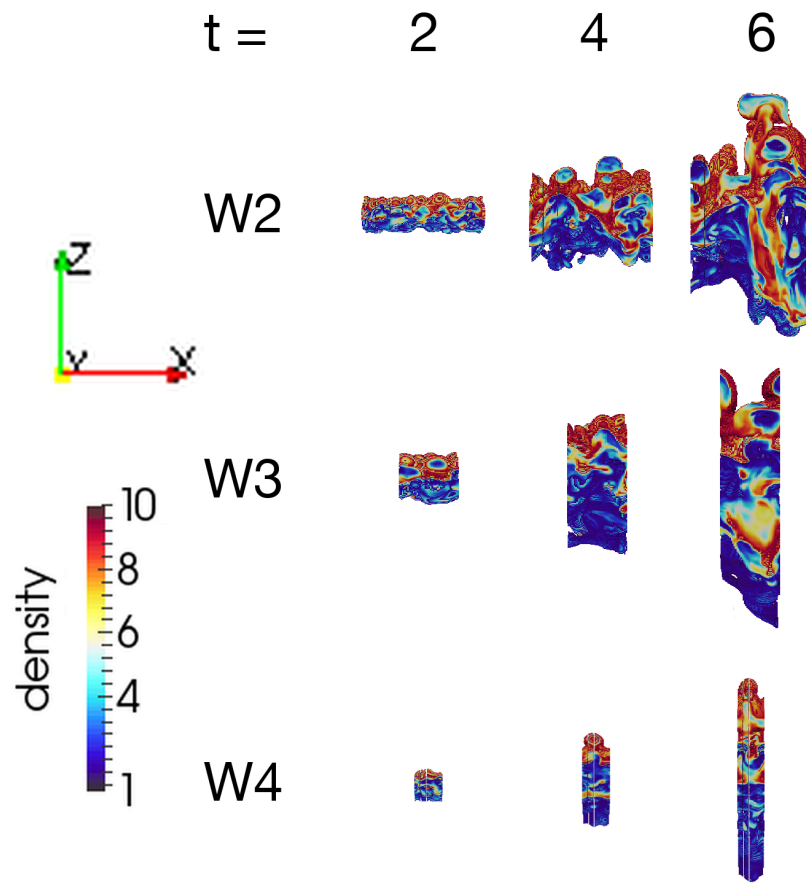


Fig. 4.6: Images showing the mixing region $1.5 \leq \rho \leq 9.5$ of simulations W2, W3 and W4 (c.f. Table 4.2) at $t = 2, 4, 6$.

Label	L_x	L_x/λ_u	α
W1	0.4	5.7	0.0470
W2	0.2	2.9	0.0634
W3	0.1	1.4	0.0338
W4	0.05	0.7	0.0399

Table 4.2: Initial conditions of varied parameters and measured nonlinear growth rate over second set of simulations.

4.2.2 The Effect of Magnetic Field Strength on the Nonlinear Development of the Rayleigh-Taylor Instability

The measure of bubble height h was taken as being the highest point in z at which the average density of the x - y plane is $\rho_{xy} \leq 9.5$, which should return a position at the average height of all bubbles; Figures 4.5 and 4.6 show the sharp density gradients at the edges of the mixing region. Figure 4.7 shows plots of equation 1.28 for each simulation in the magnetic field varying set. The gradient of the slopes defines the relative rate at which bubbles grow, and it is apparent that this decreases across the simulations from B1 to B7 from visual inspection, suggesting that increased magnetic field strength will yield a reduced (nonlinear) growth rate (as well as agreeing with the analytic prediction that linear growth rate decreases with magnetic field strength; see equation 1.23). This is an interesting result, as Stone and Gardiner (2007b) showed that the addition of a strong magnetic field caused an increase in nonlinear growth rate at later times of the RTi compared to the hydrodynamic case. This is due to the frozen-in flux condition preventing material from moving across field lines and as such inhibits mixing at the interface.

The early linear phase of the RTi can be seen in Figure 4.7, characterised by an exponential growth (see Section 1.3 for an explanation of this). The rate of growth appears to then suddenly decrease at the same point in all B simulations, continuing thereon with a relatively steady dependence on t^2 . Some lines diverge from this steady t^2 dependence towards later times, as the more time the system evolves over, the more important turbulence becomes, making the system increasingly difficult to predict the behaviour of. Nonlinear growth rate α is estimated from the gradients of the slopes for what appears to be the early nonlinear phase (taken as $0.5 \leq Agt^2 \leq 2$, chosen from visual inspection of Figure 4.7; corresponding to $2.47 \leq t \leq 4.94$) and is found to generally decrease from ~ 0.047 to ~ 0.035 as magnetic field strength is increased; calculated values of α are listed in full in Table 4.1.

Similar plots of the W simulations are shown in Figure 4.8, which also appear to show a change in α across the simulations, listed in Table 4.2, where L_x/λ_u is the only parameter which is decreasing between simulations.

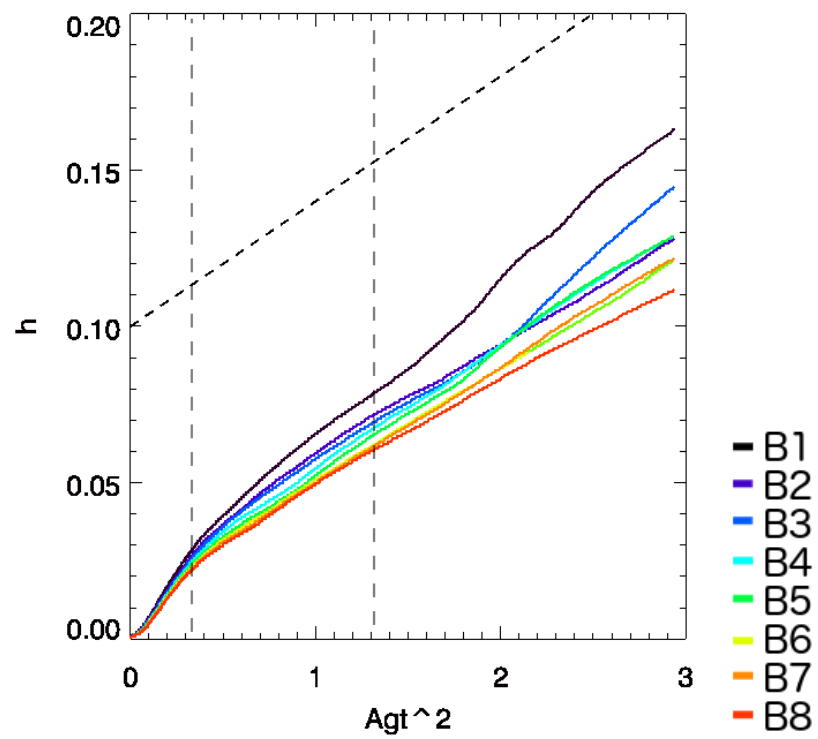


Fig. 4.7: Plots showing the development of bubble height as a function of Agt^2 for the B simulations. Grey dashed lines mark $t = 2$ and $t = 4$; simulations end at $t = 6$; black dashed line represents a slope with $\alpha = 0.04$ for visual comparison.

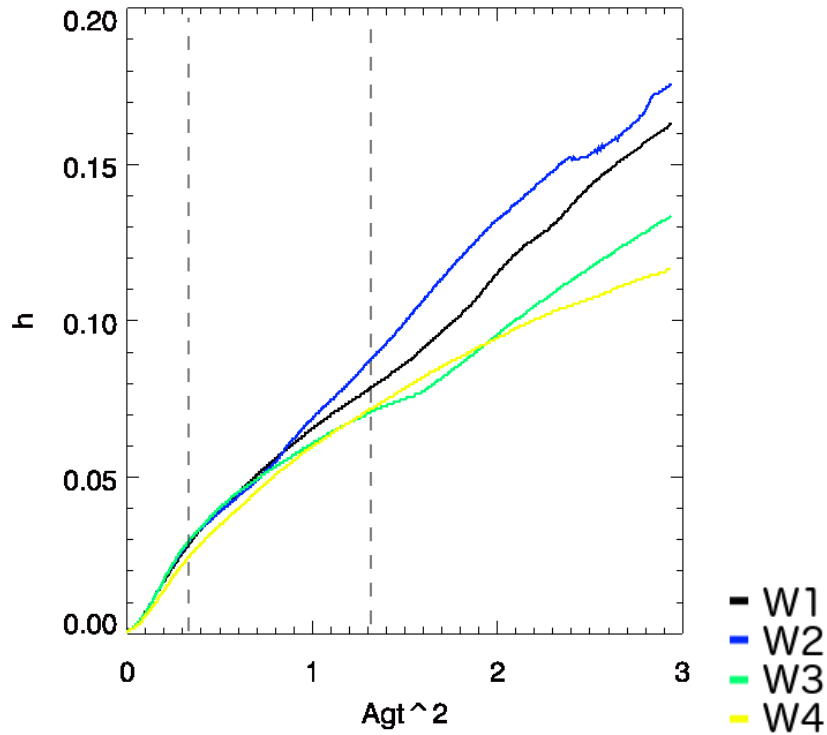


Fig. 4.8: Plots showing the development of bubble height as a function of Agt^2 for the W simulations. Dashed lines mark $t = 2$ and $t = 4$; simulations end at $t = 6$.

This suggests that magnetic field is not necessarily having a strong effect on the nonlinear growth of the RTi, though the trend in α is much clearer and correlative in set B.

A value of α was also found for the W simulations over the early nonlinear phase ($0.5 \leq Agt^2 \leq 2$); these values are listed in Table 4.2. This large spread does not show such a strong correlation as the values found for set B, therefore I can say with reasonable confidence that the nonlinear growth rate of the RTi is reduced as magnetic field strength increases. This effect is even more pronounced when comparing Figures 4.7 and 4.8 at early nonlinear times; The plots in Figure 4.7 appear to suddenly spread out uniformly at approximately $Agt^2 \approx 0.4$, whereas the plots in Figure 4.8 do not appear to diverge particularly until somewhat later times ($Agt^2 \approx 0.9$), and this divergence does not appear to follow any correlation, as in set B.

4.3 Comparison of Observations and Simulations

A value of $J = 0.8$ was calculated for the observed material using the Alfvén speed of 47 km s^{-1} found by Innes et al. (2012), a gravity of half the solar surface gravity (since the material is assumed to be approximately $0.5 R_{\odot}$ above the surface) $g = 0.137 \text{ km s}^{-1}$, and a characteristic bubble size of $2 \times 10^4 \text{ km}$. This J is a factor two greater than that of the simulation with the largest J , and as such direct comparison is not ideal; however, the simulations have been conducted over a greater range of parameter space in J and not only is a small variation in nonlinear growth rate seen, but the growth rates are seen to converge as larger values of J are reached.

In order to compare the growth rates of the height of developing bubbles relative to the initial interface between observations and simulations, it is useful to normalise the data by some scaling factor of the system. In the simulations, this was chosen as the width of the domain along the magnetic field, L_x ($= 0.4$ for B simulations), and for the observations it was taken as twice the largest size the bubbles were seen to reach, $L_x = 5 \times 10^4 \text{ km}$. This allowed the simulated data to be plotted alongside the observations, shown in Figure 4.9. The red line represents B1, while the black lines have the corresponding style from Figures 4.1 & 4.3. These observational plots have been modified to best fit the slope of the simulations by multiplying Ag by an additional factor due to the ‘windy outflows’, $w = 10$.

Since both L_x/λ_u and J affect α , only the simulation with the largest L_x/λ_u is plotted with the observations, as these are not constrained by any width. In the observations, secondary instances of the RTi are seen beginning to form within the original bubbles, suggesting that much later times in the instability are being reached than in the simulations, and nonlinear growth rate may become affected by successively larger scales dominating. Previous studies have also shown there to be a discrepancy between the values of α determined from simulations (faster developing) and laboratory experiments (slower) by up to a factor 2 (Dimonte et al. 2004). This would reduce the estimation of the wind factor to be $w = \sim 5$.

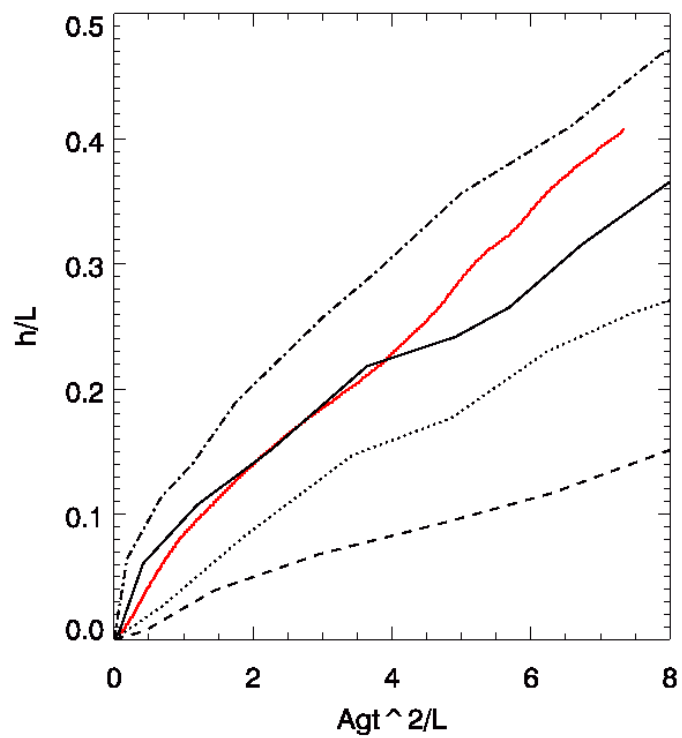


Fig. 4.9: Comparison plots of the development of the observed bubbles (black lines) and simulation B1 (red line). Note that these curves have been normalised by a characteristic length scale of the system, and an additional acceleration term has been included to the solar g value (adapted to observed height and inclination) to fit the observed curves to the simulation as best as possible.

4.4 Discussion

The observational results presented in this Chapter demonstrate a consistent growth rate amongst bubbles in ejected material following the the 7th of June 2011 filament eruption. This suggests that the density, magnetic field strength and motion of the material is reasonably consistent throughout the examined ejecta. The growth of the bubbles is much faster than predicted from previous studies of the nonlinear growth of the RTi, both numerical simulations and laboratory experiments.

Measuring the growth rate of the bubbles is complicated by the motion of the higher-density material itself; whilst the analysis is conducted at the point at which the bulk of the material appears to be static, it is not certain that the material in fact has reached zero velocity. Not only do projection effects become a problem (*i.e.*, the material is only viewed from one angle and as such motion along the LOS is almost impossible to notice), but it is also difficult to define a frame of reference for a fluid which is moving in such complex ways; distinct velocities (magnitude and direction) are seen in material which appear to be a part of the same ‘cloud’. The bulk of the material does indeed appear to be relatively stationary at the start of the analysis, however, some other parts of the ejecta still appear very dynamic at this point.

Another potential problem is g : the value used is half the surface acceleration since the material is clearly seen to be at least $0.5 R_{\odot}$ above the surface (where gravitational acceleration obeys an inverse square relation to distance). However, the true value could be higher than this due to projection effects causing an underestimate of the height of the material.

The simulations conducted examine the impact of magnetic field strength on the development on the RTi. The results indicate that increased magnetic field strength leads to reduced nonlinear growth rate. This could be due to an increased magnetic tension ($= (\mathbf{B} \cdot \nabla)\mathbf{B}/\mu_0$) in stronger magnetic field, which requires greater energy to overcome and therefore reducing the momentum of the plasma. Values of alpha for the simulations presented here are somewhat lower than many previously published values, though this is not necessarily due to the magnetic field strength, as algorithmic differences and differences in

simulation duration have an effect on numerical dissipation and as such may affect the growth rates considerably, as pointed out by Glimm et al. (2001).

Whilst magnetic field strength is the only parameter altered between successive runs of this initial “B” set, this leads to a secondary constraint on the physics of the system: the ratio of the dominant scale of the instability (λ_u , from equation 1.26) to domain width (L_x) approximately predicts the number of bubbles which are able to develop along the direction of magnetic field. If this is below unity, equation 1.26 will no longer give the characteristic scale size of the simulation, as this would be larger than the simulated domain. This suggests that λ_u/L may affect the growth rate (either linear or nonlinear) RTi, and so a further set of simulations were run with constant magnetic field strength but variable width. These displayed nonlinear growth rates which varied as much as the first B set, however, with no apparent correlation. However, the lack of correlation in the W simulations suggests that the correlation in the B simulations is reliable and that enhanced magnetic field strength leads to lower growth-rates.

In order to measure the nonlinear growth rate of the RTi (α in equation 1.28), the gradient of a curve such as those plotted in Figure 4.9 is often commonly used. However, a precise value of α for each simulation is difficult to measure, as this is an attempt to describe the average behaviour of the nonlinear system; the nonlinearity itself implies fluctuations which will change α on small timescales. Moreover, the transition between linear and nonlinear regimes of the instability is ill-defined, so the α measurement starting point can be difficult to choose. As a good approximation, the eigenfunction for the vertical velocity v_z is given by

$$v_z(z) = Ae^{-k|z|} \quad (4.8)$$

(Chandrasekhar 1961), which implies that $1/k$ can be used as the vertical scale through which the perturbation can travel before it reaches its nonlinear saturation.

Furthermore, in order to compare distinct occurrences of the RTi, should the same points in time be used for each, or should instances with larger scales

(and a later onset of terminal velocity and hence longer nonlinear growth regime, as defined above) be measured for longer? To complicate things further, none of the growth rate curves, observed or simulated, are perfectly straight over any of their evolution. Considering that previously published values have a somewhat large variance (up to a factor 2 disagreement) and frequently are measured over only two or three points, I believe that this is a far more complicated problem than it first appears.

4.5 Conclusions

This work analysed bubbles developing into a large cloud of ejected material following a massive filament eruption on the 7th of June 2011. The nonlinear growth rate was found to be an order of magnitude greater than that predicted by both previous observational studies and theoretical models. This has been attributed to a combination of outflows impacting the ejecta and the multi-directional initial velocities which the material appears to undergo.

Simulations of the RTi were then conducted in order to better understand how magnetic field strength may affect the growth rate of this instability. It has been found from previous work that nonlinear growth rate is enhanced when a strong magnetic field is present (c.f. the hydrodynamic case), however, this study has found that increasing the strength of the magnetic field leads to a decrease in nonlinear growth rate. This is speculated to be due to higher magnetic tension requiring greater energy in order for the frozen-in plasma to move. Nonlinear growth rates were found to converge on ~ 0.039 for the strongest magnetic fields studied.

The simulations were conducted in a slightly different regime to the environment in which the observations were collected; $J = c_A^2/gL$ was estimated to be approximately 0.8 for the observations, whereas this ranged between 0.06 – 0.36 in the simulations. However, this factor ~ 2 difference is far too small to cause the observed order-of-magnitude discrepancy in nonlinear growth rate, α . More importantly, both observations and simulations have $J < 1$. The curves of observed bubble height as a function of time squared appear congruent with that of the simulations, supporting the proposed oc-

currence of the RTi.

Chapter 5

Estimating the Total Mass of An Unusual Eruptive Filament

I would like to thank Lidia van Driel Gesztelyi, Gherardo Valori and Pascal Demoulin for their enlightening suggestions on the magnetic topology of the filaments and eruptions studied in this project, and Huw Morgan for calculating the mass of the associated CME.

For the final project in this thesis, I turned my attention to a particularly interesting series of eruptions which occurred over the 14th and 15th of March 2015 from AR12297. To the west of this active region lay an intermediate filament (IF) of approximately 300 Mm in length, in a sigmoid-like shape. This filament had been growing since it was first seen to rotate into view on the 8th of March 2015, though it is difficult to judge this initial size due to projection effects; on the 11th, however, it appears roughly 150 Mm.

One leg of the IF appears to be rooted close to the strong concentration of positive polarity in the centre of AR12297, extending outwards along PILs both north and south of the positive polarity, which each begin and end in the same locations (see Figure 5.1). Moving along the southward PIL, the IF protrudes southwards but quickly curves to the west, whilst the filamentary material above the northern PIL can be less clearly seen. The other footpoint is rooted among diffuse patches of negative polarity to the west. The overlying field appears to be similarly configured, with loops rooted in the active region and the diffuse negative polarity to the south and south-west. Figure 5.2 shows

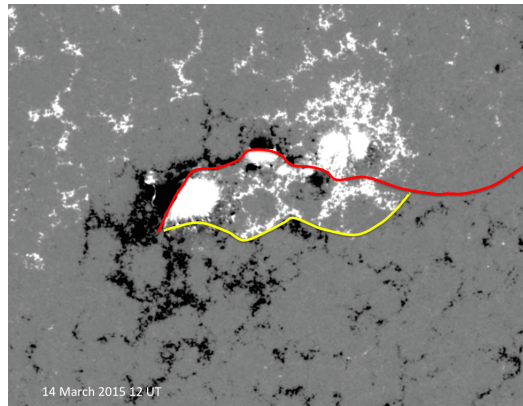


Fig. 5.1: PILs in AR12297 which are thought to support filament material. Image courtesy Lidia van Driel-Gesztelyi.

the configuration of the AR and IF a day before erupting.

At 11:45 UT on the 14th of March 2015, an eruption is seen to occur from AR12297, though this could be considered a failed eruption, as much of the material appears to be confined by overlying magnetic field (however, a low-mass, slow-moving CME is seen in coronagraph images following the eruption). The material which is (not completely) ejected appears to originate from the footpoint of the IF rooted in the AR, emitting brightly in EUV wavelengths and forming a spray-like ejecta emanating from a sunspot umbra, seeming to move higher in the solar atmosphere than the filament before becoming supported in a quasi-static fashion in the dips of a large magnetic arcade above two PILs, where it cools and becomes visible in absorption. This is shown in Figures 5.3 and 5.4. The centre-of-mass and volume of material seems approximately static, but fine structure can be seen ‘sloshing about’, like water in a swinging hammock. Some is seen to stream down magnetic field lines rooted in the diffuse negative polarity to the south-west of the AR, but then the remaining material gradually ‘settles down’, forming a beautiful little condensation of filament plasma by approximately 20:00 UT; if this is indeed supported by the dips in the overlying field, this would point to the sheared arcade model, though not a typical case. The small size, unconventional formation and position above an IF make this a most fascinating filament. The IF appears relatively unchanged following this eruption.

The layout of the magnetic field is postulated in Figure 5.4. This shows

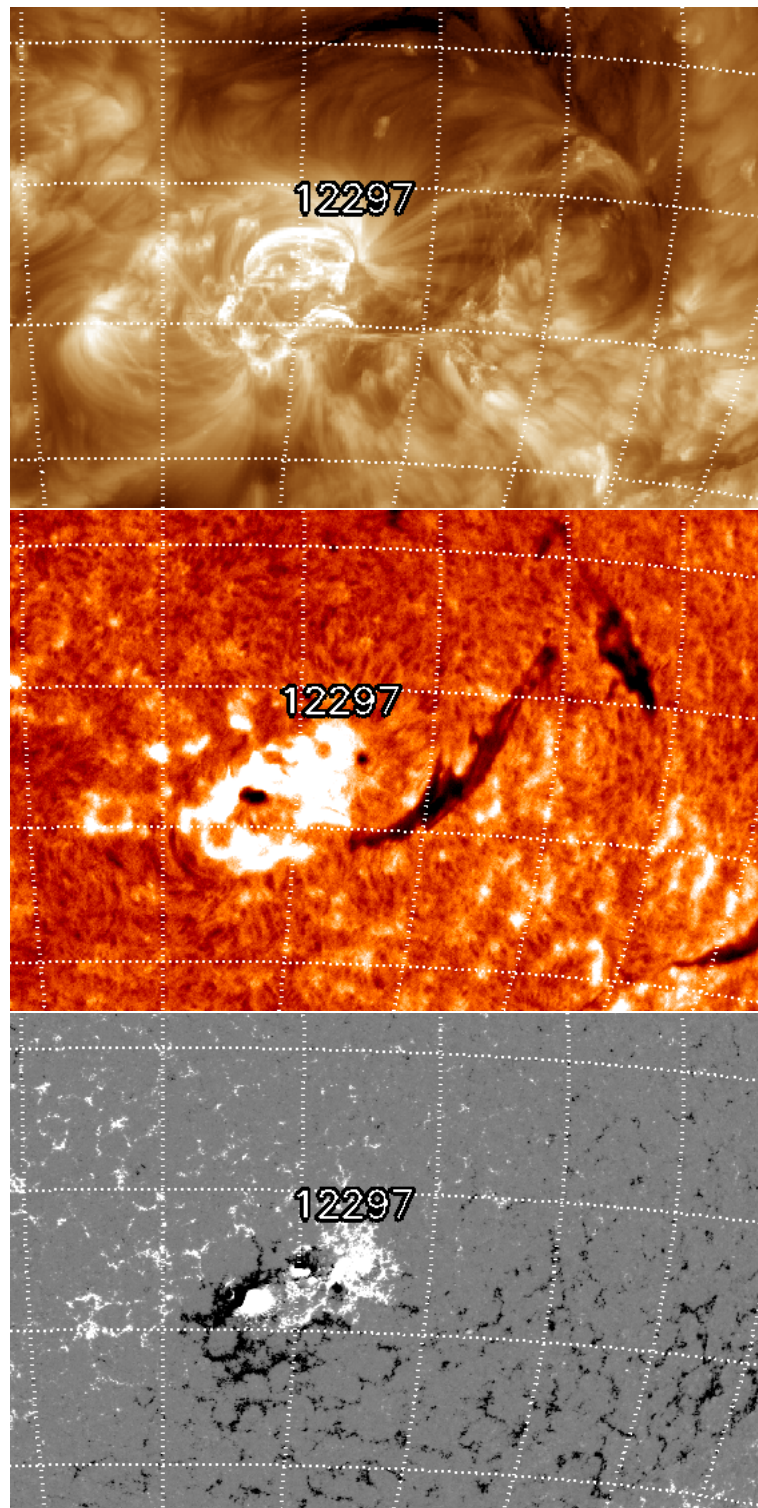


Fig. 5.2: AR12297 shown at roughly 22:00 UT on the 13th of March 2015 (pre-eruption) in the SDO/AIA 193 Å channel, an H α image from Big Bear Solar Observatory, and an SDO HMI magnetogram. The large IF can be seen clearly in the H α image, protruding from the west of the AR. Images from solarmonitor.org.

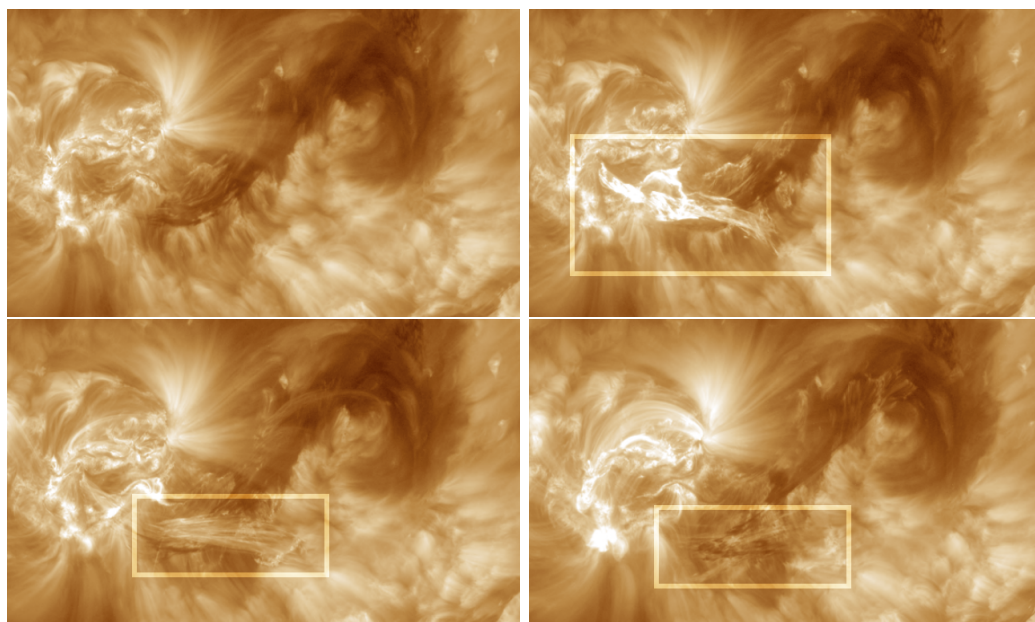


Fig. 5.3: The spray-like ejecta emanating from AR12297 seen by the SDO/AIA 193 Å channel. The top left image shows the AR and IF moments before the eruption at 11:38 UT; top right shows the material emitting strong EUV radiation just after the eruption (highlighted by the box) at 11:55 UT; the bottom left shows the material becoming less bright in EUV and remaining in place at 12:22 UT; and the bottom right shows the material becoming visible in absorption at 14:42 UT.

AR12297, the IF protruding from the west, and the overlying field supporting the smaller filament. The footpoints of the overlying magnetic field can be seen to have a larger separation in the more diffuse negative polarity. The filaments remain like this until 00:40 UT on the 15th of March 2015, when another eruption occurs from the AR. The smaller filament begins to lift off, accelerating and erupting completely. The material quickly becomes diffuse, though a large bulk of it can be seen to move off the limb. This is overtaken by material ejected from lower down in the solar atmosphere, leaving behind a dimming region just below the location of the original IF. Post-flare loops are then seen to form rooted in flare ribbons; these are where the original overlying field was and so the southern footpoints, rooted in the diffuse negative polarity, move outwards faster than the northern, which are rooted in the strong concentrations of the AR. Figure 5.5 shows the AR and IF at four points along the evolution, including before both eruptions, between the two, and after both.

By extending the density calculation method only slightly, the total mass of the target may be calculated as well as the column density. This would give the method added applicability, allowing for a more meaningful result, as column density can be a perceptually difficult quantity. However, before proceeding, it is important to note that for a total mass calculation, the goodness-of-fit of the model to the data should be optimal, otherwise the data will not be included in the target material selection, and a further underestimation of the total mass will be made (since the calculated column density is a lower limit as discussed in Chapter 3).

It is for this reason that I decided to investigate whether the column density calculation method could be improved on. The 94 Å channel has a much poorer signal-to-noise ratio than the other four used, and so the removal of this channel from the calculation may influence the result for the better, despite the fact that this would reduce the number of data points to fit the model by 20%. A comparison of the target filament in this Chapter is shown in both 94 Å and 171 Å in Figure 5.6 to highlight the lower quality of the former; in fact the 94 Å image shows mostly noise and hardly any solar structure.

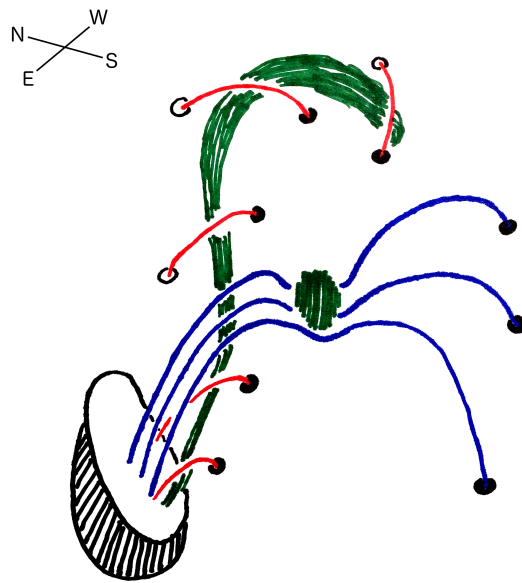


Fig. 5.4: A cartoon showing the postulated magnetic configuration of AR12297, the associated IF and the overlying magnetic arcade which supports the smaller filament. Black outlines illustrate surface magnetic polarity (white for positive, black for negative), red lines show low-lying sheared magnetic field constraining the IF, blue lines represent the overlying arcade whose dips support the smaller filament, and green shows the location of the material seen in absorption.

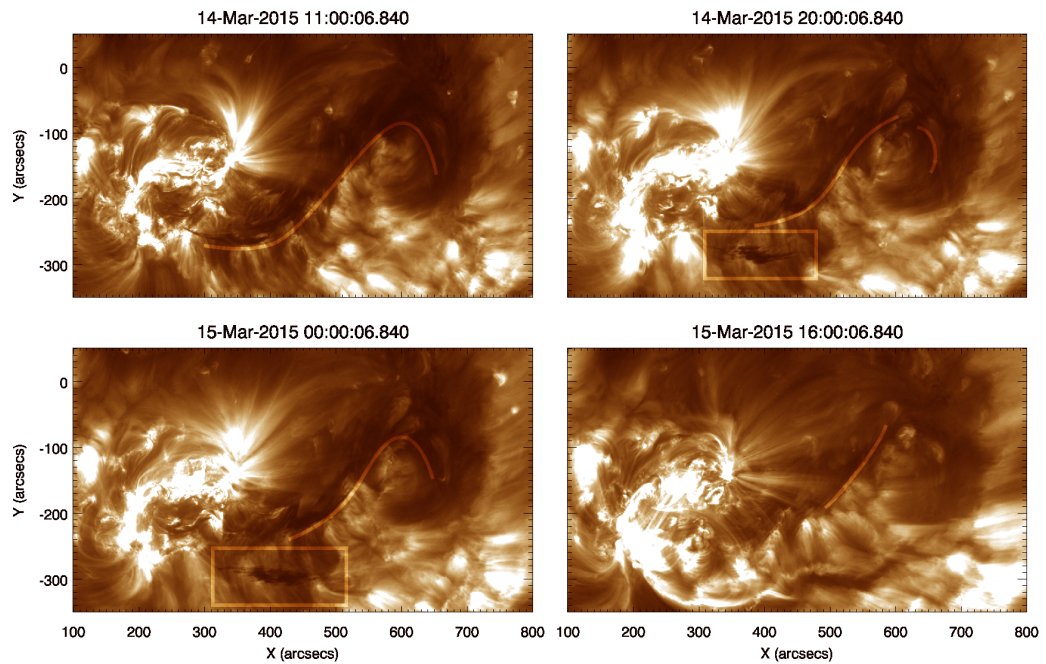


Fig. 5.5: AR12297 is shown on the left of these images, with the IF protruding to the west. The images have been corrected for solar rotation and as such only the first image axes are accurate co-ordinates. The first image (at 11:00 UT) is before both eruptions with a line drawn just to the south of the IF to highlight its position, the next two (20:00 and 00:00 UT) are between the two eruptions with the IF and smaller filament highlighted, and the final image is some time after the second eruption with the remaining IF highlighted. Note that these images have been derotated to keep the AR in the centre of view; the co-ordinates apply to the first image.

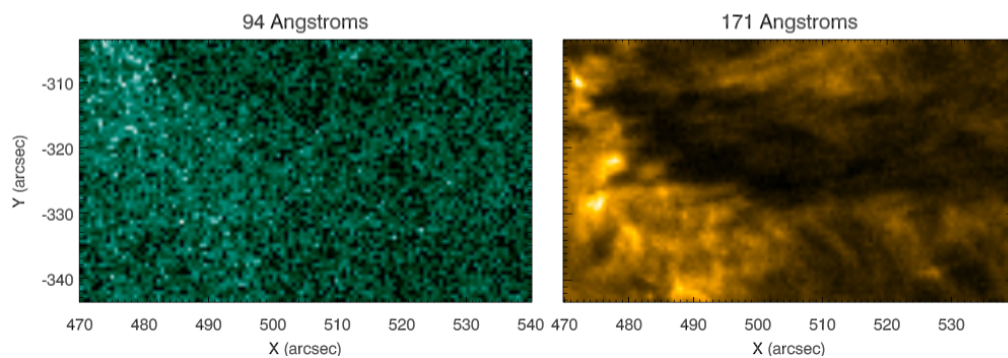


Fig. 5.6: 94 Å image (left) and 171 Å (right) of filament material examined in this Chapter.

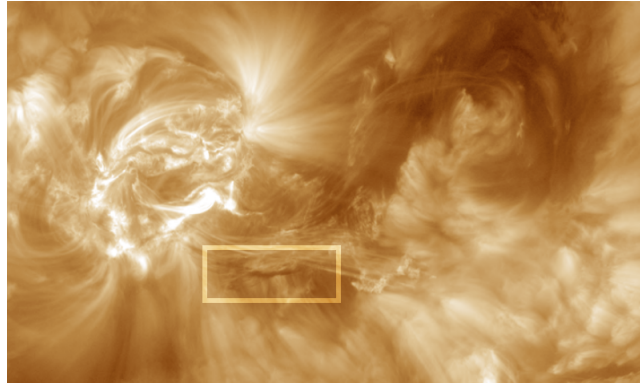


Fig. 5.7: Target 1; the box highlights a portion of the IF which is seen to move over a quiescent background, shown in the 193 Å channel of SDO/AIA at 12:33 UT on the 14th of March 2015.

The view of this event from SDO allows the column density (and hence total mass) to be calculated for filament material in several different locations. Particularly of note is the smaller filament, which can be seen clearly in totality just before the second eruption, which gives a clear view of the background radiation field just before the flare-loops set in.

5.1 Observations

The whole system was observed continuously for the entire (series of) event(s), between 11:00 UT on the 14th of March 2015 and ~06:00 UT on the 15th of March 2015, by SDO/AIA (see Section 2.1) in all required bandpasses: 94, 131, 171, 193 and 211 Å. Targets were chosen from the most dynamic material with apparently quiescent background radiation fields.

It was not possible to apply the column density calculation to the larger IF as a whole, as this structure does not appear to move much over the duration of the observations, and whilst material is evacuated from the eastern side of the IF, the background radiation field here is within the AR – far too dynamic to be used as a background frame in this method. However, the southernmost point of the filament (where the axis lies east-west) is seen to move slightly south and then back again as the first eruption takes place; at 12:20 UT to be precise. This is outside the AR and as such is deemed suitable to be analysed. This is Target 1, shown in Figure 5.7.

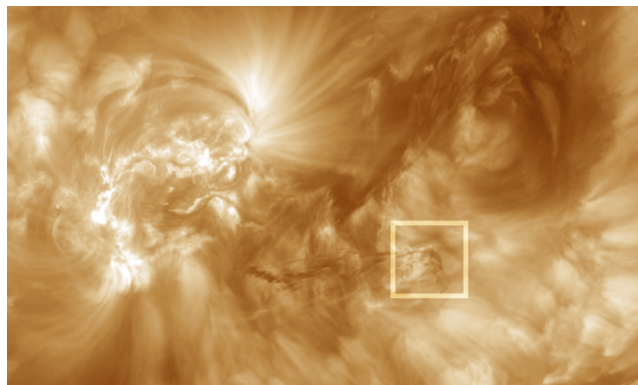


Fig. 5.8: Target 2; the box highlights a portion of the smaller filament which is apparently moving down the magnetic legs of the arcade supporting it, shown in the 193 Å channel of SDO/AIA at 16:00 UT on the 14th of March 2015.

Following the first eruption, lots of dynamic material is seen in emission in the EUV wavelengths examined in the general vicinity of the AR, which prevents column density analysis of the smaller filament as it is forming. However, some of the material which appears to move down the leg of a magnetic field line from the smaller filament passes over a quiescent background field very briefly at 15:04 UT on the 14th of March 2015, and so this material was also analysed as Target 2, shown in Figure 5.8.

Some time after the first eruption, but before the second, the environment becomes slightly more ‘settled’: the smaller filament appears almost stationary, and much less material in emission (virtually none) can be seen moving through the corona. The smaller filament, whilst described as lying ‘above’ the larger IF, is not in fact co-located with the IF from our point of view; that is, along no LOS from Earth (or, rather SDO) do both filaments lie. Not only this, but the background radiation field of the smaller filament is glimpsed just after the second eruption, before the post-flare loops appear in emission. This makes the pre-eruption smaller filament (at 00:23 UT on the 15th of March 2015) the perfect target for this column density calculation. This, Target 3, is used to investigate and refine the method itself, since it is so easily applied to this filament, and is shown in Figure 5.9.

At the onset of the second eruption, material is seen to be ejected from the AR, initially appearing bright (*i.e.*, in emission), but becoming visible as

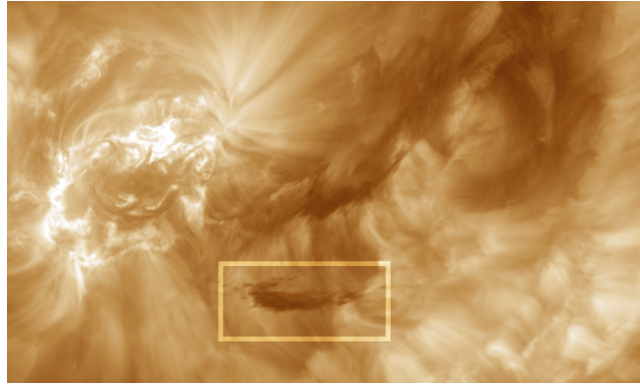


Fig. 5.9: Target 3; the box highlights the smaller filament moments before the second eruption, shown in the 193 Å channel of SDO/AIA at 00:23 UT on the 15th of March 2015.

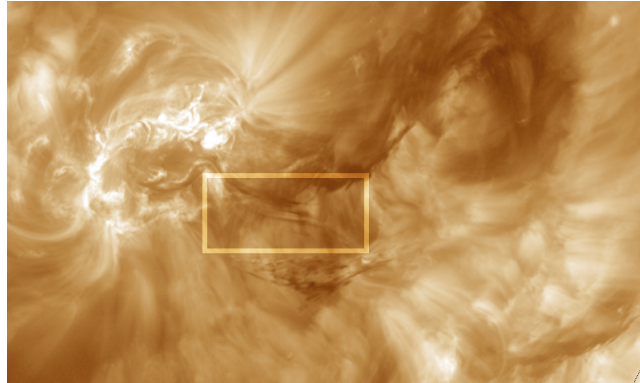


Fig. 5.10: Target 4; the box highlights material ejected from the AR passing in front of quiescent background, shown in the 193 Å channel of SDO/AIA at 00:47 UT on the 15th of March 2015.

absorbing material just after passing away from the AR at 00:47 UT on the 15th of March 2015. This mass motion happens in a very short space of time (~ 5 minutes) and so the background radiation field barely seems to change at all. This makes this material the perfect target for mass analysis. Target 4 is shown in Figure 5.10.

Following the eruption, the bulk of material from the smaller filament can be followed towards the limb as it is ejected out into the heliosphere. Whilst it does indeed become diffuse rapidly, it is possible to apply the column density calculation method once more at 01:19 UT on the 15th of March 2015, before losing sight of it completely in these wavelengths. The bulk of material as it is moving out into the upper corona is shown in Figure 5.11.

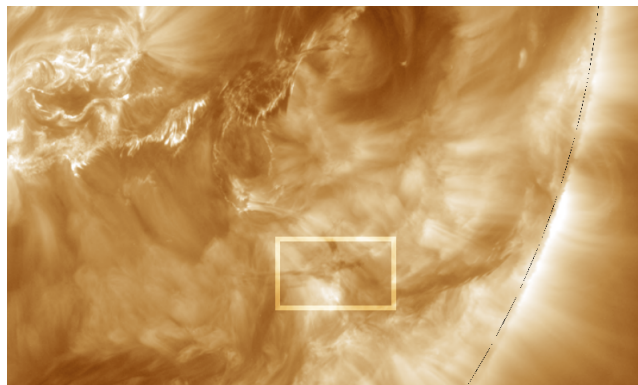


Fig. 5.11: Target 5; the box highlights the bulk of material from the smaller filament as it is being ejected into the heliosphere, shown in the 193 Å channel of SDO/AIA at 01:19 UT on the 15th of March 2015.

5.2 Refining the Column Density Calculation

Firstly the column density calculation method was applied unchanged (with respect to Chapter 3) to Target 3, the pre-eruption smaller filament at 00:23 UT, to provide a base for comparison with further iterations of the technique; this will be referred to as Target 3a. The method was then applied to the same target and background frames, this time omitting the 94 Å channel, referred to as Target 3b.

The resulting column density values for Target 3a and 3b are shown in Figure 5.12. Removing the 94 Å channel gives a smoother distribution of column density values and fewer ‘spikes’, *i.e.*, values which appear to have hit the saturation limit of the colour table used – meaning we have returned fewer values above $10^{20.1} N_H \text{ cm}^{-2}$. This also results in more pixels being included in the data presented, indicating a greater number of pixels which have both $0.5 < G < 1.0$ and $0.1 < \chi_v^2 < 10$.

The errors on N_H for Targets 3a and 3b are shown in Figure 5.13. The same masking criteria are used as for Figure 5.12. From visual inspection we can see that removing the 94 Å channel, which has the largest measurement errors on DN, has improved the errors for our calculated column density values.

The calculated values for geometric depth $0.5 < G < 1.0$ for Target 3a and b are shown in Figure 5.14. Figure 5.15 shows all $G \leq 0.5$ or $G = 1.0$ for Target 3a and 3b to make it easier to spot any pixels which fall outside

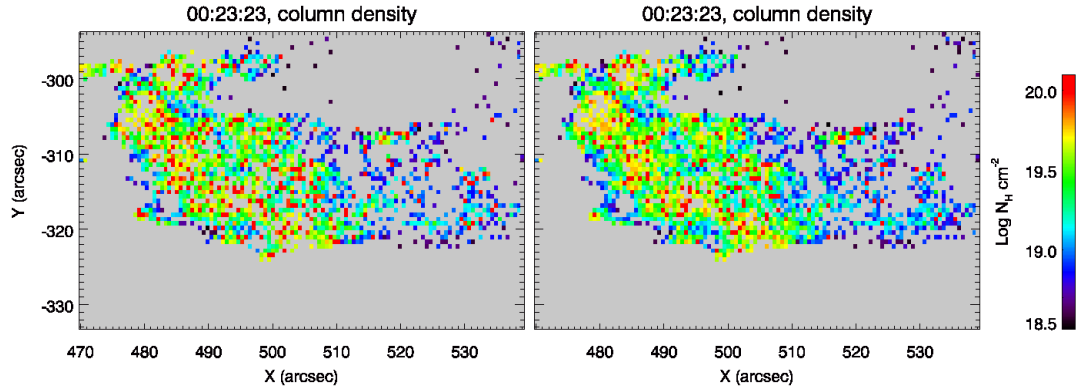


Fig. 5.12: Calculated column density values for the pre-eruption filament with the 94 Å bandpass included (3a, left) and omitted (3b, right). Only pixels with $0.5 < G < 1.0$ and $0.1 < \chi^2_{\nu} < 10$ are presented.

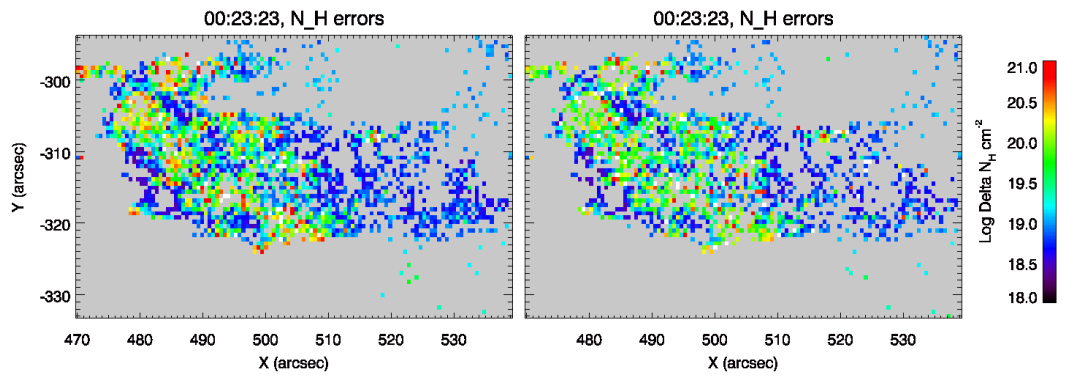


Fig. 5.13: Errors on calculated values of N_H for $0.5 < G < 1.0$ and $0.1 < \chi^2_{\nu} < 10$ of the pre-eruption filament with the 94 Å bandpass included (3a, left) and omitted (3b, right).

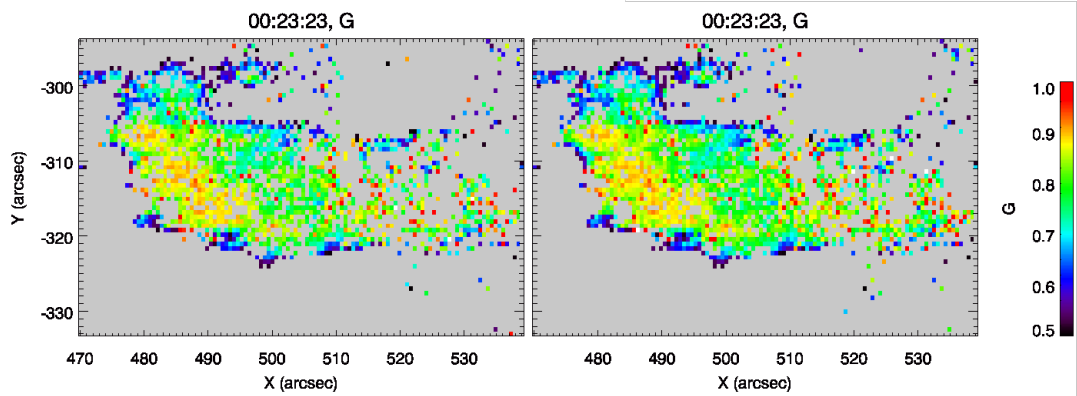


Fig. 5.14: Calculated geometric depth values for $0.5 < G < 1.0$ and $0.1 < \chi_\nu^2 < 10$ of the pre-eruption filament with the 94 \AA bandpass included (3a, left) and omitted (3b, right).

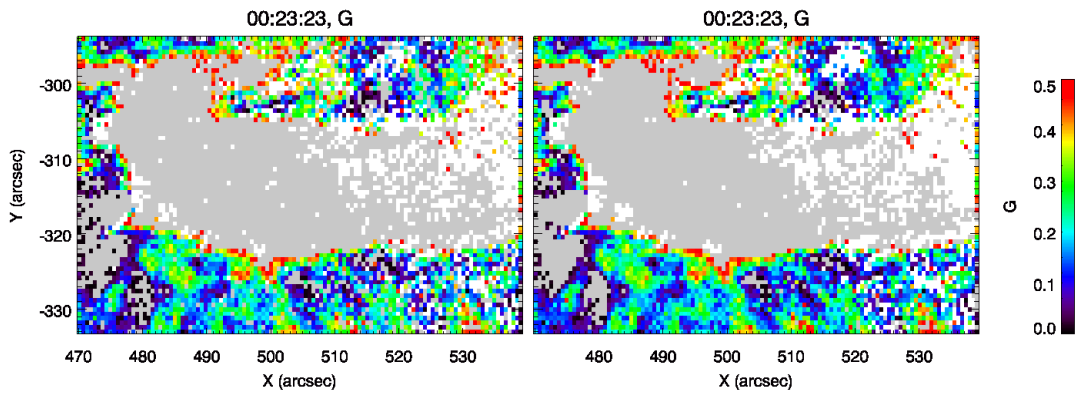


Fig. 5.15: Calculated geometric depth values for $G \leq 0.5$ or $G = 1.0$ (presented as white) of the pre-eruption filament with the 94 \AA bandpass included (3a, left) and omitted (3b, right) (for all χ_ν^2).

the cutoff within the visual edge of the target. This highlights that a greater number of pixels within the visual edge of the blob have $G = 1$, particularly to the west of the blob, suggesting that removing the 94 \AA channel may not be entirely beneficial.

Reduced goodness-of-fit χ_ν^2 in the target (*i.e.*, $0.5 < G < 1.0$) is shown in Figure 5.16, and a higher mean and median value can be seen when the 94 \AA channel is included (3a, left). This is examined further in Figure 5.17, where only ‘bad’ χ_ν^2 values in the target are shown, that is pixels with $\chi_\nu^2 < 0.1$ or $\chi_\nu^2 > 10$. This shows that removing the 94 \AA channel improves the fit of the model to the data. This is supported by the mean value of χ_ν^2 for

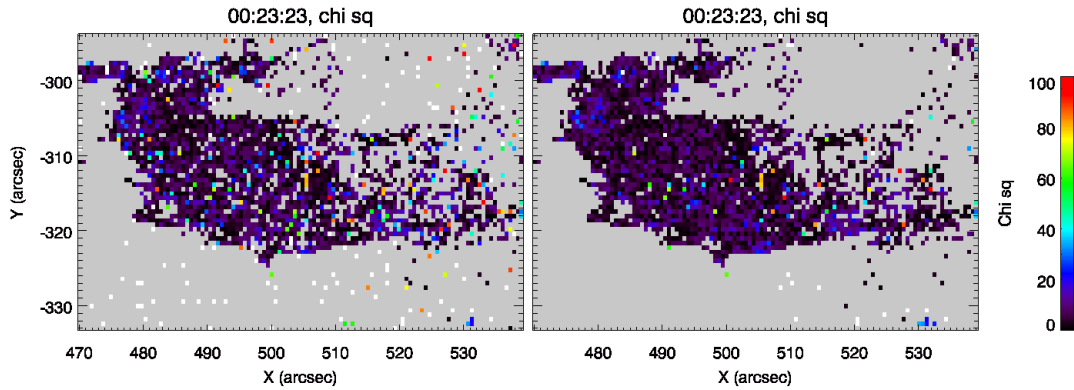


Fig. 5.16: χ_ν^2 values for $0.5 < G < 1.0$ of the pre-eruption filament with the 94 Å bandpass included (3a, left) and omitted (3b, right).

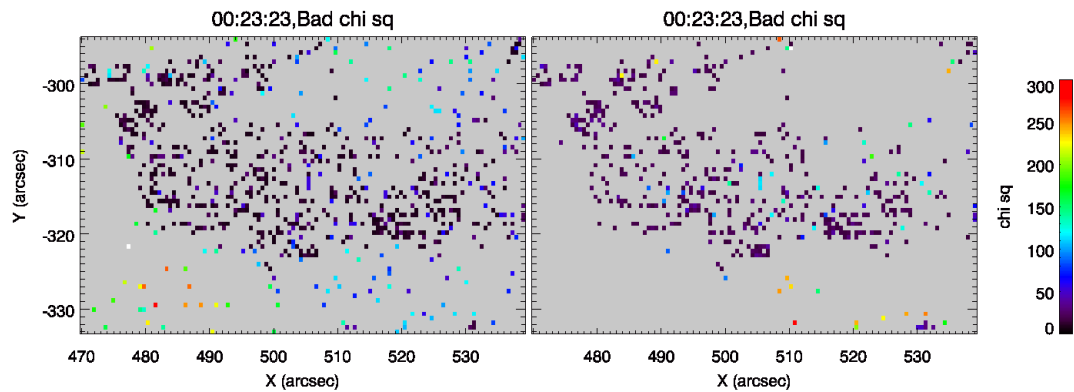


Fig. 5.17: ‘Bad’ χ_ν^2 values (*i.e.*, $\chi_\nu^2 < 0.1$ or $\chi_\nu^2 > 10$) for $0.5 < G < 1.0$ of the pre-eruption filament with the 94 Å bandpass included (3a, left) and omitted (3b, right).

$0.5 < G < 1.0$; target 3a has $\langle \chi_\nu^2 \rangle = 11.13$, which falls above the cutoff of 10, while b has $\langle \chi_\nu^2 \rangle = 6.62$, well within our acceptable range.

Since improved χ_ν^2 and errors are obtained by omitting the 94 Å channel, this channel will not be used for column density calculation henceforth, and Target 3b will now be referred to as Target 3.

5.3 Mass Investigation

5.3.1 Method

It is a trivial exercise to convert from column density of hydrogen to total hydrogen mass by using the area of the target and the mass of a hydrogen atom. In order to do this we simply multiply the three values together to find the total mass in a pixel and then sum over all target pixels (*i.e.*, where

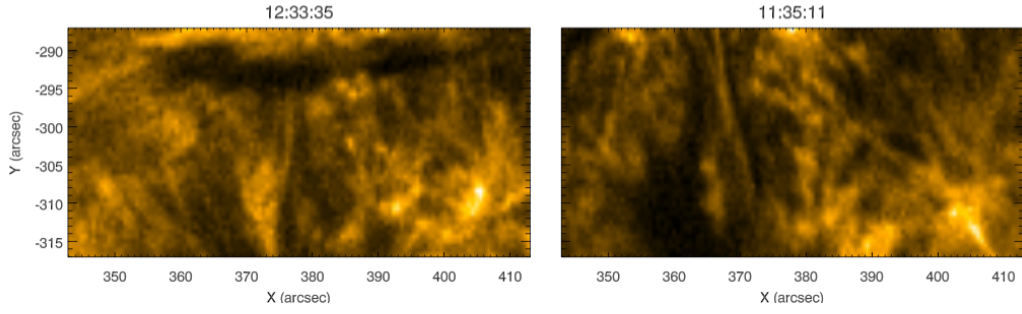


Fig. 5.18: 171 Å image of Target 1 (left) and associated background (right) frames.

$0.5 < G < 1.0$ and $0.1 < \chi_\nu^2 < 10$), that is

$$M_H = \sum_{target} N_H a_{pix} m_H, \quad (5.1)$$

where M_H is the total hydrogen mass of the target, a_{pix} is the area of a pixel, m_H is the mass of a hydrogen atom, and we are summing over all target pixels. The area of a pixel is given by the angular width of a pixel on the SDO/AIA CCD, $\sim 0.6''$ and $1''$ at the Sun-Earth distance is approximately 725 km: therefore, the area of a pixel on the solar surface in CGS is $0.6 \times 725 \times 10^5 = 1.89 \times 10^{15}$ cm (see Chapter 2). The mass of a hydrogen atom is $\sim 1.673 \times 10^{-24}$ g.

5.3.2 Total Target Masses

For each target, all pixels with $0.5 < G < 1.0$ and $0.1 < \chi_\nu^2 < 10$ are counted, and the mean column density and total mass of these pixels are returned.

Target 1, the southernmost portion of the IF, is shown with its associated background in Figure 5.18. This target frame is found to contain 683 target pixels with mean column density $\bar{N}_H = 4.73 \times 10^{19}$ cm $^{-2}$ and total mass $M_H = 2.03 \times 10^{14}$ g; the column density map is presented in Figure 5.19.

Target 2, which consists of a portion of the smaller filament as it appears to fall down the magnetic legs of the supporting arcade, is shown with its associated background in Figure 5.20. This frame is found to contain 361 target pixels with mean column density $\bar{N}_H = 3.70 \times 10^{19}$ cm $^{-2}$ and total mass $M_H = 1.75 \times 10^{14}$ g; the column density map is presented in Figure 5.21.

Target 3, the smaller filament in totality, is shown in Figure 5.22 and has

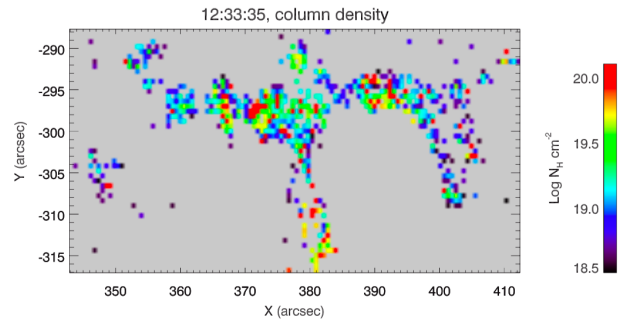


Fig. 5.19: Column density of a small portion of the IF, Target 1.

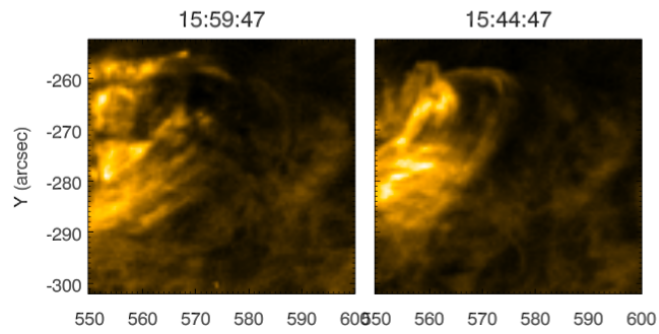


Fig. 5.20: 171 Å image of Target 2 (left) and associated background (right) frames.

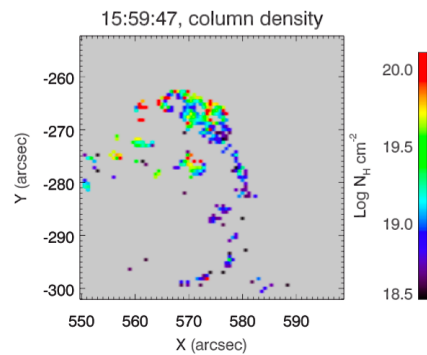


Fig. 5.21: Column density of material falling from the smaller filament, Target 2.

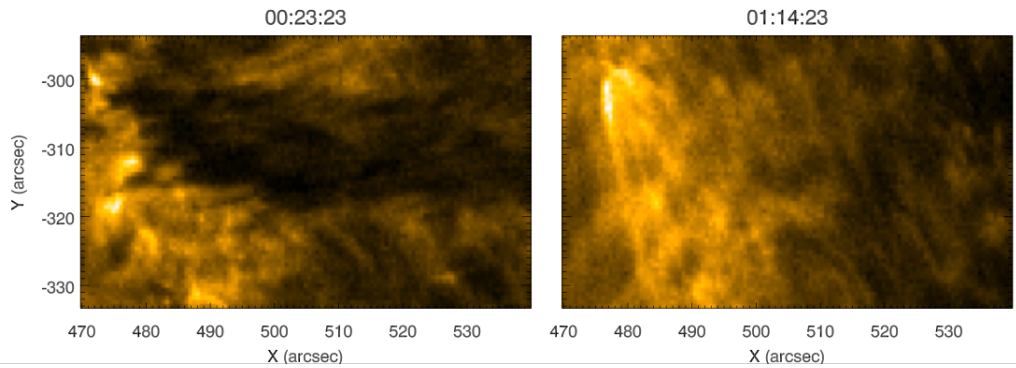


Fig. 5.22: 171 Å image of Target 3 (left) and associated background (right) frames.

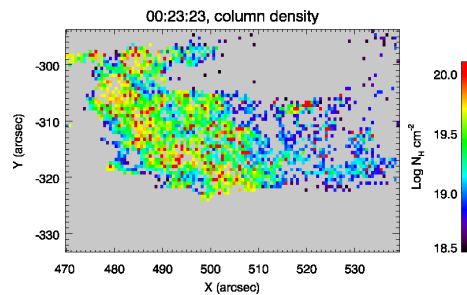


Fig. 5.23: Column density of the smaller filament, Target 3.

2109 target pixels with $0.5 < G < 1.0$ and $0.1 < \chi_\nu^2 < 10$. These have a mean column density $\bar{N}_H = 4.34 \times 10^{19} \text{ cm}^{-2}$ and total hydrogen mass $M_H = 4.50 \times 10^{14} \text{ g}$. Column density results for Target 3 are presented in Figure 5.23.

Target 4 is composed of material being ejected from AR12297 at the onset of the second eruption, and is shown in Figure 5.24. This shows the 1010 target pixels which have a mean column density $\bar{N}_H = 4.80 \times 10^{19} \text{ cm}^{-2}$ and total hydrogen mass $M_H = 2.32 \times 10^{14} \text{ g}$. Column density results for Target 4 are presented in Figure 5.25.

Target 5 is the ‘main bulk’ of the filament, which can just about be seen moving in a reasonably straight line into the corona and out of view. The target and background frame are shown in Figure 5.26, and column density is shown in Figure 5.27. In this window there are 807 target pixels with mean column density $\bar{N}_H = 1.52 \times 10^{19} \text{ cm}^{-2}$ and total hydrogen mass $M_H = 5.80 \times 10^{13} \text{ g}$.

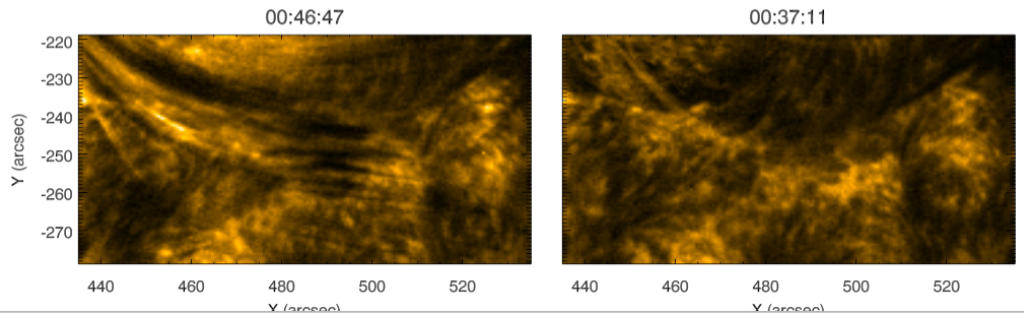


Fig. 5.24: 171 Å image of Target 4 (left) and associated background (right) frames.

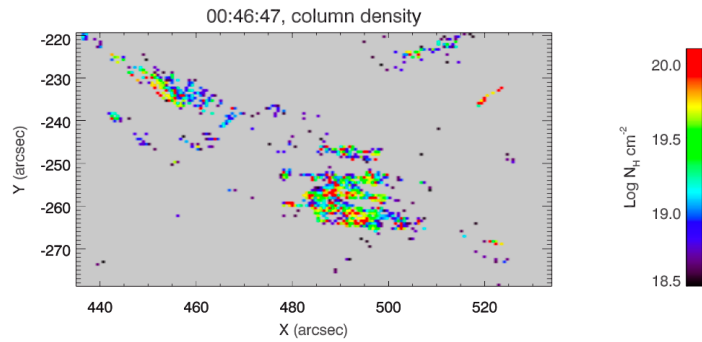


Fig. 5.25: Column density of material ejected from the AR, Target 4.

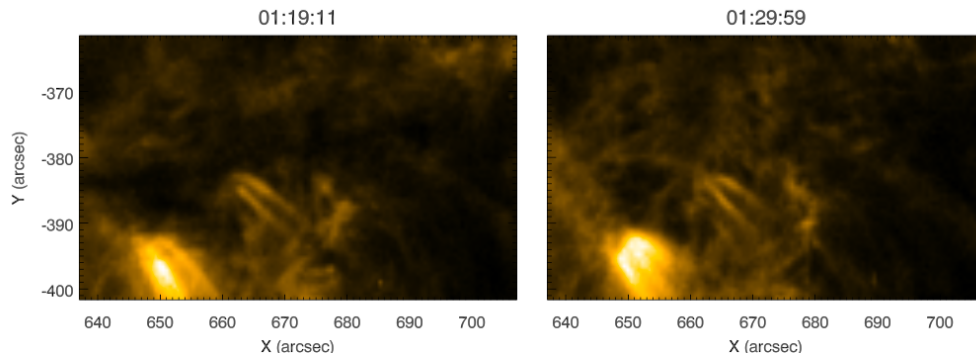


Fig. 5.26: 171 Å image of the target (left) and background (right) frames a few minutes after the onset of eruption, Target 5.

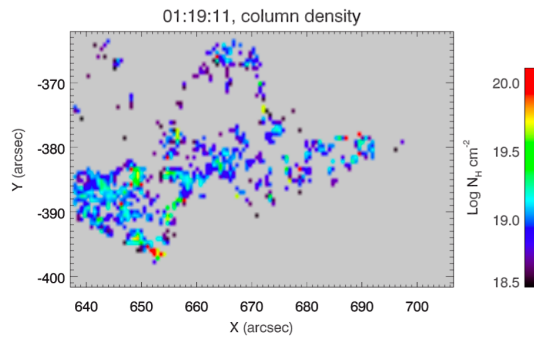


Fig. 5.27: Column density of the main bulk of the erupted filament material, Target 5.

5.3.3 Estimating the Total Filament and Eruption Mass

The main bulk of the eruptive IF towards the west does not change in intensity appreciably in EUV wavelengths over the course of events, while much of the material towards the east becomes visible in emission, suggesting heating. For this reason, it was not possible to use the column density calculation method on the entire filament to find its mass. However, Target 1 belongs to the IF, and so extrapolations based on assumptions, outlined below, can be made in order to estimate the total mass.

The filament is roughly 300 Mm in length and 10 Mm in width based on visual inspection in multiple wavelengths; the clearest view is given by $H\alpha$ observations, presented in Figure 5.2. The average hydrogen column density of Target 1 is $\bar{N}_H = 4.73 \times 10^{19} \text{ cm}^{-2}$, and based on intensities of the wavelengths observed by SDO/AIA, this material appears to be representative of the bulk of material. The total hydrogen mass is then

$$M_{IF-H} = \bar{N}_H a_{IF-H} m_H, \quad (5.2)$$

with the area $a_{IF} = 3 \times 10^{10} \times 1 \times 10^9 = 3 \times 10^{19} \text{ cm}^2$, $M_{IF} = 2.4 \times 10^{15} \text{ g}$. This is of comparable order in filament size and mass as previously published values, though the average column density in Target 1 is slightly higher than those found by Schwartz et al. (2015): between $3.8 - 16.5 \times 10^{18} \text{ cm}^{-2}$.

By examining the area of the IF following the eruption in the same way, the filament appears to be reduced in size by at least a factor 2, and the drop in intensity by absorption also appears to be reduced. Figure 5.28 shows AR12297 and the IF on the 15th of March 2015 in $H\alpha$, to be compared with Figure 5.2 taken on the 13th. Therefore, based on the estimated pre-eruption mass, material of the order 10^{15} g was ejected from the IF during the two eruptions, though how much of this went on to escape to the heliosphere is unclear.

5.4 Discussion

The series of events which unfolded over the 14th and 15th of March 2015 involving a large, eruptive intermediate filament and associated active region AR12297 are particularly interesting. Not only are two eruptions seen to occur

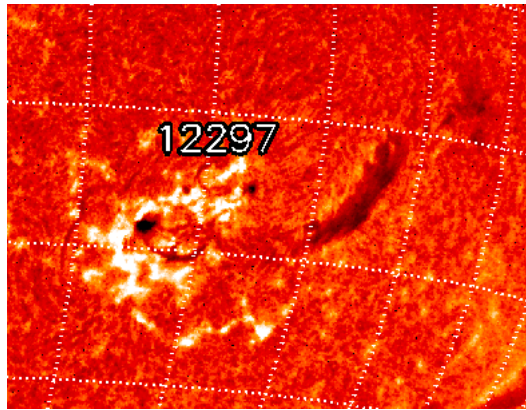


Fig. 5.28: AR12297 and the IF in $H\alpha$ at 07:00 UT on the 15th of March 2015, from solarmonitor.org.

from roughly the same source location of the AR within just 13 hours of one another, but the spray-like ejecta from the first (failed) eruption forms a high-lying, small, dense filament above the other. Neither of these is a common observation.

The small ‘blob’ of material comprising Target 3 has been referred to as a small filament throughout this Chapter, postulated to be described by the sheared arcade filament model, the mass supported by possible dips. However, whether this can truly be considered a filament is debatable. The mass is approximately above a PIL (although offset towards the south-west, lying over mainly dispersed negative-polarity fields), and the structure consists of dense, chromospheric material supported in the corona by magnetic field; this fulfils the definition of a filament. On the other hand, this object is much smaller than typical filament sizes, and the formation from spray-like ejecta apparently being captured by an overlying arcade is not typical. It also appears to be considerably higher in the atmosphere than filaments are often observed, and its short lifespan is another feature distinguishing the blob from ordinary filaments. The crux of this problem lies with the difficulty of dividing observed physical phenomena into discrete categories; reality rarely has such well-defined, distinct regimes.

Large amounts of mass are involved in the series of events; not only does each eruption cast a considerable amount of material into the solar atmosphere,

but equally a lot of mass appears to remain in the precursor structures. For each target studied, relatively high column densities are found (*c.f.* previous studies outlined in Chapter 1 and work presented earlier in this thesis, most notably Chapter 3), which would suggest strong magnetic fields are present in order to support this mass in the low- β corona.

Target 1 (see Figures 5.18 and 5.19) is the only column density measurement which was able to be made for the IF, and shows a reasonably high column density $\bar{N}_H = 4.73 \times 10^{19} \text{ cm}^{-2}$; Schwartz et al. (2015) recently published the average column density of six quiescent filaments ranging between $3.8 - 16.5 \times 10^{18} \text{ cm}^{-2}$. However, this does not necessarily mean that the IF studied here is unusual, as IFs may be more dense than QFs due to stronger magnetic fields in the associated AR being able to support more mass. This also leads to the idea that perhaps the assumption that Target 1 is representative of the whole IF may be incorrect, as it is located very close to the AR.

Some locations in Target 1 which do not appear to be part of the IF have also been identified by the method as target material; where the IF is at the top of Figure 5.19, two patches can be seen just to the south. It is not clear whether this is ejected material in the target frame or simply an increase in intensity in these locations at the time of the background frame. This also means the total mass calculated for Target 1 is an overestimate, however, the strict condition that $0.5 < G < 1$ means some pixels containing target material may not be counted, introducing a source of potential underestimate.

Target 2 (see Figures 5.20 and 5.21) is a relatively small target, and the mean column density is only slightly lower than that of Target 1: $\bar{N}_H = 3.70 \times 10^{19} \text{ cm}^{-2}$. This is surprising, as this material was ejected from the AR over 4 hours prior, but the comparable column density to the IF suggests that the material either did not expand appreciably during the eruption, or was of a very high density pre-eruption, or expanded upon eruption and then re-condensed in the corona.

Target 3 (see Figures 5.22 and 5.23) is the smaller ‘filament’ in total-ity. This has a high mean column density relative to all targets examined,

($\bar{N}_H = 4.34 \times 10^{19} \text{ cm}^{-2}$), and has the largest area (approximately 10^{19} cm^2) and highest total mass ($M_H = 4.50 \times 10^{14} \text{ g}$). However, the west side of this target appears to have caused the method some problems, as fewer pixels are identified as target material.

Examining the details of this target presented in Section 5.2, it is interesting to notice that locations where $G = 1.0$ are more common towards the west of the target (see Figure 5.15); recalling from Chapter 3, $G = 1.0$, which has the physical implication that there is no foreground emission whatsoever, which is unrealistic, or this could also be due to the least-squares minimisation hitting a wall in parameter space, suggesting no good fit was found. These pixels are therefore discarded from the results. The calculated column density here is generally lower (see Figure 5.12). Figure 5.29 shows the calculated absorption depth $d(\lambda)$ in the four SDO/AIA bandpasses used (note that here all pixels with $0.5 < G$ are shown as well as $G = 1$). This shows a discrepancy in $d(\lambda)$ between the wavelengths which is larger towards the right of the target, where G is seen to reach unity.

Recalling from and rearranging equations 3.6 and 3.7,

$$d(\lambda) = \left(1 - \frac{I_{obs}}{I_b + I_f}\right) \quad (5.3)$$

and

$$G = f \frac{I_b}{I_b + I_f} \quad (5.4)$$

(where I_{obs} is the intensity with the target material obscuring the background, I_b and I_f are background and foreground emission respectively and f is pixel-filling factor) we see that a smaller $d(\lambda)$ means a smaller difference between the obscured and unobscured intensities; the right of Target 3 has a considerably smaller $d(\lambda)$ relative to the left in the 171 Å bandpass especially, and this can be seen to correlate with the difference in intensity between target and background frame from a qualitative examination of Figure 5.22. The result of $G = 1$ suggests this larger change in $d(\lambda)$ across wavelengths is not only due to a lower column density.

The result of $G = 1$ would mean the pixel was completely filled with material ($f = 1$), which is not unfeasible, but also that there is no foreground

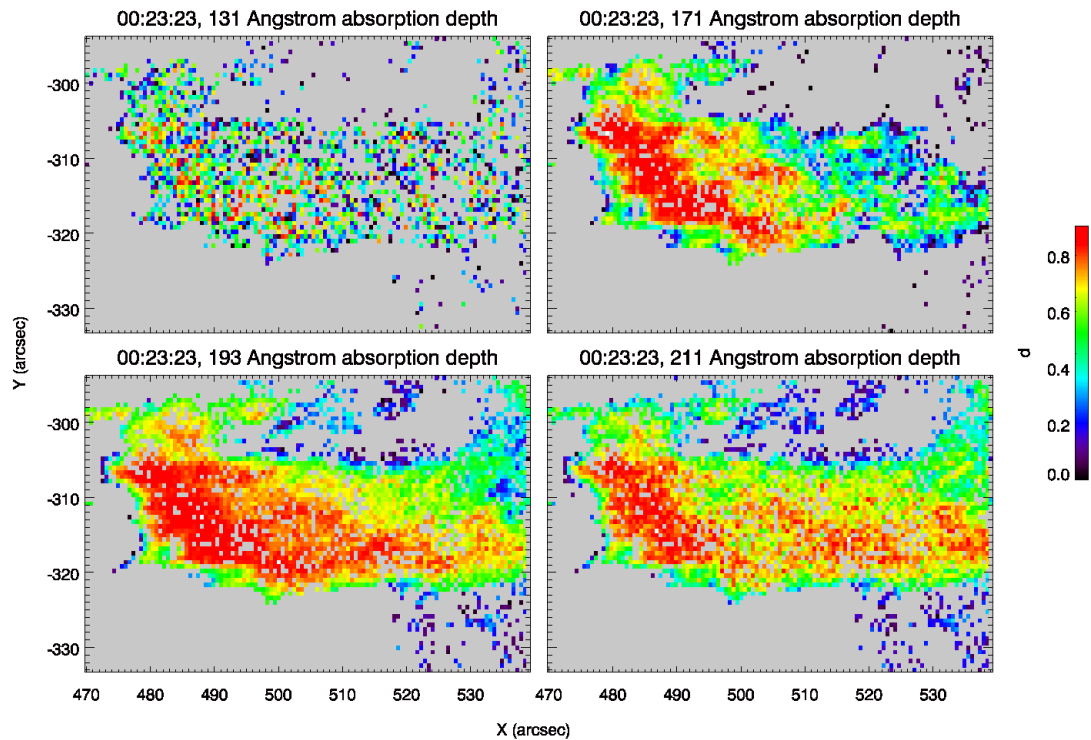


Fig. 5.29: Calculated absorption depth values for the pre-eruption filament in the four bandpasses used. Only pixels with $0.5 < G$ and $0.1 < \chi_\nu^2 < 10$ are presented.

emission ($I_f = 0$). The latter is unlikely as the corona is of a sufficient temperature and density and composition to emit in the wavelengths which are used in this work at heights above where this material is situated. As mentioned in Chapter 3, pixels with this value of G are therefore not used in assessing column density, nor total mass.

Target 4 (see Figures 5.24 and 5.25) is material ejected by the AR at the onset of the second eruption. This material was not captured particularly well, as background frame selection proved to be tricky. Following the eruption, high intensity EUV radiation is emitted by both material in the chromosphere and dense material suspended and moving in the corona. Therefore, the background frame was taken to be moments before the eruption – but some brightening has already occurred by the time the target frame is taken. In the event that the true background is brighter than the selected background frame, the column density will be underestimated; the mean column density is in fact found to be reasonably high, $\bar{N}_H = 4.80 \times 10^{19} \text{ cm}^{-2}$. Upon further

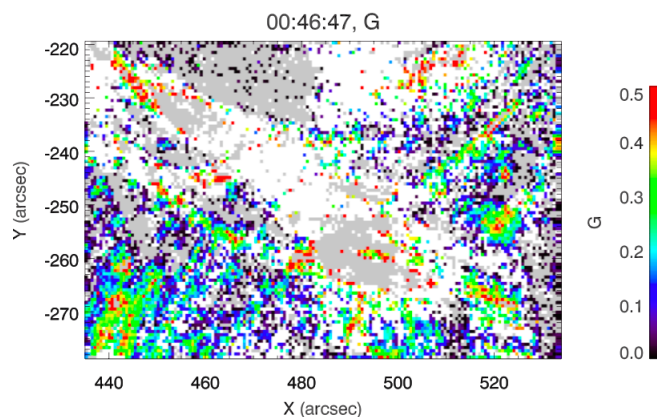


Fig. 5.30: Geometric depth $G \leq 0.5$ and $G = 1$ for Target 4.

investigation, many pixels with $G = 1$ are seen in this target frame, shown in Figure 5.30, co-located with brightenings in the target frame (see Figure 5.24).

Target 5 (see Figures 5.26 and 5.27) is well captured by the method due to the high speed of the material allowing for a closely temporally located background frame to be used. This target has a lower column density and total mass than the other targets, $\bar{N}_H = 1.52 \times 10^{19} \text{ cm}^{-2}$ and $M_H = 5.80 \times 10^{13} \text{ g}$; this target is the main bulk of the smaller filament following its eruption, and it is interesting to note that both values have fallen by an order of magnitude relative to the pre-eruption structure, Target 3. However, much of the filament material expands and becomes transparent in EUV channels rapidly, preventing mass assessment by this method.

The mass of the precursor IF has been estimated as $M_{IF} = 2.4 \times 10^{15} \text{ g}$, though some assumptions have gone into this: most importantly, that the mean column density of Target 1 is representative of the whole filament, which may be incorrect since the strongest magnetic fields supporting the IF are closest to the AR – where Target 1 is measured.

By visual inspection of the IF before and after the eruption, *i.e.*, by comparing Figures 5.2 and 5.28, at least half of the material appears to have been removed from the filament over the two eruptions (by visual inspection of the area) – of the order 10^{15} g . How much of this was ejected in the associated CME and how much was returned to the surface is not clear, but the total mass of the CME has been estimated from white-light scattered coronagraph

images to be 1.2×10^{15} g (Huw Morgan, personal communication; Morgan (2015)). Not all of this mass is necessarily from the filament, which forms the core of the CME, as the coronal material swept-up by the front of the CME makes up a reasonable percentage of the total mass – possibly up to 50%. Therefore it is reasonable to postulate that more than half of the mass of the precursor IF was involved in the eruption, and of that, more than half went on to form the core of the CME, in agreement with results presented here.

One possible further improvement to the column density calculation method is investigating the influence of the initial guess that both G and N_H have on results. Even better, the need for an initial guess in the fitting method could be removed entirely, by designing a program to find the χ^2 space for a range of G and N_H for one pixel, and use this to find the best initial guess. A problem with this is that it requires prior knowledge of the location of a characteristic pixel of target material to calculate the χ^2 space for. Another solution is to use a different fitting technique, such as a Markov chain Monte Carlo (MCMC) method, which identify the true minimum χ^2 much more efficiently by investigating multiple parts of parameter space simultaneously. This should be investigated in future iterations of this method (see Section 6.2).

5.5 Conclusions

The column density calculation method introduced in Chapter 3 has been shown to give results with improved goodness-of-fit to the model when the noisy 94 Å channel is removed. It may be possible to improve upon the method further by improving upon or removing the need for the initial guess used in determining the best fit, perhaps by employing MCMC methods.

The method has been used to investigate an IF protruding from the edge of AR12297 as it is seen to undergo a failed eruption on the 14th of March 2015, creating a smaller, unusual filament, suspended in the overlying magnetic arcade, then erupting again, successfully ejecting huge amounts of material from the IF and the smaller filament completely. Column densities of several portions of material associated with the IF and eruption are found to have

mean values between $1.52 - 4.80 \times 10^{19} \text{ cm}^{-2}$.

The total mass of hydrogen of the smaller filament has been calculated to be $M_H = 2.03 \times 10^{14} \text{ g}$. By assuming the precursor IF is uniformly composed of similar density material to the targets studied over its area of $3 \times 10^{19} \text{ cm}^2$, I estimate the total precursor IF hydrogen mass to be approximately $2.4 \times 10^{15} \text{ g}$. By visual inspection, more than half of this material appears to be lost over the course of the two eruptions, however it is unclear how much of the mass which ‘disappeared’ went on to escape the corona. The mass of the CME accompanying the second eruption was found to be approximately $1.2 \times 10^{15} \text{ g}$ from coronagraph data, which is a compatible value with the total mass estimated here.

Chapter 6

Summary, Conclusions & Future Work

6.1 Summary & Conclusions

In this thesis I have presented a quasi-spectroscopic method for calculating column density of material in absorption by utilising the simultaneous multi-wavelength observations of SDO/AIA. The high resolution and cadence of this instrument allows for the density and total mass determination on small and highly dynamic structures of sufficiently dense and ionised (or rather, sufficiently neutral) chromospheric material present in the corona, manifested for example as filaments and eruptions. The method has been successfully applied to both pre- and post-eruption filament material and it has been used to calculate the total mass of a filament prior to erupting. The method itself has been investigated by examining the effect of omitting a channel with poorer signal-to-noise than the other four, which was found to improve the method. I believe the method could be further improved upon by removing the need for an initial guess for the least-squares minimisation algorithm.

The technique was first applied to back-falling matter following an eruption with an unusually large volume of ejecta on the 7th of June 2011; although this material was seen to expand up to two orders of magnitude (in plane-of-sky projected area), the discreet condensations of ejecta were found to have column density comparable to pre-eruption filaments, of the order $\sim 2 \times 10^{19} \text{ cm}^{-2}$ (both from previous publications and later confirmed by further investigation in this thesis).

The method was also applied to a pair of eruptions involving an IF on

the 14th and 15th of March 2015. The column density of a portion of the large IF was calculated to be approximately $\bar{N}_H = 4.73 \times 10^{19} \text{ cm}^{-2}$. By approximating the area of the IF as $3 \times 10^{19} \text{ cm}^2$, I estimate a total hydrogen mass of $M_H = 2.4 \times 10^{15} \text{ g}$. A smaller filament which is seen to form above the IF following the first eruption is also analysed, and found to have $\bar{N}_H = 4.34 \times 10^{19} \text{ cm}^{-2}$ and total hydrogen mass $M_H = 4.50 \times 10^{14} \text{ g}$. This is then ejected during the second eruption, which also drains much of the IF of material. By visual inspection, it appears that over half the filament mass is lost. The associated CME has been measured to have a total mass of $2.4 \times 10^{15} \text{ g}$ from coronagraph data, in agreement with the total mass estimations made here.

During the investigation into the back-falling material, I became intrigued by the morphology and dynamics of the ‘blobs’ as they fell through the solar atmosphere; a repeated, self-similar bifurcation can be seen which is consistent with the Rayleigh-Taylor instability (RTi). Previous publications have shown that the material involved in this eruption is RT-unstable, though none have examined the ‘blobs’ in this context. By using basic linear theory of the RTi, I used my calculated column density, a depth estimate using STEREO and the observed bifurcation scales to estimate a characteristic magnetic field strength of the order 1 G.

I then decided to examine the postulated RTi in the main bulk of the ejecta, before the smaller blobs had separated and began to fall back, as large bubbles indicative of the RTi can be seen developing into this bulk shortly after the initial eruption. The growth rate of these bubbles was measured, though this was so large (with respect to that predicted by analytic theory) that I speculate that some outflow from lower down in the atmosphere is affecting the development of the instability, and also that the bulk of material may not initially be at rest, making it nigh on impossible to determine the position of the front of a bubble with respect to the initial interface.

In order to attempt to learn more about the instability in this context, I conducted some numerical MHD simulations of RT-unstable material with varying magnetic field strength, and found that the growth rate for bubbles

is reduced for stronger magnetic fields. However, the change in growth rate between runs may be due to a changing ratio of characteristic wavelength to simulated domain size, as confirmed by a further set of runs which kept magnetic field strength constant but altered the width of the domain. This second set showed approximately equal variation in growth rate between runs as the first set, although here there seemed to be no correlation. Unfortunately, this uncertainty, combined with the difficulty of assessing the true growth rate of the observations, meant I was unable to comment on the characteristic magnetic field strengths associated with the main bulk of the the 7th of June 2011 ejecta shortly after erupting.

6.2 Future Work

Whilst I am coming to the end of my PhD research project, I do not view this as an ending; there is much further work I would like to undertake, and in this section I will outline the main aims for the near future of my career.

Firstly, I believe the work presented in Chapters 4 and 5 is suitable for publication in an astrophysical or solar physics journal, and as such I plan to write each up as an article to be submitted to a suitable journal.

I would like to continue investigating the mass of eruptive filaments using the quasi-spectroscopic column density calculation technique, ultimately undertaking an extensive study of many eruptive filaments, in order to better understand more about the typical behaviours of these and hopefully learn more about the underlying mechanisms. However, before moving ahead with such work, I feel the method can be improved upon further by introducing Markov chain Monte Carlo (MCMC) methods to replace the least-squares minimisation fitting. I would like to rewrite the code completely using Python, as this is freely available to all, and I would like to distribute the method to anyone who would like to make use of it. This would allow me to optimise the way in which the technique works, as well as introduce the MCMC methods. The abundances used in the equations could also be further investigated; I have no reason to believe the value which is currently used to be incorrect (taken from a publication within the last decade), however it is not something which

requires further consideration.

It could be possible to utilise the method using the two passbands on STEREO below 227 Å (171 and 195 Å) to examine larger-scale material, though with only two datapoints for a model with two free parameters, another approach may need to be considered. In fact, I would like to extend the method to return monochromatic column density estimates, that is using only a single band-pass. This will most likely have a greater uncertainty associated with the results, however this means that it would be possible to estimate total mass of absorbing material from a much greater array of instruments. I have been accepted onto the Guest Investigator program for the SWAP instrument on PROBA2, which is similar to the 171 Å SDO/AIA filter, with a lower resolution and larger field-of-view ($54' \times 54'$); a monochromatic column density estimate would be ideal for such an instrument, and I hope to be able to follow filament eruptions out to several solar radii by off-pointing SWAP.

I would also like to extend my work to examine *non*-eruptive filaments, especially polar-crown filaments. I am interested to learn how these massive structures are built up over several solar rotations, how the mass within them is distributed and evolves, and work alongside colleagues at MSSL investigating the build-up of flux-ropes by flux cancellation to determine whether this is related to the mass distribution. A possible problem with this investigation could be a difficulty in obtaining background frames for the stationary QFs. It could be possible to create a model background radiation field to use in the column density calculation method, based on the intensities of the solar surface surrounding the QF. Whilst this would introduce uncertainty regarding variation in the true background radiation field, this would also allow for a much higher cadence of data to be analysed. Virtually every image captured by AIA could be analysed, which would help with identifying anomalous results caused by small-scale brightenings (*etc.*) behind the filament material.

I also hope to continue examining possible occurrences of the RTi in filament ejecta; I have recently had discussions with Andrew Hillier regarding the true nature of the relationship between length scales and magnetic field strength in this instability, and we have realised that the relationship between

the observed scales and the strength of the associated magnetic field may be more nuanced than we have assumed in this work. For example, the modes across and along the magnetic field are not causally related, however there could be some correlative relationship between the two, though more analytic work is required.

Finally, I would like to conduct a further set of simulations of RT-unstable plasma, specifically with stratified (as opposed to uniform) density layers in order to investigate what, if any, effect this has on the RT growth rate (both linear and nonlinear). By applying the density calculation code to observed RT-unstable plasma and examining the density stratification, it would be useful to understand how this will affect the instability.

Chapter 7

List of Publications

7.1 Peer-reviewed Journals

- J. Carlyle, D. R. Williams, L. van Driel-Gesztelyi, L. Green, G. Valori (2016), Estimating the total mass of an eruptive quiescent filament which led to an unexpectedly geoeffective magnetic storm, *in prep.*
- J. Carlyle, D. Innes, A. Hillier, L. Guo (2016), Nonlinear growth rate of the magnetic Rayleigh-Taylor instability in observations and simulations of erupted filament plasma, *in prep.*
- J. Carlyle, D. R. Williams, L. van Driel-Gesztelyi, D. Innes, A. Hillier, S. Matthews (2014), Investigating the dynamics and density evolution of returning plasma blobs from the 2011 June 7 eruption, *The Astrophysical Journal*, 782, 87, DOI: 10.1088/0004-637X/781/1/1
- L. van Driel-Gesztelyi, D. Baker, T. Török, E. Pariat, L. M. Green, D. R. Williams, J. Carlyle, G. Valori, P. Démoulin, B. Kliem, D. M. Long, S. A. Matthews, J. M. Malherbe (2014), Coronal magnetic reconnection driven by CME expansion – the 2011 June 7 event, *The Astrophysical Journal*, 788, 85, DOI: 10.1088/0004-637X/788/1/85
- D. Baker, D. H. Brooks, P. Démoulin, L. van Driel-Gesztelyi, L. M. Green, K. Steed, J. Carlyle (2014), Plasma composition in a sigmoidal anemone active region, *The Astrophysical Journal*, 778, 69, DOI: 10.1088/0004-637X/778/1/69

7.2 Conference Proceedings

- J. Carlyle, D. R. Williams, L. van Driel-Gesztelyi, D. Innes (2014), Density evolution of in-falling prominence material from the 7th June 2011 CME, *Proceedings of the IAU*, 300, 401, DOI: 10.1017/S1743921313011277
- L. van Driel-Gesztelyi, D. Baker, T. Török, E. Pariat, L. M. Green, D. R. Williams, J. Carlyle, G. Valori, P. Démoulin, S. A. Matthews, B. Kliem, J. M. Malherbe (2014), Magnetic reconnection driven by filament eruption in the 7 June 2011 event, *Proceedings of the IAU*, 300, 502, DOI: 10.1017/S1743921313011745
- D. Baker, D. H. Brooks, P. Démoulin, L. van Driel-Gesztelyi, L. M. Green, K. Steed, J. Carlyle (2014), FIP bias in a sigmoidal active region, *Proceedings of the IAU*, 300, 222, DOI: 10.1017/S1743921313011009

Bibliography

- Antiochos, S. K. and DeVore, C. R. (1999), The Role of Helicity in Magnetic Reconnection: 3D Numerical Simulations, *Washington DC American Geophysical Union Geophysical Monograph Series* **111**, 187.
- Carlyle, J., Williams, D. R., van Driel-Gesztelyi, L., Innes, D., Hillier, A. and Matthews, S. (2014), Investigating the Dynamics and Density Evolution of Returning Plasma Blobs from the 2011 June 7 Eruption, *The Astrophysical Journal* **782**, 87.
- Chae, J. (2003), The Formation of a Prominence in NOAA Active Region 8668. II. Trace Observations of Jets and Eruptions Associated with Canceling Magnetic Features, *The Astrophysical Journal* **584**, 1084–1094.
- Chandrasekhar, S. (1961), *Hydrodynamic and hydromagnetic stability*, International Series of Monographs on Physics, Oxford, Clarendon.
- Chen, P. F. (2011), Coronal Mass Ejections: Models and Their Observational Basis, *Living Reviews in Solar Physics* **8**.
- Cho, K.-S., Lee, J., Gary, D. E., Moon, Y.-J. and Park, Y. D. (2007), Magnetic Field Strength in the Solar Corona from Type II Band Splitting, *The Astrophysical Journal* **665**(1), 799.
- DeVore, C. R. and Antiochos, S. K. (2000), Dynamical Formation and Stability of Helical Prominence Magnetic Fields, *The Astrophysical Journal* **539**(2), 954.
- Dimonte, G., Youngs, D. L., Dimits, A., Weber, S., Marinak, M., Wunsch, S., Garasi, C., Robinson, A., Andrews, M. J., Ramaprabhu, P., Calder, A. C.,

- Fryxell, B., Biello, J., Dursi, L., MacNeice, P., Olson, K., Ricker, P., Rosner, R., Timmes, F., Tufo, H., Young, Y.-N. and Zingale, M. (2004), A comparative study of the turbulent Rayleigh–Taylor instability using high-resolution three-dimensional numerical simulations: The Alpha-Group collaboration, *Physics of Fluids (1994-present)* **16**(5), 1668–1693.
- Downs, C., Roussev, I. I., van der Holst, B., Lugaz, N. and Sokolov, I. V. (2012), Understanding SDO/AIA Observations of the 2010 June 13 EUV Wave Event: Direct Insight from a Global Thermodynamic MHD Simulation, *The Astrophysical Journal* **750**(2), 134.
- Driesman, A., Hynes, S. and Cancro, G. (2008), The STEREO Observatory, *Space Science Reviews* **136**, 17–44.
- Evans, C. R. and Hawley, J. F. (1988), Simulation of magnetohydrodynamic flows - A constrained transport method, *The Astrophysical Journal* **332**, 659–677.
- Gary, G. A. (2001), Plasma Beta above a Solar Active Region: Rethinking the Paradigm, *Solar Physics* **203**(1), 71–86.
- Gilbert, H., Kilper, G., Alexander, D. and Kucera, T. (2011), Comparing Spatial Distributions of Solar Prominence Mass Derived from Coronal Absorption, *The Astrophysical Journal* **727**, 25.
- Gilbert, H. R., Holzer, T. E. and MacQueen, R. M. (2005), A New Technique for Deriving Prominence Mass from SOHO/EIT Fe XII (19.5 Nanometers) Absorption Features, *The Astrophysical Journal* **618**, 524–536.
- Gilbert, H. R., Inglis, A. R., Mays, M. L., Ofman, L., Thompson, B. J. and Young, C. A. (2013), Energy Release from Impacting Prominence Material Following the 2011 June 7 Eruption, *The Astrophysical Journal* **776**(1), L12.
- Glimm, J., Grove, J. W., Li, X. L., Oh, W. and Sharp, D. H. (2001), A Critical Analysis of Rayleigh–Taylor Growth Rates, *Journal of Computational Physics* **169**(2), 652 – 677.

- Goff, C. P., van Driel-Gesztelyi, L., Démoulin, P., Culhane, J. L., Matthews, S. A., Harra, L. K., Mandrini, C. H., Klein, K. L. and Kurokawa, H. (2007), A Multiple Flare Scenario where the Classic Long-Duration Flare Was Not the Source of a CME, *Solar Physics* **240**, 283–299.
- Grevesse, N., Asplund, M. and Sauval, A. J. (2007), The Solar Chemical Composition, *Space Science Reviews* **130**(1-4), 105–114.
- Grigis, P., Su, Y. and Weber, M. (2012), AIA PSF Characterization and Image Deconvolution, Tech Rep., SDO/AIA Team (NASA, LMSAL, SAO).
- Guo, L.-J., Huang, Y.-M., Bhattacharjee, A. and Innes, D. E. (2014), Rayleigh-Taylor Type Instabilities in the Reconnection Exhaust Jet as a Mechanism for Supra-arcade Downflows in the Sun, *The Astrophysical Journal Letters* **796**, L29.
- Hathaway, D. H. (2010), The Solar Cycle, *Living Reviews in Solar Physics* **7**.
- Heinzel, P., Schmieder, B., Fárník, F., Schwartz, P., Labrosse, N., Kotrc, P., Anzer, U., Molodij, G., Berlicki, A., DeLuca, E. E., Golub, L., Watanabe, T. and Berger, T. (2008), Hinode, TRACE, SOHO, and Ground-based Observations of a Quiescent Prominence, *The Astrophysical Journal* **686**, 1383–1396.
- Hillier, A., Berger, T., Isobe, H. and Shibata, K. (2012), Numerical Simulations of the Magnetic Rayleigh-Taylor Instability in the Kippenhahn-Schlüter Prominence Model. I. Formation of Upflows, *The Astrophysical Journal* **746**(2), 120.
- Innes, D. E., Cameron, R. H., Fletcher, L., Inhester, B. and Solanki, S. K. (2012), Break up of returning plasma after the 7 June 2011 filament eruption by Rayleigh-Taylor instabilities, *Astronomy & Astrophysics* **540**, L10.
- Isobe, H., Miyagoshi, T., Shibata, K. and Yokoyama, T. (2005), Filamentary structure on the Sun from the magnetic Rayleigh–Taylor instability, *Nature* **434**(7032), 478–481.

- Jun, B.-I., Norman, M. L. and Stone, J. M. (1995), A Numerical Study of Rayleigh-Taylor Instability in Magnetic Fluids, *The Astrophysical Journal* **453**, 332.
- Kliem, B. and Török, T. (2006), Torus Instability, *Physical Review Letters* **96**(25).
- Labrosse, N., Heinzl, P., Vial, J. C., Kucera, T., Parenti, S., Gunár, S., Schmieder, B. and Kilper, G. (2010), Physics of Solar Prominences: I—Spectral Diagnostics and Non-LTE Modelling, *βr* **151**, 243–332.
- Landi, E. and Reale, F. (2013), Prominence Plasma Diagnostics through Extreme-ultraviolet Absorption, *The Astrophysical Journal* **772**, 71.
- Lemen, J. R., Title, A. M., Akin, D. J., Boerner, P. F., Chou, C., Drake, J. F., Duncan, D. W., Edwards, C. G., Friedlaender, F. M., Heyman, G. F., Hurlburt, N. E., Katz, N. L., Kushner, G. D., Levay, M., Lindgren, R. W., Mathur, D. P., McFeaters, E. L., Mitchell, S., Rehse, R. A., Schrijver, C. J., Springer, L. A., Stern, R. A., Tarbell, T. D., Wuelser, J.-P., Wolfson, C. J., Yanari, C., Bookbinder, J. A., Cheimets, P. N., Caldwell, D., Deluca, E. E., Gates, R., Golub, L., Park, S., Podgorski, W. A., Bush, R. I., Scherrer, P. H., Gummin, M. A., Smith, P., Auken, G., Jerram, P., Pool, P., Soufli, R., Windt, D. L., Beardsley, S., Clapp, M., Lang, J. and Waltham, N. (2012), The Atmospheric Imaging Assembly (AIA) on the Solar Dynamics Observatory (SDO), *Solar Physics* **275**, 17–40.
- Luna, M., Karpen, J. T. and DeVore, C. R. (2012), Formation and evolution of a multi-threaded solar prominence, *The Astrophysical Journal* **746**, 000.
- Lynch, B. J., Antiochos, S. K., MacNeice, P. J., Zurbuchen, T. H. and Fisk, L. A. (2004), Observable Properties of the Breakout Model for Coronal Mass Ejections, *The Astrophysical Journal* **617**, 589–599.
- Mackay, D. H., Karpen, J. T., Ballester, J. L., Schmieder, B. and Aulanier, G. (2010), Physics of Solar Prominences: II—Magnetic Structure and Dynamics, *Space Science Reviews* **151**, 333–399.

- Miyoshi, T. and Kusano, K. (2005), A multi-state HLL approximate Riemann solver for ideal magnetohydrodynamics, *Journal of Computational Physics* **208**, 315–344.
- Moore, R. L., Sterling, A. C., Hudson, H. S. and Lemen, J. R. (2001), Onset of the Magnetic Explosion in Solar Flares and Coronal Mass Ejections, *The Astrophysical Journal* **552**(2), 833.
- Morgan, H. (2015), An Atlas of Coronal Electron Density at $5R_{\odot}$. I. Data Processing and Calibration, *The Astrophysical Journal Supplement Series* **219**, 23.
- Parenti, S. (2014), Solar Prominences: Observations, *Living Reviews in Solar Physics* **11**.
- Pesnell, W. D., Thompson, B. J. and Chamberlin, P. C. (2011), The Solar Dynamics Observatory (SDO), *Solar Physics* **275**(1-2), 3–15.
- Phillips, K. J. H. (1995), Guide to the Sun, <http://www.cambridge.org/gb/academic/subjects/astronomy/solar-and-space-plasma-physics/guide-sun>.
- Schwartz, P., Heinzel, P., Kotrc, P., Fárník, F., Kupryakov, Y. A., DeLuca, E. E. and Golub, L. (2015), Total mass of six quiescent prominences estimated from their multi-spectral observations, *Astronomy and Astrophysics* **574**, A62.
- Sharp, D. H. (1984), An overview of Rayleigh-Taylor instability, *Physica D: Nonlinear Phenomena* **12**(1–3), 3–18.
- Shibata, K., Masuda, S., Shimojo, M., Hara, H., Yokoyama, T., Tsuneta, S., Kosugi, T. and Ogawara, Y. (1995), Hot-Plasma Ejections Associated with Compact-Loop Solar Flares, *The Astrophysical Journal Letters* **451**, L83.
- Stenflo, J. O. (1982), The Hanle effect and the diagnostics of turbulent magnetic fields in the solar atmosphere, *Solar Physics* **80**, 209–226.

- Stone, J. M., Gardiner, T. A., Teuben, P., Hawley, J. F. and Simon, J. B. (2008), Athena: A New Code for Astrophysical MHD, *The Astrophysical Journal Supplement Series* **178**, 137–177.
- Stone, J. M. and Gardiner, T. (2007a), The Magnetic Rayleigh-Taylor Instability in Three Dimensions, *The Astrophysical Journal* **671**(2), 1726.
- Stone, J. M. and Gardiner, T. A. (2007b), Nonlinear Evolution of the Magneto-hydrodynamic Rayleigh-Taylor Instability, *Physics of Fluids* **19**(9), 094104.
- van Ballegooijen, A. A. and Martens, P. C. H. (1989), Formation and eruption of solar prominences, *The Astrophysical Journal* **343**, 971–984.
- van Driel-Gesztelyi, L., Baker, D., Török, T., Pariat, E., Green, L. M., Williams, D. R., Carlyle, J., Valori, G., Démoulin, P., Kliem, B., Long, D. M., Matthews, S. A. and Malherbe, J.-M. (2014), Coronal Magnetic Reconnection Driven by CME Expansion—The 2011 June 7 Event, *The Astrophysical Journal* **788**, 85.
- Williams, D. R., Baker, D. and van Driel-Gesztelyi, L. (2013), Mass Estimates of Rapidly Moving Prominence Material from High-cadence EUV Images, *The Astrophysical Journal* **764**(2), 165.
- Williams, D. R., Török, T., Démoulin, P., van Driel-Gesztelyi, L. and Kliem, B. (2005), Eruption of a Kink-unstable Filament in NOAA Active Region 10696, *The Astrophysical Journal Letters* **628**, L163–L166.
- Wuelser, J.-P., Lemen, J. R., Tarbell, T. D., Wolfson, C. J., Cannon, J. C., Carpenter, B. A., Duncan, D. W., Gradwohl, G. S., Meyer, S. B., Moore, A. S., Navarro, R. L., Pearson, J. D., Rossi, G. R., Springer, L. A., Howard, R. A., Moses, J. D., Newmark, J. S., Delaboudiniere, J.-P., Artzner, G. E., Auchere, F., Bougnet, M., Bouyries, P., Bridou, F., Clotaire, J.-Y., Colas, G., Delmotte, F., Jerome, A., Lamare, M., Mercier, R., Mullet, M., Ravet, M.-F., Song, X., Bothmer, V. and Deutsch, W. (2004), EUVI: the STEREO-SECCHI extreme ultraviolet imager, in S. Fineschi and M. A. Gummin (eds.), *Proc. SPIE 5171*, pp.111–122.

Youngs, D. L. (1989), Modelling turbulent mixing by Rayleigh-Taylor instability, *Physica D: Nonlinear Phenomena* **37**(1–3), 270–287.